

**ROLE OF PHASE TRANSFORMATION PROCESSES IN DETERMINING THE
DISCHARGE BEHAVIOR OF ELECTRODES IN LITHIUM ION BATTERY**

A Dissertation

Presented to

the Faculty of the Graduate School

Tennessee Technological University

By

Uday S. Kasavajjula

In Partial Fulfillment

of the Requirements of the Degree

DOCTOR OF PHILOSOPHY

Engineering

May 2009

UMI Number: 3355189

INFORMATION TO USERS

The quality of this reproduction is dependent upon the quality of the copy submitted. Broken or indistinct print, colored or poor quality illustrations and photographs, print bleed-through, substandard margins, and improper alignment can adversely affect reproduction.

In the unlikely event that the author did not send a complete manuscript and there are missing pages, these will be noted. Also, if unauthorized copyright material had to be removed, a note will indicate the deletion.



UMI Microform 3355189
Copyright 2009 by ProQuest LLC
All rights reserved. This microform edition is protected against
unauthorized copying under Title 17, United States Code.

ProQuest LLC
789 East Eisenhower Parkway
P.O. Box 1346
Ann Arbor, MI 48106-1346

CERTIFICATE OF APPROVAL OF DISSERTATION

**ROLE OF PHASE TRANSFORMATION PROCESSES IN DETERMINING THE
DISCHARGE BEHAVIOR OF ELECTRODES IN LITHIUM ION BATTERY**

by

Uday S. Kasavajjula

Graduate Advisory Committee:



Pedro E. Arce, Chairperson

02-06-09
date

S. Venkat Ramanan

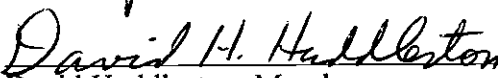
Venkat Subramanian, Member

3-6-09
date



Holly A. Stretz, Member

3-6-09
date



David Huddleston, Member

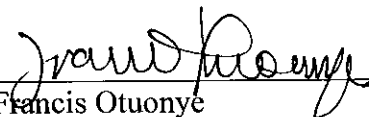
3-6-09
date



Ying Zhang, Member

3-6-09
date

Approved for the Faculty:



Francis Otuonye

Associate Vice President for Research
and Graduate Studies

5/6/09

Date

AN ABSTRACT OF A DISSERTATION

ROLE OF PHASE TRANSFORMATION PROCESSES IN DETERMINING THE DISCHARGE BEHAVIOR OF ELECTRODES IN LITHIUM ION BATTERY

Uday S. Kasavajjula

Doctor of Philosophy in Engineering

Although the performance of Li-ion batteries has improved dramatically in last ten years, Li-ion batteries cannot be directly used in hybrid-electric vehicles and electric vehicles, as they are limited by low pulse power, abuse tolerance, calendar and cycle life, and high cost. In this context, the newly-developed phase transformation cathode materials such as LiFePO_4 make the Li-ion batteries, a promising candidate for vehicular applications, as LiFePO_4 exhibits high power density, high electrochemical and thermal stability, and relative inexpensive and less toxic nature compared to conventional insertion electrodes. However, the commercial applications of LiFePO_4 in Li-ion batteries were limited due to its poor rate capability. In order to improve the rate capability of LiFePO_4 cathode materials or to develop new phase transformation electrode materials with high rate capability, it is essential to understand the electrochemical kinetics and rate-controlling mechanisms involved in the charge/discharge process. To date, the shrinking core model (SCM) is the only mathematical model available in the literature, that is applicable to phase transformation electrodes. Currently, LiFePO_4 is available from different manufacturers and all of them exhibit different rate capabilities. The difference in rate capabilities of these samples cannot be explained by the shrinking core model. Also a large discrepancy can be observed between the experimental discharge curves and discharge curves obtained from shrinking core model.

In this doctoral dissertation, the reasons for the discrepancy between experimental results and the results obtained from shrinking core model are identified by experimental techniques and mathematical modeling. From these results, it is found that the diffusion is not the only controlling mechanism for the discharge process of LiFePO_4 and the discrepancy between the experimental and SCM results is due to the assumptions used in the SCM. Based on these results and also by assuming that the discharge process is controlled by both diffusion and rate of phase transformation, the shrinking core model is modified. The modified SCM is validated by predicting the discharge behavior of three commercially-available LiFePO_4 samples. Using the modified shrinking core model as a tool, the effects of chemical diffusion, rate of phase transformation, solid solution range, volume change, and particle size on discharge rate capability of LiFePO_4 are determined. The modified SCM developed in this contribution is applicable to any phase transformation electrode such as $\text{Li}_4\text{Ti}_5\text{O}_{12}$ in Li-ion battery and metal hydride electrode in Nickel metal hydride battery, thus making it a useful tool for practitioners in the field.

DEDICATION

Dedicated to my parents Mr. K. A. R. Sastry, Mrs. Shanta, and my wife Satyavani Bari

ACKNOWLEDGEMENTS

I am thankful to many individuals for their encouragement and support throughout this work. Foremost, I would like to express my deep and sincere gratitude to my co-advisor, Dr. Chunsheng Wang for his continuous support during the Ph.D. program. It is a great honor for me to work with him and I am thankful to almighty for giving me a such nice person as an advisor. I am grateful to Dr. Chunsheng Wang for giving me an opportunity to choose this work as topic of my dissertation. The invaluable suggestions offered by him and the diligence with which he assisted in my research helped me a long way in realizing this dissertation. The discussions I had with him have improved my understanding of electrochemistry, material science, and also my analytical skills.

Next, I would like to acknowledge my co-advisor Dr. Pedro Arce, for his suggestions on mathematical modeling and for his great moral support in the absence of Dr. Chunsheng Wang. Without his encouragement and support, I could not have finished the dissertation. I also would like to acknowledge my other graduate committee members, Dr. Venkat Subramanian, Dr. Ying Zhang, Dr. David Huddleston, and Dr. Holly Stretz, for their valuable comments on my proposal and dissertation, which have greatly improved the quality of the dissertation. Also I would like to express my special thanks to my manager at Johnson Controls, Dr. James Symanski, for the valuable comments on the dissertation.

I would like to thank U.S. Army Communications Electronics Command, Department of Chemical Engineering, and Center for Manufacturing Research for providing the financial support during my graduate study. I wish to express my heartfelt appreciation for the staff of Department of Chemical Engineering (Ms. Christy Huddleston and Ms. Becky Asher) and Center for Manufacturing Research (Ms. Phyllis Stallion and Ms. Sue Richardson) for helping me with my degree.

I am wholeheartedly thankful to my parents Mr. K. A. R. Sastry and Mrs. Shanta, and my family members for the dose of warmth and affection from time to time. Also many thanks to my wife Satyavani Bari, for her support and help during tough times of my graduate student life. Last but of course not least, this work would not have been achieved without the support and encouragement of my friends.

TABLE OF CONTENTS

	Page
LIST OF FIGURES.....	VII
LIST OF TABLES.....	XI
Chapter	
1 INTRODUCTION.....	1
1.1 Hybrid Electric Vehicles (HEVs) and Electric Vehicles (EVs).....	2
1.2 Types of Rechargeable Batteries and Their Comparison.....	3
1.3 Li-ion Battery: Working Principle and Performance.....	4
1.4 Issues for Li-ion Batteries in HEVs and EVs.....	6
1.5 Alternative to LiCoO ₂ Cathodes: LiFePO ₄	7
1.6 Outline of Dissertation.....	9
2 LITERATURE REVIEW.....	11
2.1 LiFePO ₄ : Improvement in Rate Capability.....	11
2.2 Mathematical Modeling: Brief Review of Efforts.....	19
2.3 Shrinking Core Model (SCM) for Phase Transformation Electrodes.....	20
2.4 Validation of SCM.....	23
3 Experimental Methodology.....	26
3.1 Equipment Description.....	26
3.1.1 Glove Box.....	26
3.1.2 Hand-Operated Closing Tool.....	27
3.1.3 Battery Testing Machine.....	29
3.1.4 AC Impedance Spectroscopy.....	30
3.2 Electrode Preparation.....	31
3.3 Procedure for Conducting Experiments.....	32
3.3.1 Galvanostatic Charge/Discharge Test.....	33
3.3.2 Galvanostatic Intermittent Titration Technique (GITT).....	33
3.3.3 Potential Step Chronoamperometry (PSCA).....	34
3.4 Experimental Results of Samples A and B LiFePO ₄ Cathodes.....	34
3.4.1 Discharge Rate Capability Data for Samples A and B.....	34
3.4.2 Equilibrium Potential Composition Isotherms for Samples A and B LiFePO ₄	38
3.4.3 Parameter Values from Experiments.....	40
4 ASSESSMENT of APPLICABILITY OF SCM to LiFePO ₄ CATHODES.....	41
4.1 Assessment by Mathematical Modeling.....	41
4.1.1 Solving the SCM.....	42
4.1.2 Determining Equilibrium Potential.....	42
4.1.3 Determining Overpotential and Voltage.....	45
4.1.4 Predicting the Discharge Curves of Samples A and B.....	45
4.1.5 Effect of Particle Shape on Discharge Curves.....	48
4.2 Assessment by Potential-step Chronoamperometry (PSCA) Measurement.....	49

Chapter	Page
4.3	Limitations of Shrinking Core Model 56
5	DEVELOPMENT OF MATHEMATICAL MODEL 57
5.1	Modified SCM-1: Model Involving Only Transport in β Phase 57
5.1.1	Description of Discharge Process of LiFePO_4 57
5.1.2	Governing Equations and Boundary Conditions 61
5.1.3	Theory of Mixed Mode Phase Transformations 63
5.1.4	Solution Methodology 70
5.1.5	Parameter Sensitivity 72
5.1.6	Pseudosteady-State (PSS) Solution 78
5.1.7	Parameter Estimation for D_β , M , n , and A 80
5.1.8	Model Validation 84
5.2	Modified SCM-2: Model Involving Transport in α and β Phases 89
5.2.1	Li^+ ion Concentration Distribution in the LiFePO_4 Particle during Discharge Process 90
5.2.2	Governing Equations and Boundary Conditions 91
5.2.3	Solution Methodology 95
5.2.4	Equations for Equilibrium Potential and Overpotential 96
5.2.5	Parameter Estimation 99
5.2.6	Model Validation 100
6	RATE CAPABILITY ANALYSIS 106
6.1	Effect of Lithium Chemical Diffusion in β phase and Interface Mobility on Rate Capability 106
6.2	Effect of Solid Solution Range on Rate Capability 115
6.2.1	Effect of β phase Solid Solution Range and β Phase Chemical Diffusion Coefficient on Rate Capability 116
6.2.2	Effect of Extending the α Solid Solution Range on Rate Capability 123
6.2.3	Effect of Extending the α and β Solid Solutions Simultaneously on Rate Capability 126
6.3	Effect of Accommodation Energy on Rate Capability 132
6.4	Effect of Particle Size/Diffusion Length on Rate Capability 137
7	CONCLUSIONS 141
8	FUTURE WORK 147
8.1	Description of Porous Electrode 148
8.2	Porous Electrode Theory 150
8.3	Summary of System of Equations 155
8.3.1	Equations for Porous Electrode 155
8.3.2	Determination of $C_{\beta s}$ from Particle Scale Model (refer to section 5.1.2) 157
8.4	Possible Strategy for Solving the System of Equations 158
	List of Symbols 160
	References 163
	VITA 169

LIST OF FIGURES

	Page
Figure 1.1: Sketch illustrating the working principle of commercial standard rechargeable Li-ion battery.....	7
Figure 2.1: Discharge curves of a LiFePO ₄ sample at different current densities: Experimental (symbols) and Shrinking core model Predictions (lines) (figure taken from ref. 53).....	24
Figure 3.1: Glove Box.....	27
Figure 3.2: (a). Parts of Coin cell (From left: Rubber gasket, stainless steel plate, stainless steel spring, cap, coin case) (b) Hand-Operated Closing Tool.....	28
Figure 3.3: 16-Channel BT2000 Battery Testing System.....	29
Figure 3.4: (a) Galvanostat/Potentiostat (b) Impedance/Gain Phase Analyzer.....	30
Figure 3.5: Schematic of 3 electrode PTFE cell.....	32
Figure 3.6: Discharge curves of Sample A LiFePO ₄ obtained from Galvanostatic charge/discharge test (from left: 5C, 2C, 1C, 0.5C, 0.2C, and 0.1C).....	36
Figure 3.7: Discharge curves of Sample B LiFePO ₄ obtained from Galvanostatic charge/discharge test (from left: 20C, 10C, 5C, 2C, 1C, 0.5C, 0.2C, and 0.1C).....	37
Figure 3.8: Equilibrium Potential Curve of Sample A LiFePO ₄ during discharge obtained from GITT experiment.....	39
Figure 3.9: Equilibrium Potential Curve of Sample B LiFePO ₄ during discharge obtained from GITT experiment.....	39
Figure 4.1: Equilibrium Potential vs. Li content x for Li _x FePO ₄ /A obtained from Experiment and Eq. 4.1.....	44
Figure 4.2: Equilibrium Potential vs. Li content x for Li _x FePO ₄ /B obtained from Experiment and Eq. 4.2.....	44
Figure 4.3: Discharge curves of sample A LiFePO ₄ sample at different current densities: Experimental (symbols) and SCM Predictions (lines).....	47
Figure 4.4: Discharge curves of sample B LiFePO ₄ sample at different current densities: Experimental (symbols) and SCM Predictions (lines).....	47
Figure 4.5: Discharge curves of LiFePO ₄ predicted from SCM with rectangular geometry and SCM with spherical geometry.....	49
Figure 4.6: The absolute value of anodic and cathodic currents of LiFe _{0.9} Mg _{0.1} PO ₄ (a) in a linear scale and (b) in a logarithm scale obtained by potential-step experiment. The negative charge current induced by potential jumping from 3.1 V to 3.48 V was converted to positive value to compare with discharge jumping current.	52
Figure 4.7: Illustration of the shrinking-core model with the juxtaposition of the two phases during the Li extraction (charge) from LiFe _{0.9} Mg _{0.1} PO ₄ and the movement of the phase boundary.....	53
Figure 4.8: Time dependence of reacted fraction α(t) of fully discharged LiFe _{0.9} Mg _{0.1} PO ₄ electrode for the charge process.....	54
Figure 4.9: Relationship between the position of phase boundary ζ and time for fully discharged LiFe _{0.9} Mg _{0.1} PO ₄ electrode during charge process.....	55

Figure 4.10: $-\ln(1-\alpha)$ plotted against time for charge process of $\text{LiFe}_{0.9}\text{Mg}_{0.1}\text{PO}_4$ electrode	55
Figure 5.1: Schematic showing (a) phase transformation and (b) Li^+ ion concentration distribution during the discharge of a LiFePO_4 particle (Li insertion into FePO_4)	60
Figure 5.2: Variation of accommodation energy during hydride precipitation through the surface to center path for different aspect ratios of the precipitate (figure taken from ref. 72)	68
Figure 5.3: (a) Interface position of LiFePO_4 vs. dimensionless time (b) Dimensionless Surface concentration of LiFePO_4 vs. dimensionless time (c) Over-potential of LiFePO_4 vs. dimensionless time (d) Equilibrium potential of LiFePO_4 vs. dimensionless time (e) Voltage of LiFePO_4 vs. dimensionless time	73
Figure 5.4: Effect of the parameter D_β on discharge curve at 5C obtained from modified SCM-1 with $M = 1 \times 10^{-10}$ m.mol/(J.s), $n = 2.2$ (From left: $D_\beta = 5 \times 10^{-17}$, 1×10^{-16} , 5×10^{-16} , 1×10^{-15} , 5×10^{-15} , 1×10^{-14} , 5×10^{-14} , and 1×10^{-13} m ² /s)	76
Figure 5.5: Effect of the parameter M on discharge curve at 5C obtained from modified SCM-1 with $D_\beta = 1 \times 10^{-14}$ m ² /s, $n = 2.2$ (From left: $M = 2 \times 10^{-12}$, 5×10^{-12} , 1×10^{-11} , 2×10^{-11} , 5×10^{-11} , 1×10^{-10} , 5×10^{-10} , 1×10^{-19} , and 1×10^{-8} m.mol/(J.s))	76
Figure 5.6: Effect of parameter n on accommodation energy variation during phase transformation ($n = 15, 12, 10, 8, 6, 4, 2.2,$ and 1)	77
Figure 5.7: Effect of the parameter n on discharge curve at 5C obtained from modified SCM-1 with $D_\beta = 1 \times 10^{-14}$ m ² /s, $M = 1 \times 10^{-10}$ m.mol/(J.s) (From left: $n = 15, 12, 10, 8, 6, 4, 2.2,$ and 1)	77
Figure 5.8: Dimensionless interface position as a function of dimensionless time at different current densities (From left: 1C, 0.5C, 0.2C, and 0.1C) obtained from PSS (Lines) and numerical method of lines (Symbols) (Values of the parameters used: $D_\beta = 3.8 \times 10^{-15}$ m ² /s, $M = 1 \times 10^{-8}$ m.mol/(J.s), $Z = 0.0004$)	81
Figure 5.9: Dimensionless surface concentration as a function of dimensionless time at different current densities (From left: 1C, 0.5C, 0.2C, and 0.1C) obtained from PSS (Lines) and numerical method of lines (Symbols) (Values of the parameters used: $D_\beta = 3.8 \times 10^{-15}$ m ² /s, $M = 1 \times 10^{-8}$ m.mol/(J.s), $Z = 0.0004$)	81
Figure 5.10: Dimensionless interface position as a function of dimensionless time at different current densities (From left: 1C, 0.5C, 0.2C, and 0.1C) obtained from PSS (Lines) and numerical method of lines (Symbols) (Values of the parameters used: $D_\beta = 3.8 \times 10^{-15}$ m ² /s, $M = 1 \times 10^{-12}$ m.mol/(J.s), $Z = 4$)	82
Figure 5.11: Dimensionless surface concentration as a function of dimensionless time at different current densities (From left: 1C, 0.5C, 0.2C, and 0.1C) obtained from PSS (Lines) and numerical method of lines (Symbols) (Values of the parameters used: $D_\beta = 3.8 \times 10^{-15}$ m ² /s, $M = 1 \times 10^{-12}$ m.mol/(J.s), $Z = 4$)	82
Figure 5.12: Discharge curves of LiFePO_4/A obtained from experiment and modified SCM-1 at 5C, 2C, 1C, 0.5C, 0.2C, and 0.1C (symbols: Experiment, lines: Model)	86

Figure 5.13: Discharge curves of LiFePO ₄ /B obtained from experiment and modified SCM-1 at 20C, 10C, 5C, 2C, 1C, 0.5C, 0.2C, and 0.1C (symbols: Experiment, lines: Model).....	87
Figure 5.14: Discharge curves at 5C, 2C, 1C, 0.5C obtained from modified SCM-1 (with $M = 1 \times 10^{-8}$ m.mol/(J.s), $n = 2.2$) and SCM with rectangular geometry (particle scale model only). Values of the common parameters for both the models: $D_{\beta} = 8 \times 10^{-16}$ m ² /s, $i_0 = 0.1$ A/g, $C_t = 0.02044$ mol/cm ³ , $\rho = 3.6$ gm/cm ³ , $\theta_{\beta\alpha} = 0.7718$	88
Figure 5.15: Schematic showing (a) phase transformation and (b) Li ⁺ ion concentration distribution during the discharge of a LiFePO ₄ particle (Li insertion into FePO ₄).....	92
Figure 5.16: Equilibrium Potential vs. Li content x in Li _x FePO ₄ /A obtained from Experiment (Symbols) and Eq. 5.58 (Line)	98
Figure 5.17: Equilibrium Potential vs. Li content x in Li _x FePO ₄ /B obtained from Experiment (Symbols) and Eq. 5.59 (Line)	98
Figure 5.18: Discharge curves of LiFePO ₄ /A obtained from experiment and modified SCM-2 at 5C, 2C, 1C, 0.5C, 0.2C, and 0.1C (symbols: Experiment, lines: Model).....	101
Figure 5.19: Discharge curves of LiFePO ₄ /B obtained from experiment and modified SCM-2 at 20C, 10C, 5C, 2C, 1C, 0.5C, 0.2C, and 0.1C (symbols: Experiment, lines: Model).....	102
Figure 5.20: Comparison of specific discharge capacity versus galvanostatic discharge rate for Sample NC (top) Sample AC (bottom)	105
Figure 5.21: Rate capability behavior predicted from the modified SCM-2 for Sample NC and Sample AC reported in ref [25]......	105
Figure 6.1: Simulated discharge capacity of LiFePO ₄ at different currents as a function of Interface Mobility and β phase chemical chemical diffusion coefficient (a: 0.1C, b:5.0C).....	111
Figure 6.2: Contour plot for ratio of discharge capacity (simulated) at 5C to discharge capacity (simulated) at 0.1C for LiFePO ₄ as a function of interface mobility and β phase chemical diffusion coefficient. The capacity ratio at 5C to 0.1C for Sample A (blue circle) and Sample B (white circle) are also shown for comparison	113
Figure 6.3: Contour plot for ratio of discharge capacity (simulated) at 10C to discharge capacity (simulated) at 0.1C for LiFePO ₄ as a function of interface mobility and β phase chemical diffusion coefficient. The capacity ratio at 10C to 0.1 C for Sample B (blue circle) is also shown.....	114
Figure 6.4: Equilibrium Potential Curves (obtained from Eq. 4.1 with different coefficients) for LiFePO ₄ with different β phase solid solution range as a function of Li content in FePO ₄ during discharge process.....	118
Figure 6.5: Simulated discharge Capacity of LiFePO ₄ at different Currents as a function of β phase Solid Solution Range and β phase chemical diffusion coefficient (a: 0.1C, b:5.0C).....	119

Figure 6.6: Contour plot for ratio of discharge capacity (simulated) at 5C to discharge capacity (simulated) at 0.1C for LiFePO ₄ as a function of β phase chemical diffusion coefficient and β phase solid solution range.....	121
Figure 6.7: Contour plot for ratio of discharge capacity (simulated) at 10C to discharge capacity (simulated) at 0.1C for LiFePO ₄ as a function of β phase chemical diffusion coefficient and β phase solid solution range.....	122
Figure 6.8: Equilibrium Potential Curves (obtained from Eq. [25] with different coefficients) for LiFePO ₄ with different α solid solution range (different $\theta_{\alpha\beta}$ and $\theta_{\beta\alpha}=0.77$) as a function of Li content in FePO ₄ during discharge process ($\theta_{\alpha\beta}$ = a:0.015, b:0.1, c:0.15, d:0.2, e:0.25, f:0.3, g:0.35, h:0.4)	124
Figure 6.9: Discharge curves of LiFePO ₄ with different α solid solution limits ($\theta_{\alpha\beta}$ = a:0.015, b:0.1, c:0.15, d:0.2, e:0.25, f:0.3, g:0.35, h:0.4) at 5C and 10C	125
Figure 6.10: Discharge curves of LiFePO ₄ with different α solid solution limits ($\theta_{\alpha\beta}$ = a:0.015, b:0.1, c:0.15, d:0.2, e:0.25, f:0.3, g:0.35, h:0.4) at 20C	126
Figure 6.11: Equilibrium Potential Curves (obtained from Eq. 5.58 with different coefficients) for LiFePO ₄ with different α and β solid solution ranges as a function of Li content in FePO ₄ during discharge process ($\theta_{\alpha\beta}$ & $\theta_{\beta\alpha}$: a=0.015&0.77, b=0.1&0.7, c=0.15&0.65, d=0.2&0.6, e=0.25&0.55, f=0.3&0.5, g=0.35&0.45)	128
Figure 6.12: Discharge curves of LiFePO ₄ with different α and β solid solution limits ($\theta_{\alpha\beta}$ & $\theta_{\beta\alpha}$: a=0.015&0.77, b=0.1&0.7, c=0.15&0.65, d=0.2&0.6, e=0.25&0.55, f=0.3&0.5, g=0.35&0.45) at 0.1C and 10C	129
Figure 6.13: Discharge curves of LiFePO ₄ with different α and β solid solution limits ($\theta_{\alpha\beta}$ & $\theta_{\beta\alpha}$: a=0.015&0.77, b=0.1&0.7, c=0.15&0.65, d=0.2&0.6, e=0.25&0.55, f=0.3&0.5, g=0.35&0.45) at 20C.....	130
Figure 6.14: Effect of increasing α and β solid solutions on rate capability of LiFePO ₄ with a chemical diffusion coefficient (D_{β}) of a: 8×10^{-14} m ² /s, b: 8×10^{-16} m ² /s.....	131
Figure 6.15: Effect of accommodation energy factor on discharge curves of LiFePO ₄ at 10C current	134
Figure 6.16: Effect of accommodation energy factor and β phase chemical diffusion coefficient on discharge capacity of LiFePO ₄ at 10C current.....	135
Figure 6.17: Effect of accommodation energy factor and Interface Mobility on discharge capacity of LiFePO ₄ at 10C current	136
Figure 6.18: Effect of particle radius on discharge capacity of LiFePO ₄ at different currents ($D_{\beta} = 8 \times 10^{-15}$ m ² /s, $M = 6.3 \times 10^{-12}$ m mol/(Js)).....	138
Figure 6.19: Effect of diffusion length on discharge capacity of LiFePO ₄ at 10C with different chemical diffusion capabilities ($M = 6.3 \times 10^{-12}$ m mol/(Js))	139
Figure 6.20: Effect of diffusion length on discharge capacity of LiFePO ₄ at 10C with different interface mobilities ($D_{\beta} = 8 \times 10^{-16}$ m ² /s)	140
Figure 8.1: Schematic of LiFePO ₄ half cell, consisting of current collector, LiFePO ₄ electrode, separator and Lithium metal	149

LIST OF TABLES

	Page
Table 1.1: Comparison of performance of various types of rechargeable batteries.....	5
Table 5.1: List of parameter values used for modeling LiFePO ₄ cathode materials and for further analysis	84
Table 5.2: List of parameter values used for modeling LiFePO ₄ cathode materials.....	101
Table 5.3: The values of the parameters used in the model for Sample AC and Sample NC.	104

CHAPTER 1

INTRODUCTION

Increasing demand for sustained energy supply and increasing global warming are among the major concerns/problems for the world in 21st century. In the present world, energy is required for performing each and every function necessary for the society. In 2005, the total energy consumed by human population in the world was equivalent to 15 trillion Watts, and 40% of it originated from petroleum [1]. Hence, petroleum is a primary energy source for us and the continuous supply of it is essential for the existence. In 2007, the total consumption of petroleum in the world was 84 million barrels/day and the petroleum consumption in United States was one fourth (20 million barrels/day) of the world's consumption [2]. Of 20 billion barrels consumed each day, 58 percent was imported and 70 percent was used for transportation, which shows the heavy reliance of transportation sector in United States on foreign petroleum reserves [3]. At present, the known reserves of petroleum are estimated as 190 km³ (1.2 trillion barrels) and at current consumption levels (84 million barrels/day) [4], these known reservoirs would be depleted by the year 2039, potentially leading to global energy crisis. Due to the heavy reliance on petroleum, the energy crisis will have a greater impact on the transportation sector in the United States. In addition to depleting petroleum reserves, the transportation sector suffers from global warming issues. The emissions leading to global warming in United States are 25% of the worldwide emissions, and the transportation sector contributes to 31% of the total CO₂ emissions in the United States [5]. In order to reduce the air pollution and petroleum consumption in the United States, and to reduce the U.S.

reliance on foreign sources of petroleum, the leadership of General Motors Corporation, Ford Motor Company, Daimler Chrysler Corporation, and EPRT has formed U.S. Advanced Battery Consortium (USABCE) in 1991. Similarly, the U.S. Department of Energy and the leadership of General Motors Corporation, Ford Motor Company, and Daimler Chrysler Corporation has announced the creation of FreedomCAR and Vehicle Technologies Program on January 9th 2003. The major goal of USABCE and the FreedomCar and Vehicle Technologies program is to develop hybrid electric vehicles and electric vehicles, thereby reducing the nation's use of imported oil and the air pollution.

1.1 Hybrid Electric Vehicles (HEVs) and Electric Vehicles (EVs)

An Electric Vehicle (EV) does not have an internal combustion and runs only on rechargeable batteries. The rechargeable batteries provide electricity to the electric motor, and the electric motor turns the transmission, and the transmission turns the wheels. The operating mechanism of hybrid electric vehicle (HEV) is different from electric vehicle (EV), as it combines the concept of both conventional vehicle and the electrical vehicle. In general, a HEV has an internal combustion engine, rechargeable battery, and an electrical motor. The internal combustion engine used in HEV is much smaller and has been tuned to be more efficient than that of conventional vehicles. In HEV, both the internal combustion engine and rechargeable batteries provide electricity to the electric motor to drive the car, hence resulting in more gas mileage. The electric motor in HEVs can also act as a generator. By acting as a generator, it converts the kinetic energy released during breaking into electrical energy and uses this energy to recharge the

battery. Although both HEV and EV employ rechargeable batteries, they differ in the gas mileage and the exhaust emissions. Generally, EV is zero emission vehicle and can only travel for 50 to 100 miles between each charge. Whereas the HEV is a vehicle with low emissions and more gas mileage compared to conventional vehicles. Though the operating principles of HEV and EV are different, their performance strongly depends on the type of the rechargeable battery used.

1.2 Types of Rechargeable Batteries and Their Comparison

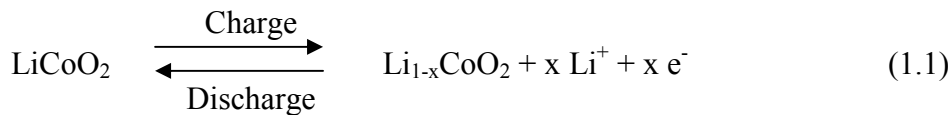
A battery is an electrochemical device which converts chemical energy to electrical energy by means of reduction and oxidation (redox) reactions. Based on the reversibility of the redox reactions, batteries are generally classified as primary and secondary (rechargeable) batteries. After discharge, the secondary batteries can be charged to the original condition by passing current through them in the opposite direction to that of the discharge current. The primary batteries cannot be recharged [6]. Currently, different types of rechargeable/secondary batteries are available commercially and they differ in the electrochemical reactions taking place inside the battery. Table summarizes the types of available commercial rechargeable batteries and their performance. From Table, it is evident that Lithium ion (Li-ion) batteries exhibit high operating voltage, energy density and power density, and low self-discharge compared to other rechargeable batteries. Also, they require low maintenance compared to other rechargeable batteries. Due to these advantages, lithium ion batteries are commonly used in portable applications such as cell phones, laptops and mp3s, and are also considered as

promising candidates for HEVs and EVs. Current HEVs such as the Toyota Prius employ nickel metal hydride (NiMH) batteries. Since Li-ion batteries have 2-3 times higher energy density and power density compared to NiMH batteries (Table), replacing NiMH batteries with Li-ion batteries would result in saving 60% mass and volume of batteries used in the vehicle.

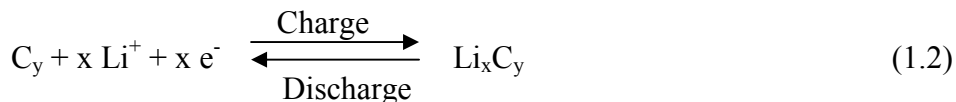
1.3 Li-ion Battery: Working Principle and Performance

Figure shows the components and working principle of a typical commercial Li-ion battery. It consists of graphite anode and LiCoO₂ cathode separated by a polymer separator filled with a Li-ion conducting organic electrolyte. It also has Al and Cu foils as current collectors. When a Li-ion cell is charged, Li⁺ ions move out from the cathode, transfer through the electrolyte, and insert into layered graphite forming Li_xC₆. On discharge process, the mechanism occurs in reverse direction leading to the formation of graphite and LiCoO₂. The electrochemical reactions occurring at positive electrode and negative electrode can be expressed as follows:

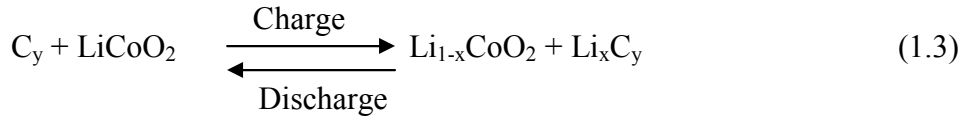
At Positive Electrode:



At Negative Electrode:



Overall Reaction:



Since Li^+ ions are transferred between graphite anode and $LiCoO_2$ cathode during the charge-discharge cycle, Li-ion batteries are sometimes referred to as ‘rocking-chair’ batteries. Since the charge/discharge processes involve only electrochemical charge transfer coupled with insertion of mobile Li^+ ions into the structure of the solid host (graphite or $LiCoO_2$) with out any chemical reaction, the graphite anode and the $LiCoO_2$ cathode are called insertion electrodes [7].

Table 1.1: Comparison of performance of various types of rechargeable batteries

Type Of Rechargeable Battery	Voltage (V)	Energy		Specific Power (W/kg)	Energy per consumer price (Wh/\$)	Self Discharge Rate (%/ month)	Cycles (#)
		Specific Energy (Wh/kg)	Energy Density (Wh/L)				
Lead-acid	2.1	30-40	60-75	180	5 – 8	3 – 4	500-800
Alkaline	1.5	85	250	50	7.7	<0.3	100-1000
Ni-cadmium	1.2	40-60	50-150	150	5 – 7	20	1500
Ni-metal Hydride	1.2	30-80	140-300	250-1000	1.37	20	1000
Ni-zinc	1.7	60	170	900	2 - 3.3		100-500
Lithium ion	3.6	160	270	1800	2.8 – 5	5 – 10	1200

1.4 Issues for Li-ion Batteries in HEVs and EVs

Although Li-ion batteries have certain advantages over other secondary batteries, they cannot be used directly in HEV applications, as they are limited by low pulse power, low abuse tolerance, high cost, and poor cycle life. Lithium ion batteries exhibit low capacity at high currents i.e. low rate capability. Due to the low rate capability, Li-ion batteries have low pulse power. Pulse power is the maximum power that can be released from the battery in a short span of time (2-60 seconds) and it is required to accelerate the car. Abuse tolerance of batteries is the ability to tolerate the short circuits, overcharge, over-discharge, mechanical shock, vibration, crush, and fire exposure. Li-ion batteries are vulnerable to the above-mentioned conditions and when overcharged or short-circuited, the temperature of the battery increases drastically.

When the temperature reaches 150°C , oxygen is released from LiCoO_2 i.e. resulting in an exothermic reaction. This leads to explosion of the battery, which is referred to as thermal runaway. Another major concern for Li-ion batteries is their high cost. As shown in Table, the energy offered by Li-ion batteries per consumer price is high compared to other batteries. As a result when installed in HEV or EV, Li-ion batteries increase the cost of vehicle considerably. Another limiting issue for Li-ion batteries in HEV applications is their poor cycle life. Similar to Ni-mH batteries, Li-ion batteries in current electric vehicles such as Tesla Roadster need to be replaced after 100,000 miles or 5 years [8]. In addition to the above-mentioned issues, LiCoO_2 used in Li-ion battery is not safe to the environment as it contains toxic elements such as Cobalt.

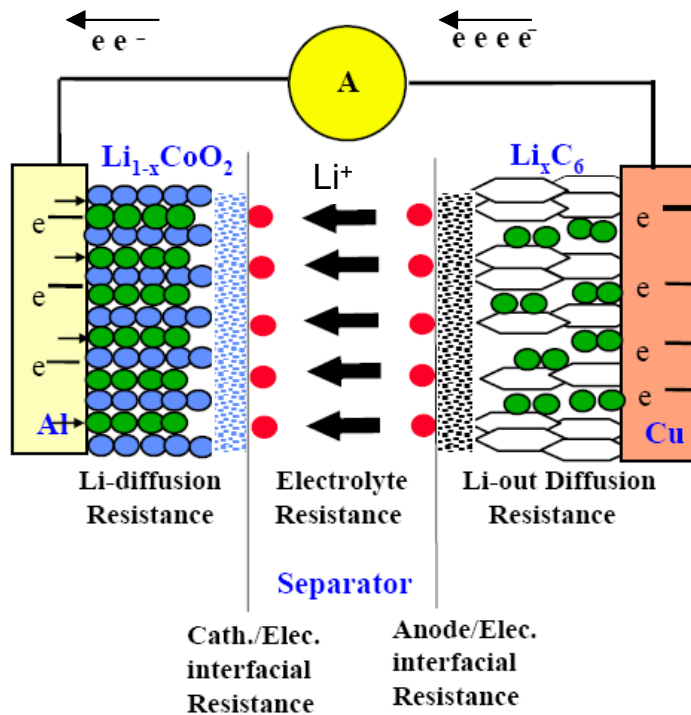


Figure 1.1: Sketch illustrating the working principle of commercial standard rechargeable Li-ion battery

1.5 Alternative to LiCoO_2 Cathodes: LiFePO_4

In order to overcome these issues and to use Li-ion batteries in HEVs and EVs, the carbonaceous anode and lithium cobalt-oxide cathodes have to be replaced by environmentally-safe electrode materials with high rate performance and high electrochemical and thermal stability. As alternatives for graphite anode, meso carbon micro beads (MCMB), hard carbon, carbon composites, inter-metallic compounds (Si alloys, Sn alloys, etc.) have been investigated. As alternatives for LiCoO_2 cathode, LiNiO_2 , LiMnO_2 , LiMn_2O_4 , LiMnNiO_2 , LiCoMnNiO_2 , LiFePO_4 , etc., have been investigated. Due to the various advantages it offers among the various cathode materials

tested, LiFePO_4 is found to be an excellent alternative for LiCoO_2 . LiFePO_4 has a theoretical capacity of 170 mAh/g, which is higher than that of LiCoO_2 (140 mAh/g). Also LiFePO_4 is electrochemically more stable compared to LiCoO_2 . The Fe-P-O bond in LiFePO_4 is much stronger than the Co-O bond in LiCoO_2 . Due to the stronger bonds, O_2 is not released from LiFePO_4 when abused (overheated or over-charged), unless the temperature of the cell rises to 800°C . As a result, LiFePO_4 is stable up to 800°C and does not suffer from thermal runaway. In addition to these advantages LiFePO_4 is relatively inexpensive and environment friendly compared to LiCoO_2 [9].

In spite of these advantages, LiFePO_4 has had limited commercial applications due to its poor rate capability. LiFePO_4 exhibits low discharge capacity at higher discharge currents, resulting in low discharge rate capability. Although extensive experimental work has been done to increase its rate capability, much less is known about the controlling mechanism for the discharge process. In order to further improve the rate capability of LiFePO_4 cathode and to develop new cathode materials, it is essential to understand the electrochemical kinetics and rate-controlling mechanisms involved in the charge/discharge process. This can be aided by developing mathematical models, which can accurately predict the discharge/charge behavior of LiFePO_4 . Prior to developing a mathematical model, it is very important to understand the charge/discharge mechanism of LiFePO_4 .

In addition to the electrochemical, thermal, and structural properties, LiFePO_4 also differs from LiCoO_2 in the charge/discharge mechanism. As mentioned earlier, in LiCoO_2 cathode, Li^+ ions diffuse into/out of $\text{CoO}_2/\text{LiCoO}_2$ layers during the discharge/charge process. The end members formed (CoO_2 , LiCoO_2) during the

charge/discharge process are solid solutions. Hence, they possess same crystal structure, though there is an orderly change in the lattice parameters. Thus, diffusion is the only key mechanism taking place in LiCoO_2 cathode during charge or discharge process. Different from LiCoO_2 , LiFePO_4 undergoes phase transformation during the charge/discharge process, resulting in the formation of two different (α and β) phases. Hence, charge/discharge process in LiFePO_4 involves diffusion in α phase, diffusion in β phase, and a phase transformation between α and β phases. Due to the difference in charge/discharge mechanism, the numerous mathematical models published in the literature for LiCoO_2 cannot be used to describe the charge/discharge process of LiFePO_4 . Similar to LiFePO_4 , $\text{Li}_4\text{Ti}_5\text{O}_{12}$ electrode also undergoes phase transformation during the charge/discharge process. Compared to all the electrode materials used in Li-ion batteries (LiCoO_2 , LiNiO_2 , LiMnO_2 , LiMn_2O_4 , LiMnNiO_2 , LiCoMnNiO_2 , LiFePO_4), $\text{Li}_4\text{Ti}_5\text{O}_{12}$ was found to have superior discharge rate capability. However, the exact reason for its superior rate capability is not known. Therefore, it is essential to develop a general mathematical model that can accurately predict the discharge behavior of LiFePO_4 and may also explain the reason for the superior rate capability of $\text{Li}_4\text{Ti}_5\text{O}_{12}$.

1.6 Outline of Dissertation

The objective of this work is to develop a general mathematical model for phase transformation electrodes such as LiFePO_4 and $\text{Li}_4\text{Ti}_5\text{O}_{12}$ in Li-ion battery. In Chapter 2, a brief literature review on LiFePO_4 and $\text{Li}_4\text{Ti}_5\text{O}_{12}$ electrode materials and the improvement of rate capability of LiFePO_4 in Li-ion batteries is presented. Mathematical

modeling efforts on phase transformation electrodes are also summarized in Chapter 2. A brief description of equipment used in this work, a detailed description of method of preparation of materials for cathode, and procedures for performing various electrochemical tests are given in Chapter 3. The applicability of SCM to LiFePO_4 cathode materials is discussed in Chapter 4. The theory relating to model development, system of equations involved in the model, and model validation are described in Chapter 5. In Chapter 6, effects of various properties on rate capability of phase transformation electrodes determined from the mathematical model are discussed. Finally, the conclusions and future recommendations for this work are presented in Chapter 7. The appropriate supplemental information is provided in the appendix.

CHAPTER 2

LITERATURE REVIEW

2.1 LiFePO₄: Improvement in Rate Capability

The use of LiFePO₄ material as a cathode in Li-ion batteries was first reported by Goodenough et al. [9] in 1997. In their work, LiFePO₄ was prepared by a direct solid-state reaction of stoichiometric amounts of Fe(II)-acetate, ammonium phosphate, and lithium carbonate. The charge and discharge experiments on LiFePO₄ had revealed that the most of the lithium could be extracted or inserted at a closed-circuit voltage of 3.5 V vs. lithium. The voltage during the charge/discharge was found to be independent over a large range of composition. From the voltage plateau and by Gibbs phase rule, it was concluded that the insertion/extraction reactions proceeded by the motion of a two-phase interface. From the XRD experiments conducted during chemical lithiation and delithiation, it was concluded that LiFePO₄ and FePO₄ were the end members formed and a first order phase transformation took place between them during discharge and charge process. The electrochemical cycling results showed the excellent reversibility of LiFePO₄ and it was attributed to the similarity in the structures of FePO₄ and LiFePO₄. FePO₄ phase and LiFePO₄ phase belong to the same space group, but FePO₄ is isostructural with heterosite and LiFePO₄ is isostructural with triphylite. The volume change between the two phases was reported as 6.81%. During the electrochemical cycling, LiFePO₄ was found to have a reversible capacity of 120 mAh/g, which was much lower than that of its theoretical capacity (170 mAh/g). In addition to the low

reversible capacity at room temperature, LiFePO_4 was found to exhibit capacity loss at high currents, i.e. low rate capability. This was attributed to the diffusion limitations in the three-dimensional structure of LiFePO_4 . In spite of its low reversibility and capacity loss, LiFePO_4 had gained lot of interest in scientific community and many research groups had started to work on this material.

Armand et al. [10-12] were the first group to show that the low reversible capacity and the capacity loss at high currents, were due to the low electronic conductivity of LiFePO_4 . In their work, full theoretical capacity was achieved at 80°C in a polymer electrolyte cell by coating an electronically conducting layer on LiFePO_4 . Based on the same concept, Huang et al. [13] have achieved a reversible capacity of 162 mAh/g at C/10 rate current (10 h charge/discharge) and a reversible capacity of 120 mAh/g at 5C rate current (12 min charge/discharge) at room temperature. These results show a great improvement in the reversible capacity at low currents and as well as at high currents. This improvement was attributed to nano size LiFePO_4 and the conductive carbon present in the electrode. From the comparison of electrochemical performance of various LiFePO_4 samples, it was concluded that the nature of carbon and the contact of carbon with LiFePO_4 particles is very critical to improve the electronic conductivity and thereby to improve the rate capability [13]. Similar conclusions were drawn from Raman microprobe spectroscopic analysis on carbon coated LiFePO_4 samples [14].

Although the above approaches (coating particles with carbon [10-12] and co-synthesizing the compounds with carbon [13]) were successful in improving the rate capability, these approaches do not increase the lattice electronic conductivity or chemical diffusion coefficient of lithium within the crystal [15]. It may be possible that

the increase in electronic conductivity of LiFePO₄ by above approaches is a surface effect. Also adding carbon to the electrode decreases the energy density by considerable amount.

To overcome these problems, Chung et al. [15] has made an effort to improve the electronic conductivity by doping supervalent cations into LiFePO₄ lattice. Supervalent cations used were Mg²⁺, Al³⁺, Ti⁴⁺, Zr⁴⁺, Nb⁵⁺, and W⁶⁺. From the conductivity measurements, it was observed that the undoped LiFePO₄ had an electronic conductivity of 10⁻⁹ – 10⁻¹⁰ S/cm and doping supervalent cations had resulted in conductivities higher than 10⁻³ S/cm [15]. Using the four-point microcontact technique on these samples, it was concluded that the increased conductivity was a bulk effect [16]. During charge/discharge process, Nb doped LiFePO₄ (Li_{0.99}Nb_{0.01}FePO₄) exhibited a reversible capacity of 70 mAh/g at 21.5C rate current and 30 mAh/g at 40C rate current [15].

Among all the doped samples, Zr doped LiFePO₄ (Li_{0.99}Zr_{0.01}FePO₄) was found to have high rate capability. During the charge/discharge process, Li_{0.99}Zr_{0.01}FePO₄ showed a discharge capacity of 120 mAh/g at 20C rate current (3 min charge/discharge) and 75 mAh/g at 50C rate current (1.2 min charge/discharge) [17]. The ability of these doped LiFePO₄ samples to be discharged at very high currents was attributed to the high electronic conductivity of these samples [15,17]. The high electronic conductivity of the supervalent cation doped samples was due to Fe₂P/Fe₃P formed during the material preparation, which acted as conductive paths for electrons [18]. During the heat treatment process in electrode material preparation, carbon present in the iron precursor reacted with LiFePO₄ leading to formation of Fe₂P or Fe₃P. Similar to the work reported by Chung et al. [15], efforts were made to improve the electronic conductivity by dispersing

metals such as copper and silver in LiFePO₄ [19]. However, the rate capability of these electrodes was much lower than that of Li_{0.99}Zr_{0.01}FePO₄ electrode. From the above-mentioned results, it is evident that the rate capability of LiFePO₄ can be improved by increasing its electronic conductivity.

The second approach presented in the literature to increase the rate capability was to increase the Li-ion conductivity and Li⁺ ion diffusion coefficient. Using this approach, Wang et al. [20] has made an effort to improve the rate capability of LiFePO₄ by doping bivalent cations (Ni, Co, Mg) into Fe site in LiFePO₄. The electrochemical performance of doped LiFe_{0.9}M_{0.1}PO₄ (M= Ni, Co, Mg) samples was compared with the electrochemical performance of carbon coated LiFePO₄. At room temperature and at 10C rate, LiFe_{0.9}M_{0.1}PO₄ (M= Ni, Co, Mg) samples showed discharge capacities of 81.7, 90.4 and 88.7 mAh/g, respectively, which were higher than that of carbon-coated LiFePO₄ (54.8 mAh/g). Here it should be noted that the electronic conductivity of these Fe site doped samples (1.0×10^{-7} S/cm, 8.8×10^{-8} S/cm and 2.2×10^{-7} S/cm) were 3 - 4 orders of lower magnitude than that of carbon coated LiFePO₄ (4.0×10^{-4} S/cm). In spite of their low electronic conductivity, the high rate capability shown by the doped samples is in contradiction with the previous conclusion that the rate capability is strongly dependant on electronic conductivity. From the X-ray photoelectron spectroscopy (XPS) experiments conducted on the doped and undoped samples it was concluded that the high rate capability of doped samples was due to the weakening of Li-O interactions by doping, which resulted in high Li-ion conductivity and diffusion coefficient.

To find out the effect of electronic conductivity and Li-ion conductivity on rate capability of LiFePO₄, Wang et al. [21] prepared three LiFePO₄ samples, which were Li-

ion conductive, electron conductive, and mixed conductive, and compared their rate capabilities. The electronic and ionic conductivities were measured by conductive impedance analysis using a blocking electrode. $\text{LiFe}_{0.95}\text{Mg}_{0.05}\text{PO}_4$ electrode was considered as mixed conductor, as it had an electronic conductivity of 1.65×10^{-4} S/cm and Li-ion conductivity of 1.79×10^{-4} S/cm. $\text{LiFe}_{0.95}\text{Ni}_{0.05}\text{PO}_4$ electrode was considered as an electronic conductor, as it had an electronic conductivity of 6.4×10^{-3} S/cm and Li-ion conductivity of 5.04×10^{-5} S/cm. LiFePO_4 electrode was considered as a Li-ion conductor, as it had an electronic conductivity of 3.7×10^{-9} S/cm and Li-ion conductivity of 5.0×10^{-5} S/cm. When tested for the rate capability, the mixed conductor $\text{LiFe}_{0.95}\text{Mg}_{0.05}\text{PO}_4$ electrode had shown the highest rate capability among all the samples. The high rate performance of this electrode was attributed to balanced electronic and ionic conductivity. The mechanism for high rate performance of $\text{LiFe}_{0.95}\text{Mg}_{0.05}\text{PO}_4$ electrode was explained as follows:

“The Li ion diffusion in LiFePO_4 is always associated with electron transport phenomena, and the internal electric field generated by electrons drastically enhances its migrations. For LiFePO_4 , the lithium ions and electrons are considered to form as a dilute binary electrolyte [22]. Therefore, the effective diffusion coefficient due to the diffusion and migration can be written as [22]” [21]

$$\hat{D} = \frac{2D_e D_i}{D_e + D_i} \quad (2.1)$$

where D_i and D_e are the ionic and electronic diffusion coefficients, respectively. A similar equation for the effective diffusion coefficient is given by Reiss [23]

$$\hat{D} = \frac{k\sigma_e\sigma_i}{\sigma_e + \sigma_i} \quad (2.2)$$

where σ_i and σ_e are the ionic and electronic conductivities, respectively. From Eqs. 2.1 and 2.2, it is evident that effective diffusion coefficient is proportional to the electronic conductivity and ionic conductivity in parallel. As a result, if the ionic or electronic conductivity is low in LiFePO_4 , the diffusion will be sluggish. Hence, it is equally important for an electrode to possess high electronic conductivity and ionic conductivity to achieve high rate capability. However, for LiFePO_4 mixed with carbon, the ionic conductivity plays much important role in determining the rate capability [21].

The third approach presented in the literature to increase the rate capability was to improve the rate of phase transformation, i.e. phase transformation kinetics. As mentioned earlier, the high-rate performance of super-valent cation doped LiFePO_4 has been attributed to the improved electronic conductivity [15]. However, later it was found that the high-rate capability of doped LiFePO_4 is also affected by the fast rate of phase transformation [24,25]. From the galvanostatic intermittent titration technique (GITT) and potentiostatic intermittent titration technique (PITT) experiments conducted on super-valent cation doped LiFePO_4 and conventional LiFePO_4 , the high rate capability of super-valent cation doped LiFePO_4 was attributed to the extended solid solution (larger single phase region) of super-valent cation doped LiFePO_4 , which has resulted in formation of a strained coherent interface between the two phases. Formation of the strain coherent interface has further resulted in improved phase transformation kinetics. From these results, it was proposed that the LiFePO_4 materials with higher solid solution limits would have high rate capability. It was also proposed that with the decrease in particle size of LiFePO_4 , there would be an increase in the solid solution limit of LiFePO_4 , therefore resulting in an increase of rate capability [26]. The critical role of the solid

solution range in improving the electrochemical performance is also evident from the better electrochemical performance of Mn^{+2} doped LiFePO_4 [27,28]. The partial substitution of Fe in LiFePO_4 by Mn^{+2} [28] was also found to increase the solid solution range.

The importance of rate of phase transformation is also evident from higher rate capability of $\text{Li}_4\text{Ti}_5\text{O}_{12}$. $\text{Li}_4\text{Ti}_5\text{O}_{12}$ electrode is a spinel oxide and was introduced in early 1990s as a promising electrode for Li-ion batteries [29-31]. Similar to LiFePO_4 , $\text{Li}_4\text{Ti}_5\text{O}_{12}$ electrode is also a phase transformation electrode, as it undergoes a first order phase transformation between $\text{Li}_4\text{Ti}_5\text{O}_{12}$ phase and $\text{Li}_7\text{Ti}_5\text{O}_{12}$ phase. The Li insertion potential of $\text{Li}_4\text{Ti}_5\text{O}_{12}$ electrode is 1.55 – 1.56 V vs. Li and the theoretical capacity is 175 mAh/g. The rate capability of $\text{Li}_4\text{Ti}_5\text{O}_{12}$ electrode is much higher than that of LiFePO_4 , although it has low electronic conductivity ($\sim 10^{-8}$ S/cm) and relatively low Li-ion conductivity ($\sim 10^{-5}$ S/cm) [32] compared to LiFePO_4 . At 10C rate, $\text{Li}_4\text{Ti}_5\text{O}_{12}$ electrode exhibits a discharge capacity higher than 140 mAh/g, which corresponds to a rate capability higher than 80% [33-35]. The high rate capability of $\text{Li}_4\text{Ti}_5\text{O}_{12}$ was attributed to 0% volume change of $\text{Li}_4\text{Ti}_5\text{O}_{12}$ [31] occurring during the phase transformation in charge/discharge process, which results in a rapid phase transformation rate. These results show the importance of volume change and rate of phase transformation in determining the rate capability of phase transformation electrodes.

Apart from increasing the electronic conductivity, ionic conductivity and the solid solution range, another technique widely used to increase the rate capability of LiFePO_4 is to reduce the particle size to the nano meter range. Sides et al. [36] has prepared a thin film nanocomposite $\text{LiFePO}_4/\text{Carbon}$ cathode consisting of monodispersed nanofibers of

LiFePO₄ electrode material mixed with an electronically conductive carbon. On discharge, this electrode showed a capacity of 165 mAh/g at 3C rate and a capacity of 60 mAh/g at 65C rate. The rate capability shown by the nanocomposite LiFePO₄/Carbon cathode is the highest rate capability reported in the literature for LiFePO₄. The excellent rate capability was due to the nanometer Li⁺ ion diffusion length and the increased electronic conductivity from carbon matrix. Similarly, a powdered electrode prepared from LiFePO₄ nanoparticles (40 nm) showed a discharge capacity of 45 mAh/g at 60 C rate [37]. Similarly, Delacourt et al. [38] have shown that high rate capability can be achieved for LiFePO₄ without carbon coating by reducing the particle size to 140 nm. From the comparison of electrochemical performance of LiFePO₄ samples from various research groups and simple theoretical model, it was also concluded that the electrode resistance for LiFePO₄ based cathode materials depends only on mean particle size [39], i.e. rate capability is strongly dependant on particle size of LiFePO₄.

These results demonstrate the importance of electronic conductivity, Li⁺ ion conductivity, rate of phase transformation, solid solution range, volume change, and particle size in determining the rate capability. However, due to the lack of a theoretical study on the kinetics of LiFePO₄, the role of these properties on charge/discharge behavior as well as how to further improve the rate performance of LiFePO₄ are still not clear and needs further investigation. Hence, a systematic study on the influence of these factors on rate performance of LiFePO₄ is critical for attaining further improvement in the rate capability and can be assisted through the development of a mathematical models.

2.2 Mathematical Modeling: Brief Review of Efforts

Developing new electrode materials or improving the electrochemical performance of existing electrode materials require in depth understanding of transport and reaction processes occurring in electrodes. A mathematical model validated by experiments is a very useful tool to identify the rate-controlling mechanisms and estimate the cell performance for design, scale-up, and also optimization. Various models exist in the literature that use a macro homogenous approach to describe the charge/discharge processes in Li-ion cells [40-44]. Reviews of available mathematical models for Li-ion batteries are given in [45, 46, 47]. These models consider various processes such as transport of charge across both the electronic and ionic phases in a porous electrode, transport of mass in the ionic phase, reactions at electrode/electrolyte interfaces, and transport of Li ions in the solid particles. These models are generally valid for any ion insertion electrodes. However, they are not easily adaptable to LiFePO_4 cathode materials, as LiFePO_4 undergoes a phase transformation during charge/discharge process and the phase transformation process is not considered in these models. Different from the above-mentioned models, and to this author's knowledge, the shrinking core model is the only model available in the literature that considers the phase transformation and it is applicable to LiFePO_4 cathode material. The details of shrinking core model are discussed in the following section.

2.3 Shrinking Core Model (SCM) for Phase Transformation Electrodes

Solid-fluid reactions are generally encountered in a variety of chemical process industries. Applications are also found in the fields of extractive metallurgy, control of gaseous pollutants, combustion of solid fuels, and catalyst manufacture. The most important model developed for non-catalytic solid fluid reactions is the shrinking core model (SCM). The SCM was first developed by Yagi et al. [48] in 1955. The detailed derivation of the SCM can be found in [49, 50].

The mechanism-taking place in a phase transformation electrode during the charge/discharge process is similar to the mechanism occurring in non-catalytic heterogeneous solid fluid reactions. In general, a surface reaction of solid-fluid systems consist of the following steps: (1) diffusion of the fluid reactants across the fluid film surrounding the solid, (2) diffusion of the fluid reactants through porous solid layer, (3) adsorption of the fluid reactants at the surface, (4) chemical reaction with the solid surface, (5) desorption of the fluid products from the solid reaction surface, and (6) diffusion of the product away from the reaction surface through porous solid media and through the fluid film surrounding the solid [51]. This phenomenon was successfully illustrated using SCM [51]. Since charging/discharging process of a phase transformation electrode results in growth/disappearance of a new phase/an existing phase by means of diffusion and reaction (phase transformation), SCM can also be used to illustrate the phenomenon. Subramanian et al. [52] used such an approach to predict the discharge behavior of metal-hydride electrode, which also undergoes phase transformation during the charge/discharge process.

Similarly, Srinivasan et al. [53] used the SCM to predict the discharge behavior of a LiFePO_4 electrode. The development of this model was based on three assumptions:

- (i) The phase transformation process is very fast and the discharge kinetics is controlled by a two-dimensional spherical diffusion process. It also implies that diffusion is the slowest process among all the processes taking place in LiFePO_4 during discharge. As a result, Li^+ ion content in α phase at the interface and Li^+ ion content in β phase at the interface are equal to equilibrium concentrations $C_{\alpha\beta}$ and $C_{\beta\alpha}$, respectively.
- (ii) Volume change during the phase transformation is neglected.
- (iii) LiFePO_4 particles are considered of spherical shape.

In general the discharge curve of LiFePO_4 can be divided into three regions: initial solid solution region, phase change region, and final solid solution region. In the initial solid solution region the particle to be discharged is full of α phase. In the phase change region, both α and β phase co-exist in the particle. In the final solid solution region, the particle is full of β phase. In addition to the above-mentioned assumptions, and for simplifying the model development, the initial single-phase/solid solution region and α phase in phase change region was neglected in SCM. The governing equation, the initial conditions, and boundary conditions for the SCM [53] are given as follows:

For the phase change region, the transient-diffusion equation with radial symmetry becomes:

$$\frac{\partial C_{\beta}}{\partial t} = D_{\beta} \left(\frac{\partial^2 C_{\beta}}{\partial r^2} + 2 \frac{\partial C_{\beta}}{\partial r} \right) \quad (2.3)$$

If no β phase is present at the beginning of the discharge process, thus:

$$C_{\beta} = 0 \text{ at } t = 0 \quad (2.4)$$

The following are the two boundary conditions required for the diffusion part:

$$D_{\beta} \frac{\partial C_{\beta}}{\partial r} = \frac{i}{F} \text{ at particle surface } (r = R_p) \quad (2.5)$$

$$C_{\beta} = C_{\beta\alpha} \text{ at the interface } (r = r_c) \quad (2.6)$$

However, the interface location is not known since it is a moving front (shrinking core model).

The unknown interface position can be evaluated by doing a mass balance of Li^+ ions at the interface, which is given by the following equation:

$$-C_{\beta\alpha} \frac{dr_c}{dt} = D_{\beta} \left(\frac{\partial C_{\beta}}{\partial r} \right)_{r=r_c} \text{ at the interface } (r = r_c) \quad (2.7)$$

When the interface reaches the center of the particle, i.e. when the particle is full of β phase, the particle enters into the solid solution region. Under these conditions the differential model given by Eqs. (2.3-2.7) reduces to

$$\frac{\partial C_{\beta}}{\partial t} = D_{\beta} \left(\frac{\partial^2 C_{\beta}}{\partial r^2} + 2 \frac{\partial C_{\beta}}{\partial r} \right) \quad (2.8)$$

$$D_{\beta} \left(\frac{\partial C_{\beta}}{\partial r} \right) = \frac{i}{F}, \text{ at particle surface } (r = R_p) \quad (2.9)$$

$$\frac{\partial C_{\beta}}{\partial r} = 0, \text{ at particle center } (r = 0) \quad (2.10)$$

where C_β is the Li-ion concentration in the iron phosphate/LiFePO₄ lattice, r is the radial position in the electrode, t is time in seconds, r_c is the radial position of the α/β interface, R_p is the radius of the particle, $C_{\beta\alpha}$ is the equilibrium concentration of the lithium rich (β) phase at the interface, i is the reaction current applied across the surface, F is the Faraday's constant, and D_β is diffusion coefficient of Li in the Li rich (β) phase. The initial condition for Eq. 2.8 is the lithium concentration profile inside the β phase at the end of the phase change region. Eqs. 2.3-2.10 were converted to dimensionless form and solved to obtain the dimensionless surface concentration of LiFePO₄ particle. From the dimensionless surface concentration, the equilibrium potential, the over-potential, and the voltage of LiFePO₄ cathodes were calculated. The details on calculation procedure can be found in [53].

2.4 Validation of SCM

To validate the SCM, the discharge behavior of LiFePO₄ samples were predicted from SCM and were compared with the experimental results [53]. Generally, in the field of batteries, a mathematical model is said to be validated if the model is able to reasonably predict the discharge curves of an electrode at different current densities. The discharge curve of LiFePO₄ has three different regions: initial descending line, horizontal plateau, and final descending line. The slope and length of these three lines differ from one LiFePO₄ sample to another LiFePO₄ sample, depending on the type of material preparation process and electrode preparation process. Also the discharge curves at different current densities vary from one sample to another sample. Hence, it is essential

to validate the model by predicting the discharge behavior of at least two or more samples, before using the model for further analysis.

Figure 2.1 shows the experimental discharge curves of a LiFePO_4 sample and the predicted results from shrinking core model (reported in [53]). From Figure 2.1, it is evident that the shrinking core model is able to predict the discharge behavior at a current density of 1.3 mA/cm^2 . However, it over-predicts the discharge behavior at 0.26 mA/cm^2 and it under-predicts the discharge behavior at 2.6 mA/cm^2 . These results show the inability of shrinking core model in predicting the discharge behavior of LiFePO_4 sample. The proposed reason (by Srinivasan et al.) for the disagreement between experimental and model results was the large particle size distribution present in the sample [53].

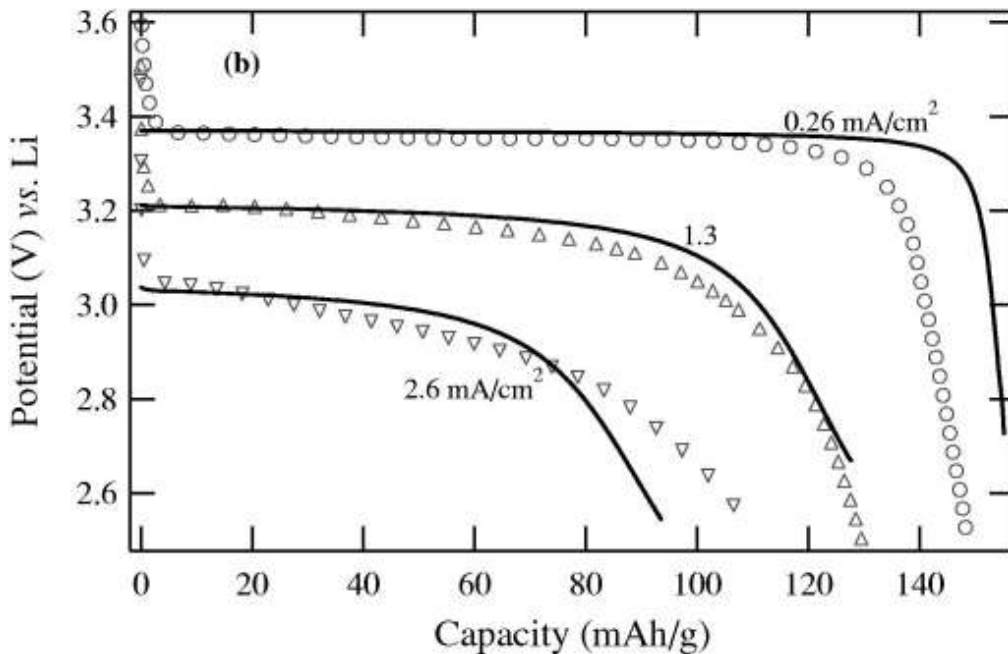


Figure 2.1: Discharge curves of a LiFePO_4 sample at different current densities: Experimental (symbols) and Shrinking core model Predictions (lines) (figure taken from ref. 53)

However, the above-proposed reason is not valid for all LiFePO_4 samples, as some of the samples may have narrow particle size distribution. Thus, it is crucial to identify the actual reason for the discrepancy between experimental results and the results obtained from SCM. Also, it is important to determine the controlling mechanism for charge/discharge process of LiFePO_4 by experimental techniques and to cross check the applicability of shrinking core model to phase transformation electrode materials. Based on those results, SCM needs to be modified, which is the main objective of this doctoral dissertation work. With the aid of this modified shrinking core model and experimental approaches, the effects of various properties of phase transformation electrodes such as chemical diffusion (electronic conductivity and the Li-ion conductivity), the phase transformation kinetics, the solid solution range, volume change, and the particle size on the rate capability of electrode materials will be determined.

CHAPTER 3

EXPERIMENTAL METHODOLOGY

In this chapter, a brief description of equipment used is given. The methods used for preparation of LiFePO_4 cathode and Li-ion half-cells are also explained. Procedures for conducting galvanostatic charge/discharge test, galvanostatic intermittent titration technique (GITT), and potential step chronoamperometry (PSCA) measurement are also discussed.

3.1 Equipment Description

3.1.1 Glove Box

An OMNI Lab glove box (Vacuum Atmospheres Company) connected to an Argon gas cylinder was used to create inert atmosphere in order to store oxygen sensitive and moisture sensitive materials such as lithium. All the operations related to these materials and assembling of all Li ion half-cells were done inside the glove box. As shown in Figure, glove box mainly contains an antechamber, reaction or storage chamber, and gas purifier. Initially, all the materials are transferred to antechamber from outside. After transferring, the antechamber is vacuumed thrice to maintain inert atmosphere. Then the material is transferred to storage chamber. Before and after transferring, the antechamber valves are always closed. The glove box is not continuously

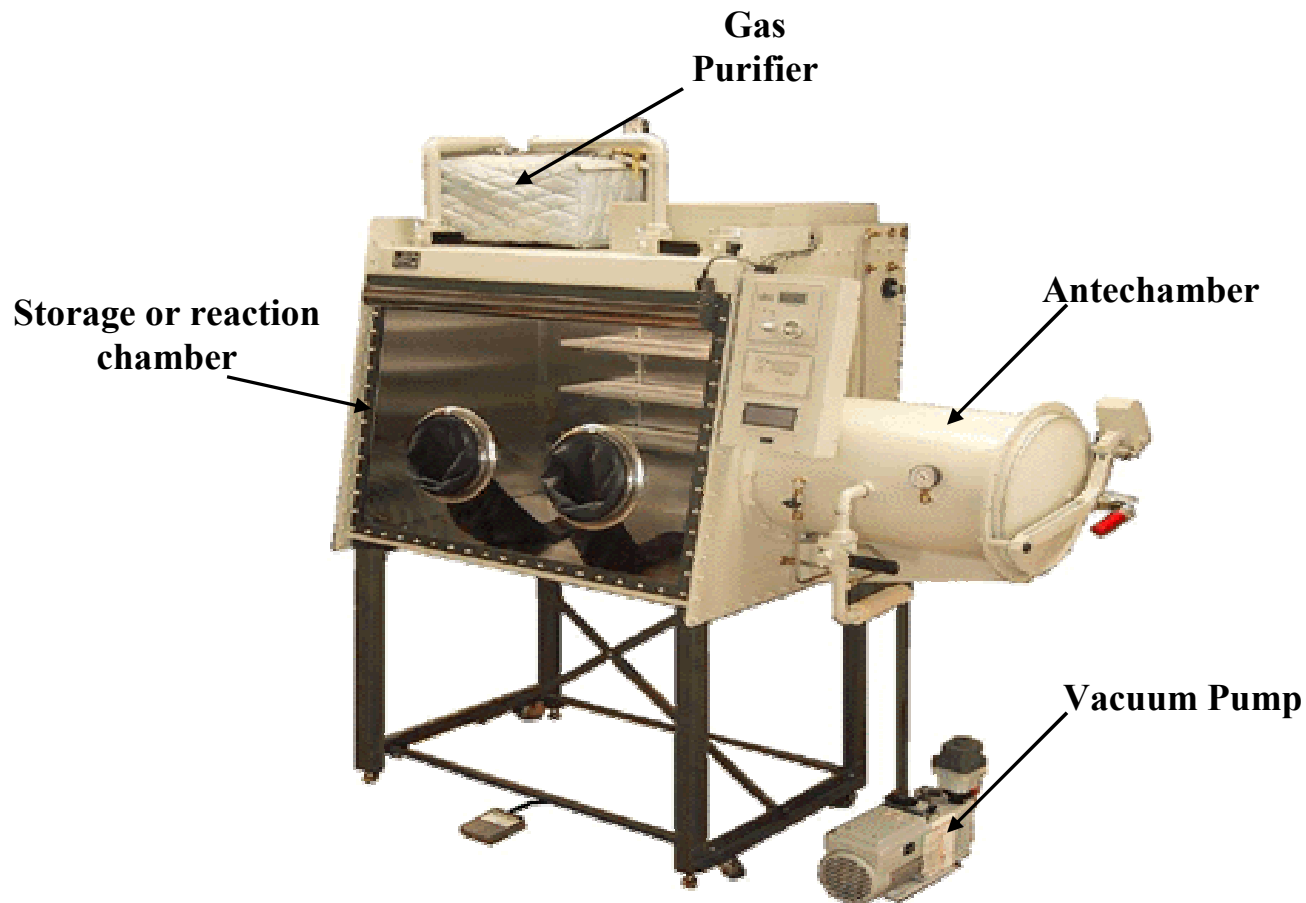


Figure 3.1: Glove Box

purged with Argon gas. But the gas purifier present in the glove box removes the oxygen and trace moisture contamination.

3.1.2 Hand-Operated Closing Tool

Electrochemical testing of LiFePO_4 cathodes for Li ion batteries is done in CR 2032 coin cells. Apart from cathode, Li metal electrode, separator, and electrolyte, the coin cell's internal parts are shown in Figure 3.2(a). Assembling of coin cells is generally

done inside the glove box using a hand-operated closing tool (Hohsen Corporation), which is shown in Figure 3.2(b).

Assembling Coin Cell:

First of all, the gasket is placed inside the coin case and then Li metal, separator, liquid electrolyte, cathode or working electrode, stainless steel plate, spring, and cap are kept in the order to form a cell. Once the cell is assembled, the lever for hand-operated tool is lifted and held up to keep the cell on the bottom mold of the operating tool. Then the lever is pushed down until there is firm resistance from it and then it is held for a while. Then the lever is lifted up and the closed cell is taken out.

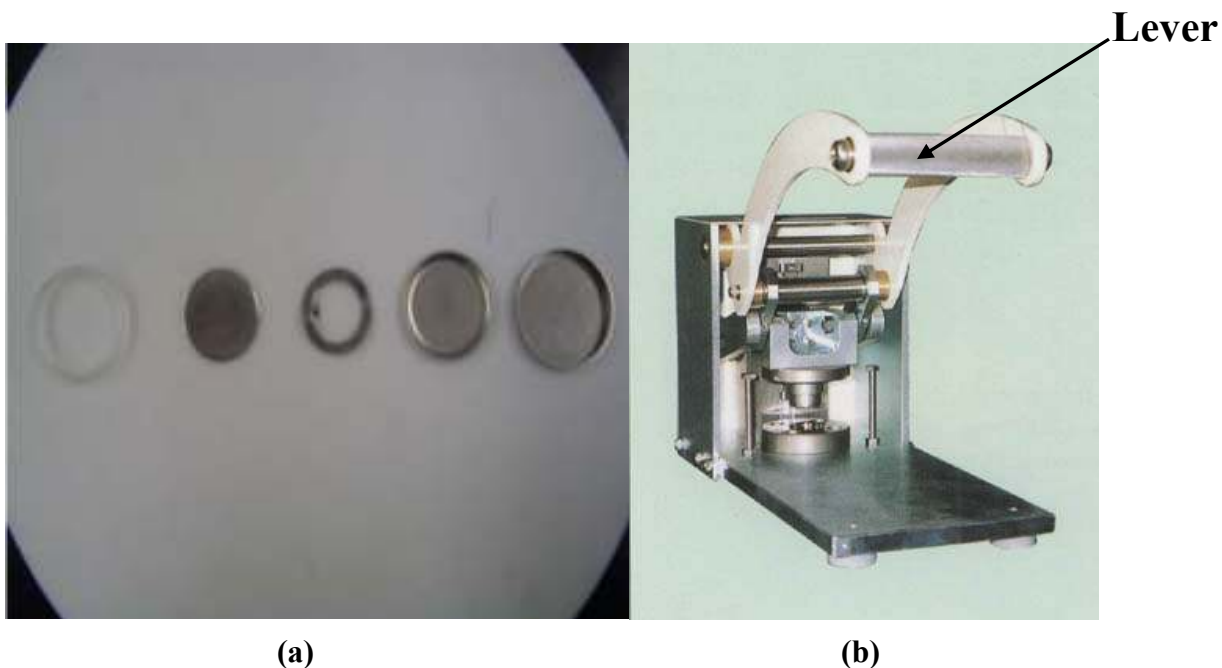


Figure 3.2: (a). Parts of Coin cell (From left: Rubber gasket, stainless steel plate, stainless steel spring, cap, coin case) (b) Hand-Operated Closing Tool.

3.1.3 Battery Testing Machine

Assembled batteries are charged-discharged using an Arbin battery test station (Arbin Instruments), which is shown in Figure 3.3. The test station has 16 independently controllable channels, which are fully functional potentiostats/galvanostats by nature. This potentiostat/galvanostat functionality allows us to perform broad electrochemistry work, which involves the use of reference electrodes. This testing station can be operated over a wide range of currents, voltage, and power. Channels can also be paralleled to increase the current output. All the operations on this testing station are controlled automatically by MITS PRO software, which is installed in the computer connected to the testing station.



Figure 3.3: 16-Channel BT2000 Battery Testing System

3.1.4 AC Impedance Spectroscopy

Impedance measurements related to cathode materials are done by electrochemical impedance spectroscopy. The testing device is shown in Figure. It includes of a Solartron 1287 Potentiostat, 1260 Impedance/Gain phase analyzer and a computer for data acquisition. Z plot software (Scribner Associates) is used for conducting the impedance tests automatically. A maximum polarization of 14.5V/2A can be obtained by using the 1287 Potentiostat and a frequency range of 10 μ Hz-1MHz can be maintained by using the 1260 impedance/Gain-phase analyzer.

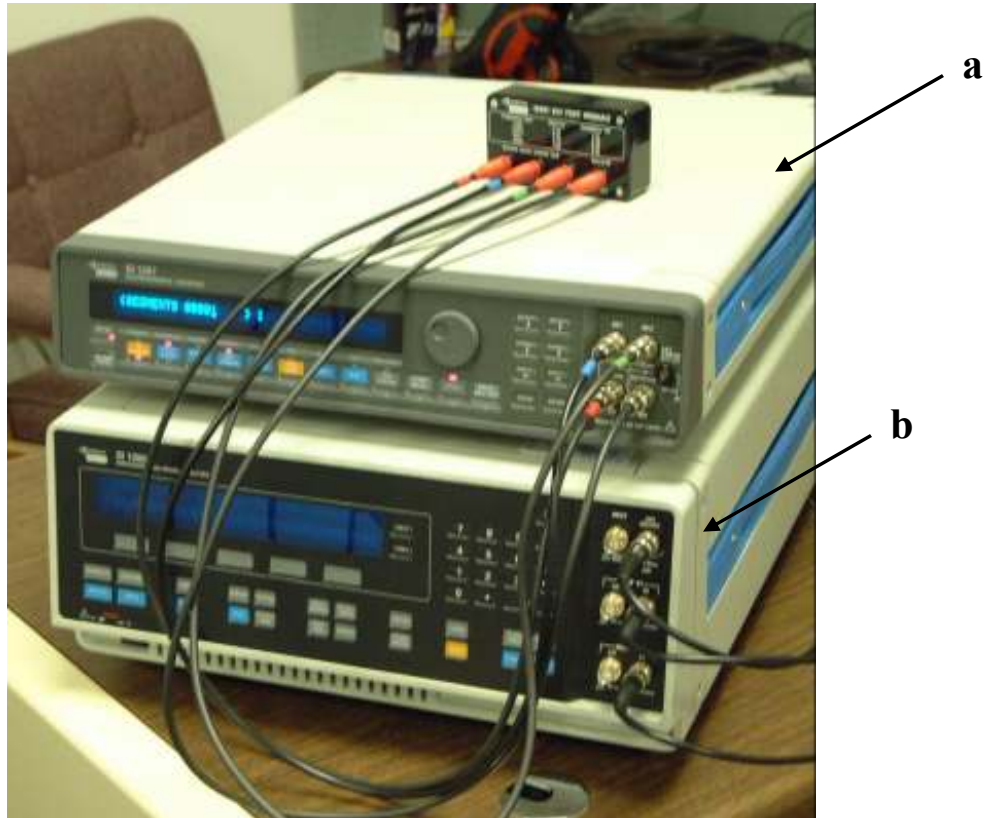


Figure 3.4: (a) Galvanostat/Potentiostat (b) Impedance/Gain Phase Analyzer

3.2 Electrode Preparation

Two different carbon-coated LiFePO₄ materials (samples A and B) as received from the industrial suppliers are used in this study. These two samples have a narrow particle size distribution and their mean particle radius is 0.8 μm. LiFePO₄ active materials as received from industrial suppliers are mixed with different amounts of carbon black (0, 5wt% and 10wt%) and 10wt% polyvinylidene fluoride (PVDF, KynarTM, Elf-Atochem) in 1-methyl-2-pyrrolidinone solvent to form a viscous paste, which is then homogenized in an ultrasonic bath for 30 minutes. The paste obtained by this procedure is coated on a carbon-coated Al mesh circular discs (geometric surface area of 1.5 cm²). The discs are then dried in a vacuum oven at 120°C for 12 hours. After the material was cooled down to room temperature, the disc electrodes were pressed with a pressure of 1 tonnes/cm² and used as electrodes. The active material loading on the electrodes was about 5 mg/cm². Using LiFePO₄ electrode prepared on Al mesh as working electrode (WE), Li foil as counter electrode (CE) and reference electrode (RE), 3-electrode PTFE cells are prepared. Schematic of 3-electrode PTFE cell is shown in Figure. All the cells prepared in this work are assembled in an argon-filled glove box, with 1.0 M LiPF₆ in EC-DEC-DMC-EMC (1:1:1:3 by volume) (Ferro Corporation) as liquid electrolyte, and polypropylene (PP) microporous film as the separator.

LiFePO₄/A and LiFePO₄/B electrodes with and without 10wt% carbon black addition are used for exchange current density measurement with the aid of electrochemical impedance and linear polarization (1mv/s) at 50% state of discharge. LiFePO₄/A and LiFePO₄/B electrodes containing 5wt% carbon black are used for

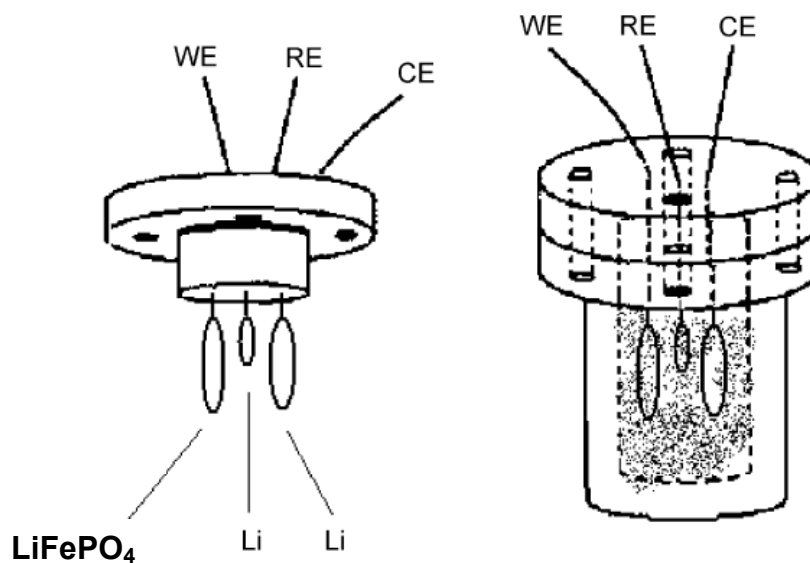


Figure 3.5: Schematic of 3 electrode PTFE cell

obtaining equilibrium discharge potential–composition isotherms. A working electrode with a composition of 88wt% $\text{LiFe}_{0.9}\text{Mg}_{0.1}\text{PO}_4$ powder, 6wt% carbon black, and 6wt% polyvinylidene fluoride is used for potential step chronoamperometry measurement. The procedure for preparation of $\text{LiFe}_{0.9}\text{Mg}_{0.1}\text{PO}_4$ powder can be found in [54].

3.3 Procedure for Conducting Experiments

All the experiments conducted in this work are commonly used standard experiments in the field of electrochemistry. A brief procedure for conducting these experiments is discussed in this subsection.

3.3.1 Galvanostatic Charge/Discharge Test

The discharge curves for sample A and sample B are provided by the industry. The discharge curves were obtained using the following procedure: The galvanostatic charge/discharge test was conducted on CR 2032 coin cells containing LiFePO₄/A and LiFePO₄/B working electrodes with an active material loading of 3 mg/cm² and with a composition of 85wt% LiFePO₄, 5wt% carbon black, and 10wt% PVDF. Before conducting the test at different current densities, all the cells were activated through several charge/discharge cycles with a small current (0.1C, 1C=150mA/g for all the materials studied) by using an Arbin Corporation (College Station, TX) automatic battery cycler. Once the cells were activated, they were charged to an upper cut-off voltage of 4.2 V using a low current (0.1C rate) and discharged to lower cut-off voltage of 2.5 V at different current rates to obtain discharge curves at different current densities. Then the discharge rate capability of the electrode material was evaluated using the ratio of the discharge capacity at a given current to that of discharge capacity at 0.1C current.

3.3.2 Galvanostatic Intermittent Titration Technique (GITT)

The equilibrium discharge potential–composition isotherms (PCI) at room temperature are measured in a 3-electrode PTFE cell using a galvanostatic intermittent titration (GITT) technique at a low current density of 0.02C. The 3-electrode PTFE cells are discharged by using a series of intermittent current values for 1.0 hour. Between each intermittent current, the cells are left at an open circuit for 2.0 hour. The value of the

potential observed after 2.0 h rest time is considered as equilibrium potential. This procedure is repeated until the potential reached a value of 2.5 V.

3.3.3 Potential Step Chronoamperometry (PSCA)

PSCA measurement is conducted on 3-electrode PTFE cells containing $\text{LiFe}_{0.9}\text{Mg}_{0.1}\text{PO}_4$ cathode by using the electrochemical impedance spectroscopy. In this measurement, the potential is changed instantaneously from initial step to final step and the change of current (i) with time is measured. From the current vs. time data, the controlling mechanism for the discharge/charge process is determined.

3.4 Experimental Results of Samples A and B LiFePO_4 Cathodes

3.4.1 Discharge Rate Capability Data for Samples A and B

Figures 3.6 and 3.7 show the discharge curves of sample A LiFePO_4 and sample B LiFePO_4 at different current densities obtained from industry. From these figures, it is evident that sample A and sample B exhibit different discharge characteristics. Discharge curves of Samples A and B differ in voltage plateaus, voltage drop at high currents, and discharge capacities. For example, Sample A has a voltage plateau at 3.385 vs. Li and a voltage drop of 106 mV at 5C rate current, whereas sample B has a voltage plateau at 3.42 vs. Li and a voltage drop of 58 mV at 5C rate current. Also, at 0.1C rate, Sample A has shown a discharge capacity of 132 mAh/g and sample B has shown a discharge capacity of 144 mAh/g. The difference in discharge behavior is also evident at high

currents. Sample A has shown discharge capacities of 116 mAh/g, 106 mAh/g, and 89 mAh/g at 1C, 2C, and 5C rates, respectively, resulting in discharge rate capabilities of 87%, 80%, and 67%, respectively. Whereas sample B has shown discharge capacities of 139 mAh/g, 136 mAh/g, and 130 mAh/g at 1C, 2C, and 5C rates, respectively, resulting in discharge rate capabilities of 96%, 94%, and 90%, respectively. Even at higher currents such as at 10C, and 20C, sample B has shown discharge capacities of 124 mAh/g and 114 mAh/g, resulting in discharge rate capabilities of 86% and 79%, respectively. From the comparison of the discharge capacities of both the samples, it is clear that sample B has high reversible capacity and high discharge rate capability. Throughout this work, the discharge curves of samples A and B (Figure and Figure) are used to validate the mathematical models.

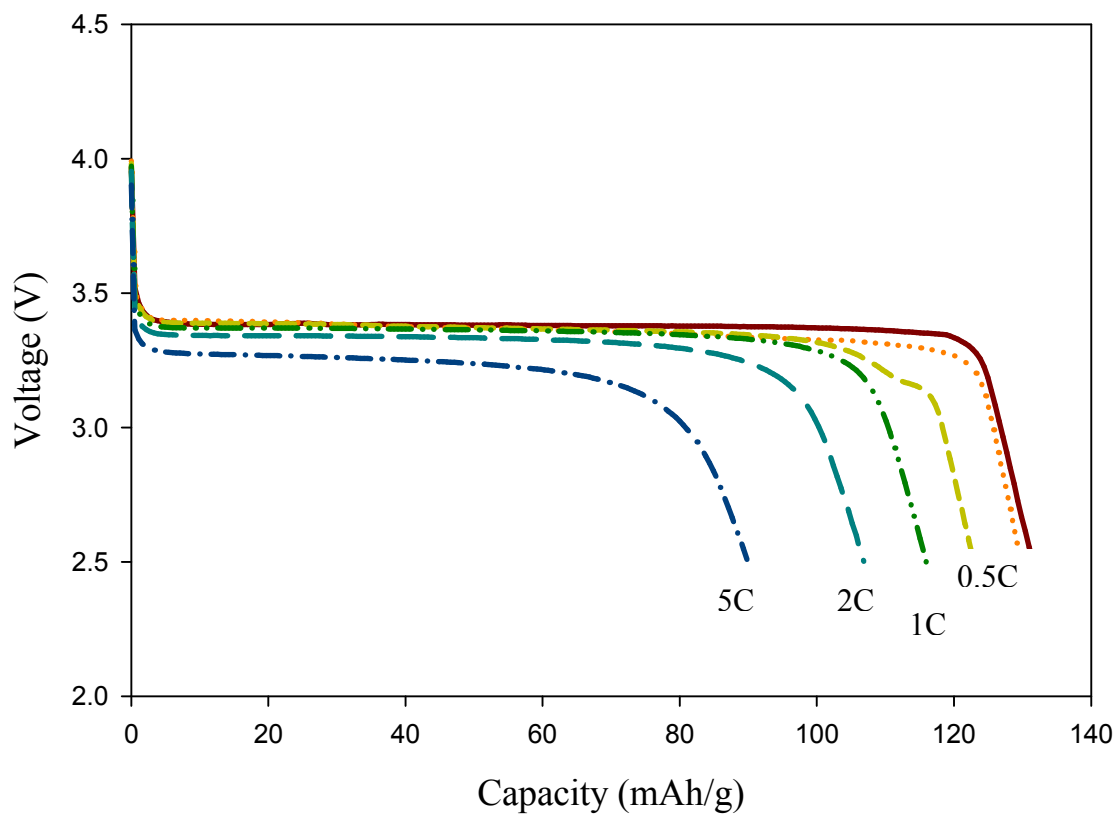


Figure 3.6: Discharge curves of Sample A LiFePO₄ obtained from Galvanostatic charge/discharge test (from left: 5C, 2C, 1C, 0.5C, 0.2C and 0.1C)

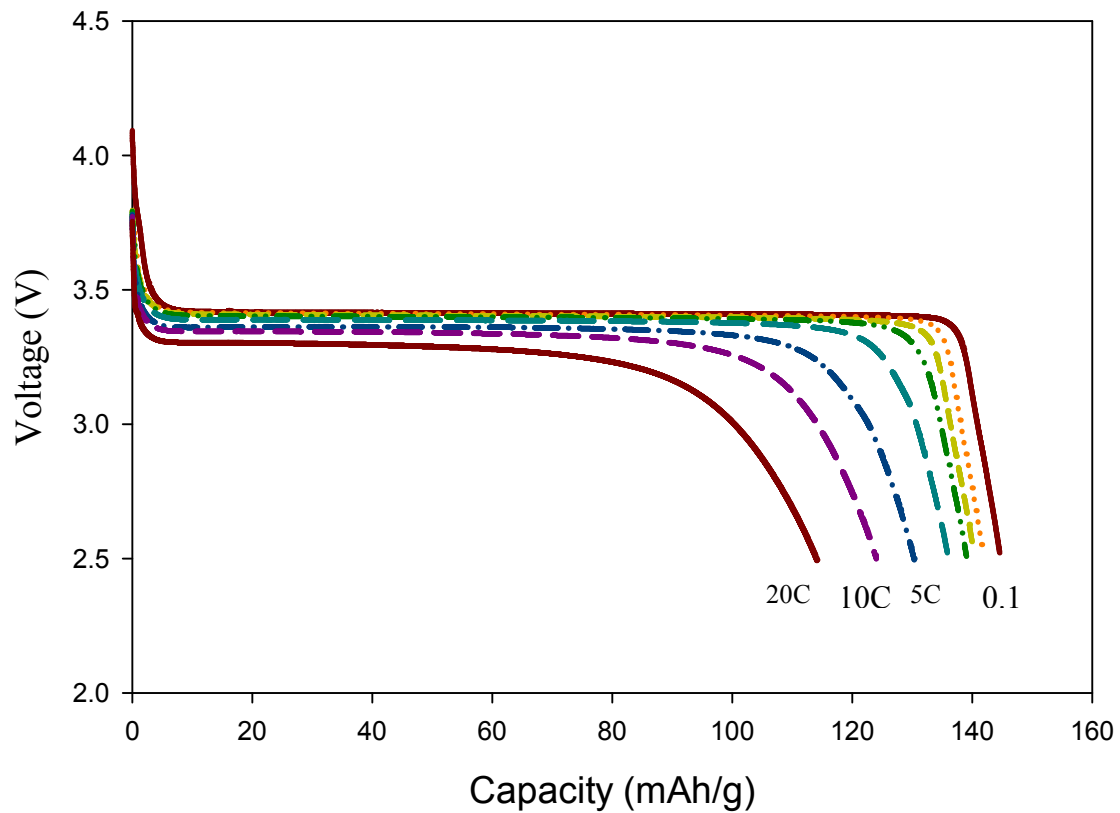


Figure 3.7: Discharge curves of Sample B LiFePO₄ obtained from Galvanostatic charge/discharge test (from left: 20C, 10C, 5C, 2C, 1C, 0.5C, 0.2C and 0.1C)

3.4.2 Equilibrium Potential Composition Isotherms for Samples A and B LiFePO₄

Figure 3.8 and Figure 3.9 show the equilibrium potential curves of sample A and sample B during discharge obtained from GITT experiments. In general, the equilibrium potential curve consists of two descending curves connected by a long plateau. The initial descending line represents the initial single-phase (α phase) or solid solution region. The potential plateau represents the phase transformation region, where the α phase is transformed to β phase. The final descending line represents the other single-phase (β phase) or solid solution region. In equilibrium potential curves, the value of state of discharge at which the voltage plateau starts is considered as equilibrium concentration of lithium deficient (α) phase ($C_{\alpha\beta}$), and the value of state of discharge at which the voltage plateau ends is considered as equilibrium concentration of lithium rich (β) phase ($C_{\beta\alpha}$). $C_{\alpha\beta}$ and $C_{\beta\alpha}$ are also referred to as solid solution limits. In addition to $C_{\alpha\beta}$ and $C_{\beta\alpha}$, the maximum lithium that can be incorporated into FePO₄ lattice (C_t) can be determined from equilibrium potential curve and Faradays law. From these figures, it can be observed that potential plateaus start at potential values of 3.859 V and 3.4245 V for sample A and sample B, respectively. The theoretical capacity of sample A LiFePO₄ measure from GITT is 150 mAh/g and that of sample B LiFePO₄ is 158 mAh/g. From Figure 3.8, the values of $C_{\alpha\beta}$, $C_{\beta\alpha}$, and C_t for sample A are found to be $0.015 \times 0.02044 \text{ mol/cm}^3$, $0.771 \times 0.02044 \text{ mol/cm}^3$, and 0.02044 mol/cm^3 . Similarly, the values of $C_{\alpha\beta}$, $C_{\beta\alpha}$, and C_t for sample B are found to be $0.027 \times 0.02119 \text{ mol/cm}^3$, $0.85 \times 0.02119 \text{ mol/cm}^3$, and 0.02119 mol/cm^3 . Throughout this work the above-mentioned values for $C_{\alpha\beta}$, $C_{\beta\alpha}$, and C_t are used in the mathematical models.

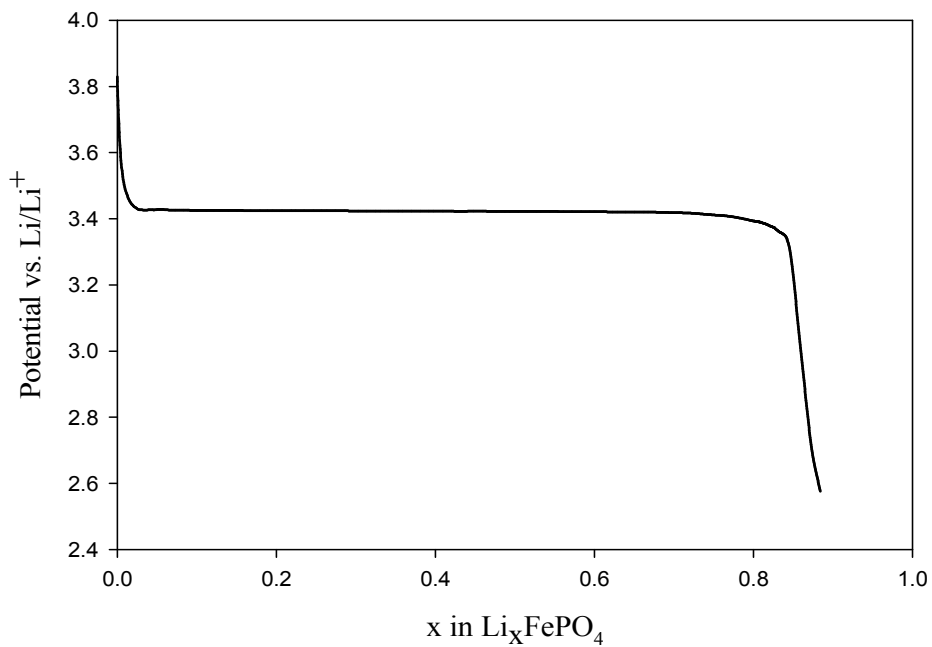


Figure 3.8: Equilibrium Potential Curve of Sample A LiFePO_4 during discharge obtained from GITT experiment

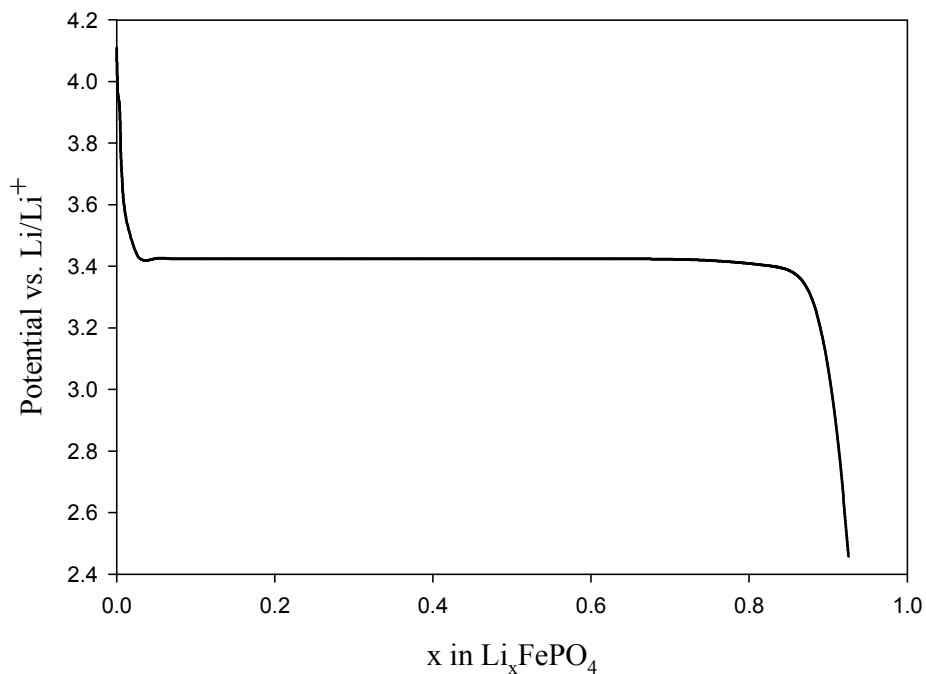


Figure 3.9: Equilibrium Potential Curve of Sample B LiFePO_4 during discharge obtained from GITT experiment

3.4.3 Parameter Values from Experiments

The particle radius ($R_p = 2L_0$) of sample A and sample B LiFePO_4 is determined from SEM observation and it is found to be $0.8 \mu\text{m}$ for both the samples. The obtained value of particle radius for sample A LiFePO_4 from SEM observation is similar to the one reported in the literature [55]. The density (ρ) value (3.6 g/cm^3) and transfer coefficient value (α_1) (0.5) are taken from the literature [53].

The exchange current densities of pure LiFePO_4/A and LiFePO_4/A -10% carbon black electrodes are measured at 50% state of discharge using linear polarization and electrochemical impedance spectroscopy (EIS) experiments. From both the experiments, i_0 value is found to be 0.3 A/g for LiFePO_4/A containing 10% carbon black and 0.007 A/g for pure LiFePO_4/A . Since the LiFePO_4 used for this study has 5% carbon black (which lies between the above mentioned two samples), the exchange current density of 0.1 A/g is used for sample A. Similarly, an exchange current density of 0.25 A/g is used for sample B.

CHAPTER 4

ASSESSMENT OF APPLICABILITY OF SCM TO LiFePO_4

CATHODES

From the literature review, it is evident that the SCM is the only mathematical model that is applicable to phase transformation electrodes such as LiFePO_4 . However, it is also understood that the SCM was not able to accurately predict the discharge behavior of LiFePO_4 sample and the discrepancy between experimental and mathematical modeling results was attributed to particle size distribution. Here we have made an effort to find out the region of applicability of SCM to cathode materials such as LiFePO_4 .

4.1 Assessment by Mathematical Modeling

To confirm the hypothesis that the discrepancy between experimental results and model predictions is due to the large particle size distribution, an effort is made here to predict the discharge behavior of two commercial LiFePO_4 samples (samples A and B) from the SCM. As mentioned earlier, these two samples have very narrow particle size distribution. Hence, SCM should be able to predict their discharge behavior accurately. If the SCM is unable to predict the discharge behavior of these two samples, it implies that the proposed hypothesis is incorrect and the reason for disagreement needs to be investigated. The procedure for obtaining discharge curves from SCM is explained in the following sections.

4.1.1 Solving the SCM

Eqs. 2.3-2.10 are converted to dimensionless form using the following variables.

$$\theta_{\beta} = \frac{C_{\beta}}{C_t} \quad \theta_{\beta\alpha} = \frac{C_{\beta\alpha}}{C_t} \quad \theta_{\beta S} = \frac{C_{\beta S}}{C_t} \quad X = \frac{r}{R_p} \quad X_c = \frac{r_c}{R_p} \quad \tau = \frac{tD_{\beta}}{R_p^2} \quad \delta = \frac{i\rho R_p^2}{D_{\beta} C_t F}$$

The resulting dimensionless equations correspond to a linear moving boundary value problem. This system of equations is solved by using the numerical method of lines (MOL) approach [56,57]. In order to use numerical method of lines, the values of the parameters $C_{\beta\alpha}$, C_t , R_p , ρ , and D_{β} have to be known. The values of the parameters $C_{\beta\alpha}$, C_t , R_p , and ρ , are obtained from experiments (refer to sections 3.3 and 3.4). Since there is no accurate method to determine the value of the parameter D_{β} for phase transformation electrodes, a guess value is given to the parameter D_{β} . Once the values of the parameters are known, the system of equations is discretized in the space domain, thereby converting the system of partial differential equations into a system of differential-algebraic equations (DAE). The resulting system of differential-algebraic equations is then solved by using time-integration techniques. Following this procedure, dimensionless surface concentration as a function of time is determined for a particular current density.

4.1.2 Determining Equilibrium Potential

As mentioned in section 3.4.2, equilibrium potential curves of sample A (Figure 3.8) and sample B (Figure 3.9) are obtained from GITT. To use these data in the model,

an empirical relation between equilibrium potential and state of discharge is obtained by a curve fitting. State of discharge is the dimensionless surface concentration ($\theta_{\beta S}$), which is the ratio of surface concentration ($C_{\beta S}$) to maximum concentration (C_t). The equations for equilibrium potential as a function of state of discharge for samples A and B, obtained from curve fitting, can be expressed as follows:

For Sample A:

$$U = 3.3929 - 0.5 \times e^{\left(-\frac{1.55}{(\theta_{\beta S})^5} + (\theta_{\beta S}) \right)} - 8 \times e^{\left(-\frac{0.52}{(\theta_{\beta S})^4} \right)} \quad (4.1)$$

For Sample B:

$$U = 3.4245 - 0.1 \times e^{\left(-\frac{3}{(\theta_{\beta S})^5} + (\theta_{\beta S}) \right)} - 14 \times e^{\left(-\frac{0.98}{(\theta_{\beta S})^4} \right)} \quad (4.2)$$

Here, the Parameter U corresponds to equilibrium potential of the respective samples. Figure 4.1 and Figure 4.2 show the comparison between experimental results and results obtained from Eqs. 4.1 and 4.2. From these figures, close match between experimental results and the model fit can be seen. As indicated in section 2.3, the initial solid solution curve ($C_{\alpha\beta} = 0$) is not accounted by Eqs. 4.1 and 4.2. The solid phase lithium concentration at the surface ($\theta_{\beta S}$), obtained by solving the system of equations is fed into the Eqs. 4.1 and 4.2 and the equilibrium potential as a function of time is calculated.

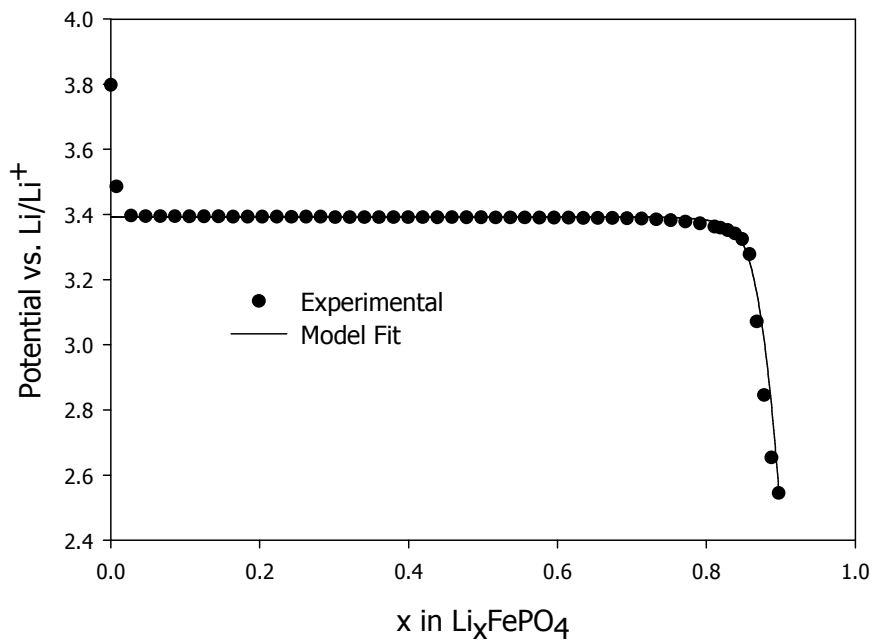


Figure 4.1: Equilibrium Potential vs. Li content x for $\text{Li}_x\text{FePO}_4/\text{A}$ obtained from Experiment and Eq. 4.1

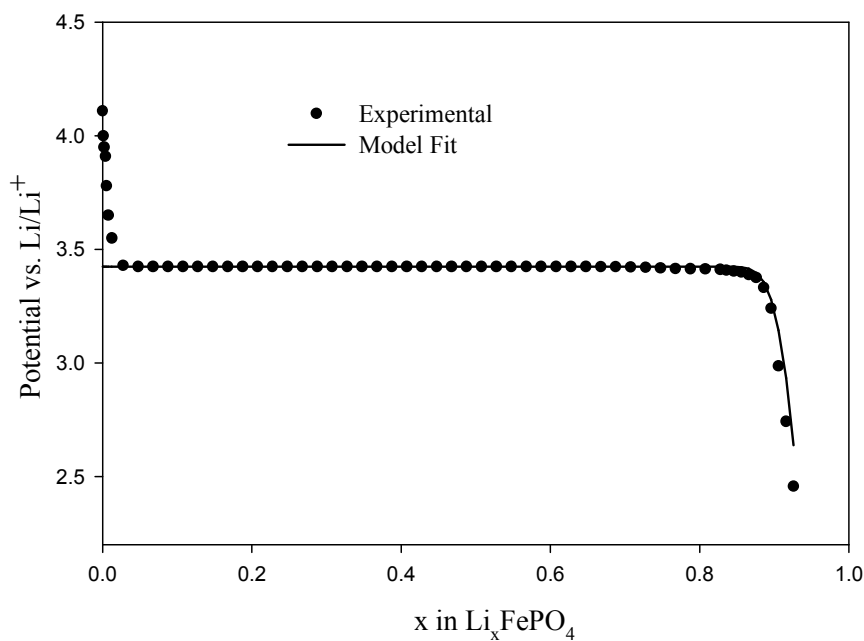


Figure 4.2: Equilibrium Potential vs. Li content x for $\text{Li}_x\text{FePO}_4/\text{B}$ obtained from Experiment and Eq. 4.2

4.1.3 Determining Overpotential and Voltage

Over potential is calculated using following current-overpotential equation [58],

$$i = i_o \left(\frac{(C_t - C_{\beta s})}{(C_t - C_{\beta \alpha})} \times e^{\left(\frac{\alpha_1 F \eta(t)}{RT}\right)} - \frac{C_{\beta s}}{C_{\beta \alpha}} \times e^{\left(-\frac{\alpha_1 F \eta(t)}{RT}\right)} \right) \quad (4.3)$$

where i is the discharge current density used, i_o is the exchange current, α_1 is the transfer coefficient, R is the universal gas constant, T is the temperature, and $\eta(t)$ is the over potential which is a function of time. For a given discharge current density (i), and for known values of i_o and α , the overpotential as a function of time can be determined. The values of i_o and α_1 are determined from experiments (refer to section 3.4.3). The voltage of LiFePO_4 electrodes (A and B) is calculated by adding the overpotential to the equilibrium potential.

4.1.4 Predicting the Discharge Curves of Samples A and B

In order to predict the discharge curves of samples A and B from SCM, the value of the parameter D_β has to be known. Since there is no accurate experimental technique to determine the value of D_β for phase transformation electrodes, a guess value is given. At a particular discharge current density, for a given value of D_β , dimensionless surface concentration as a function of time is determined. From the surface concentration, the equilibrium potential, the over-potential and the voltage during the discharge are determined. If the discharge curve obtained from SCM at a particular current density

matches with the experimental discharge curve at that current density, the guess value given is considered as the real value of the parameter D_{β} . Once the value of the parameter D_{β} is determined, using this value, the discharge curves at other current densities are determined from SCM. In case of mismatch between experimental discharge curves and discharge curves obtained from SCM, the guess value is changed and the above procedure is repeated.

Figures 4.3 and 4.4 show the experimental discharge curves of samples A and B and also the predictions from shrinking core model. For sample A, discharge curve at 1C rate current is used to estimate the value of the parameter D_{β} and for sample B, discharge curve at 5C is used. Similar to the results reported by Srinivasan et al. [53], SCM is not successful in predicting the discharge behavior of these samples (Figures 4.3 and 4.4). For example, SCM is able to predict the end of discharge value for sample A at 1C current but it could not predict the voltage plateau at 1C current and the voltage plateau and end of discharge value at other currents (5C, 2C, 0.5C, and 0.1C). Similarly, the SCM is not able to predict the voltage plateaus and end of discharge values of sample B. From these observations, it is evident that the discrepancy is not due to the particle size distribution of the sample. It may be possible that the discrepancy is due to the restrictive assumption (discharge kinetics is controlled by only diffusion process) used in the model. If the discrepancy is due to the restrictive assumption, the SCM cannot be used for describing the discharge or charge process of phase transformation electrode. Hence, it is essential to determine the controlling mechanism for charge/discharge process of LiFePO_4 by experimental techniques and to cross check the applicability of SCM to phase transformation electrode materials.

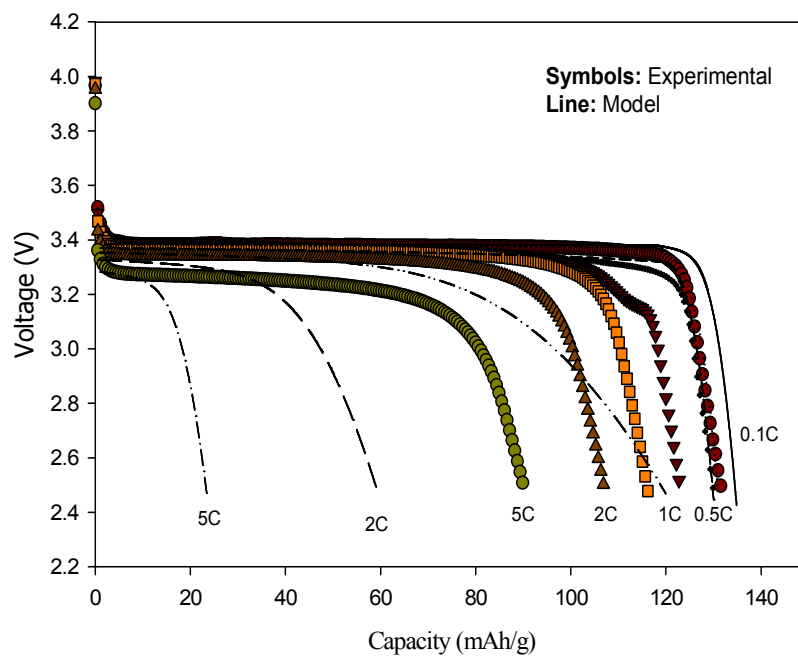


Figure 4.3: Discharge curves of sample A LiFePO₄ sample at different current densities: Experimental (symbols) and SCM Predictions (lines)

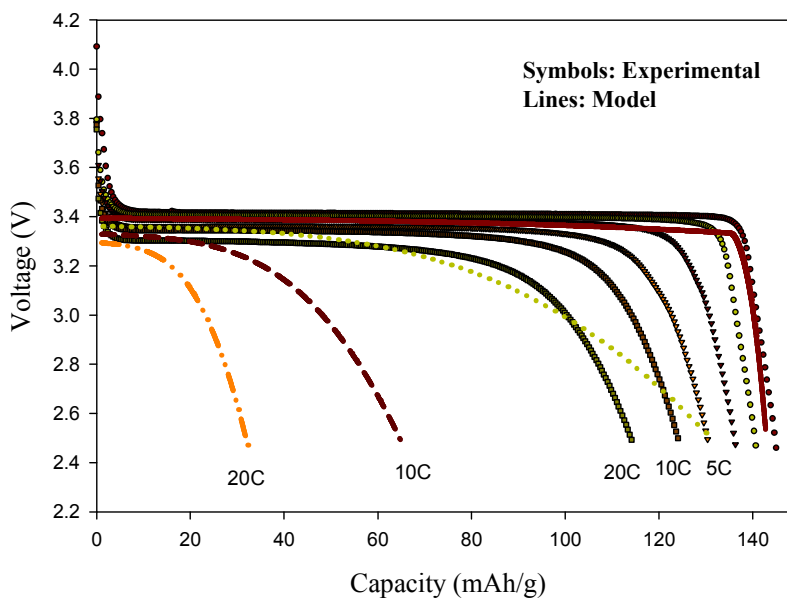


Figure 4.4: Discharge curves of sample B LiFePO₄ sample at different current densities: Experimental (symbols) and SCM Predictions (lines)

4.1.5 Effect of Particle Shape on Discharge Curves

In shrinking core model, LiFePO₄ particles were assumed to be of spherical shape and the governing equations and boundary conditions were based on spherical geometry. But from the microstructural investigations carried out on LiFePO₄ during charge/discharge, Chen et al. [59] reported that LiFePO₄ particles are of plate-like shape and Li⁺ ion diffusion in LiFePO₄ takes place in one dimension. The difference between geometry used in shrinking core model and the shape of LiFePO₄ particles could be one of the contributing factors for the disagreement between the experimental and shrinking core model results. To find out the effect of geometry used in SCM on discharge behavior, discharge curves are obtained from SCM with spherical geometry and SCM with rectangular geometry. The parameters used in both models are same and are given as follows: $R_p = 8 \times 10^{-7}$ m, $D_\beta = 8 \times 10^{-16}$ m²/s, $\rho = 3.6$ g/cm³ & $C_\beta = 0.7718 \times 0.02044$ g/cm³. Figure 4.5 shows the comparison of discharge curves of LiFePO₄ at different currents obtained from SCM with rectangular and spherical geometries. From Figure 4.5, it is evident that discharge curve at 0.5 C rate current predicted from the two models match well. However, at high currents such as 1C rate and 2C rate, SCM with spherical geometry predicts lower discharge capacities compared to SCM with rectangular geometry. The lower discharge capacities predicted from SCM with spherical geometry can be explained by difficulty of diffusion phenomenon in a spherical particle compared to one-dimension diffusion in a plate like particle. From these results, it can be concluded that the discrepancy between the experimental and SCM results is also due to the spherical geometry used in SCM.

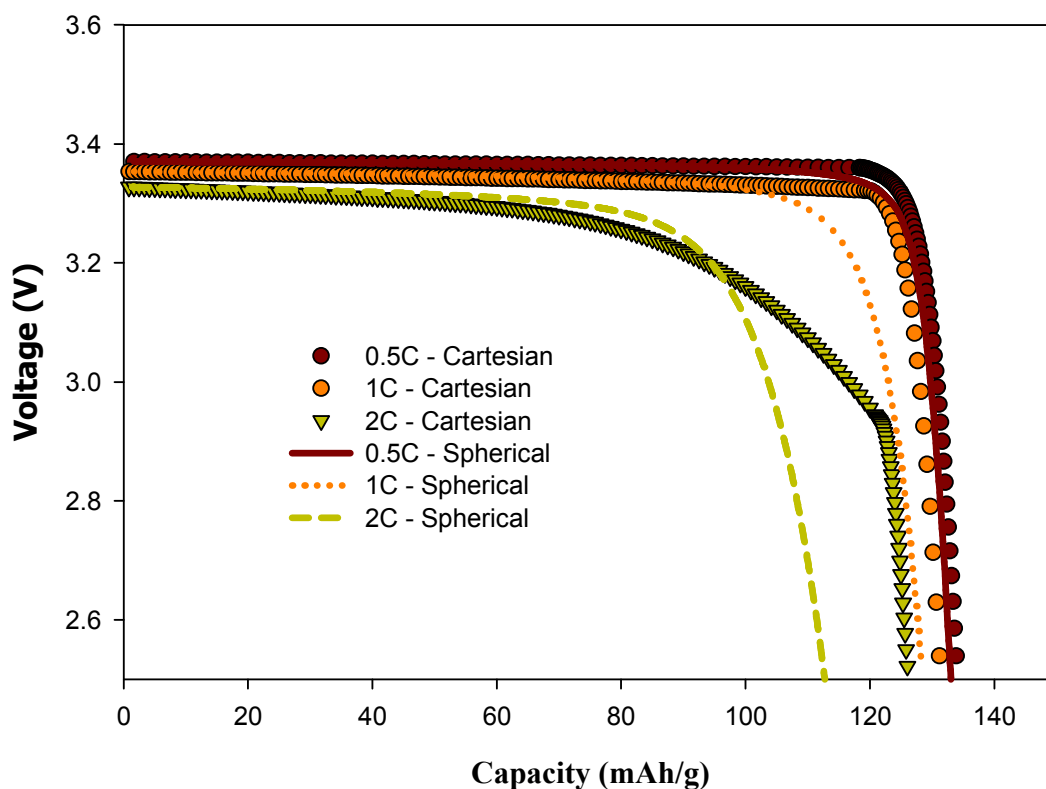


Figure 4.5: Discharge curves of LiFePO_4 predicted from SCM with rectangular geometry and SCM with spherical geometry

4.2 Assessment by Potential-step Chronoamperometry (PSCA) Measurement

As mentioned earlier, PSCA measurement is a commonly used experiment in the field of electrochemistry. In this measurement, the potential is changed instantaneously from initial value to final value and the current (i) versus time is measured. From the current vs. time data, the controlling mechanism for the charge/discharge process can be determined. To determine the controlling mechanism, the current–transient response of $\text{LiFe}_{0.9}\text{Mg}_{0.1}\text{PO}_4$ is measured using potential-step chronoamperometry (PSCA). Figure

4.6 shows the current–transient curves for $\text{LiFe}_{0.9}\text{Mg}_{0.1}\text{PO}_4$ obtained by potential-step from open-circuit potential (OCP) 3.6 to 3.1V, and from OCP 3.1 to 3.48V, in which the phase transformation between $\text{LiFe}_{0.9}\text{Mg}_{0.1}\text{PO}_4$ and $\text{Li}_{0.1}\text{Fe}_{0.9}\text{Mg}_{0.1}\text{PO}_4$ takes place. The current decayed rapidly in both cases, although the initial current and decay rate are different for the two potential jumps (Figure 4.6a). The slightly higher current for discharge (from 3.6 to 3.1 V) than that for charge (from 3.1 to 3.48 V) is probably due to large potential jump (0.5 V) in the discharge. A current hump is found for each potential jump after an initial rapid decay of the current. The presence of these current humps is the characteristic of nucleation in the phase transformation [60,61], which suggests that electrochemical nucleation and growth are involved in the electrode reaction at least during the initial stages [60]. To determine the controlling step, the linear scale in Figure 4.6a is converted into logarithm scale and replotted in Figure 4.6b. If diffusion controls the electrode reaction, a linear relationship between the logarithm of current and the logarithm of time with slope of 0.5 (i.e. Cottrell behavior or semi-infinite spherical diffusion) will be observed before an exponential decay of current with time [62]. However, the slope in Figure 4.6b is lower than 0.5 in the early stage, which suggests that the Li^+ diffusion in the $\text{LiFe}_{0.9}\text{Mg}_{0.1}\text{PO}_4$ is not the controlling step. To further ascertain that diffusion is not a controlling step, the position of the phase boundary between $\text{Li}_{0.1}\text{Fe}_{0.9}\text{Mg}_{0.1}\text{PO}_4$ and $\text{LiFe}_{0.9}\text{Mg}_{0.1}\text{PO}_4$ as a function of charge time is calculated based on SCM (Figure 4.7) proposed by Srinivasan and Newman [53] for LiFePO_4 electrode. Using the SCM [53,60], position of the phase boundary can be calculated from reacted fraction (α),

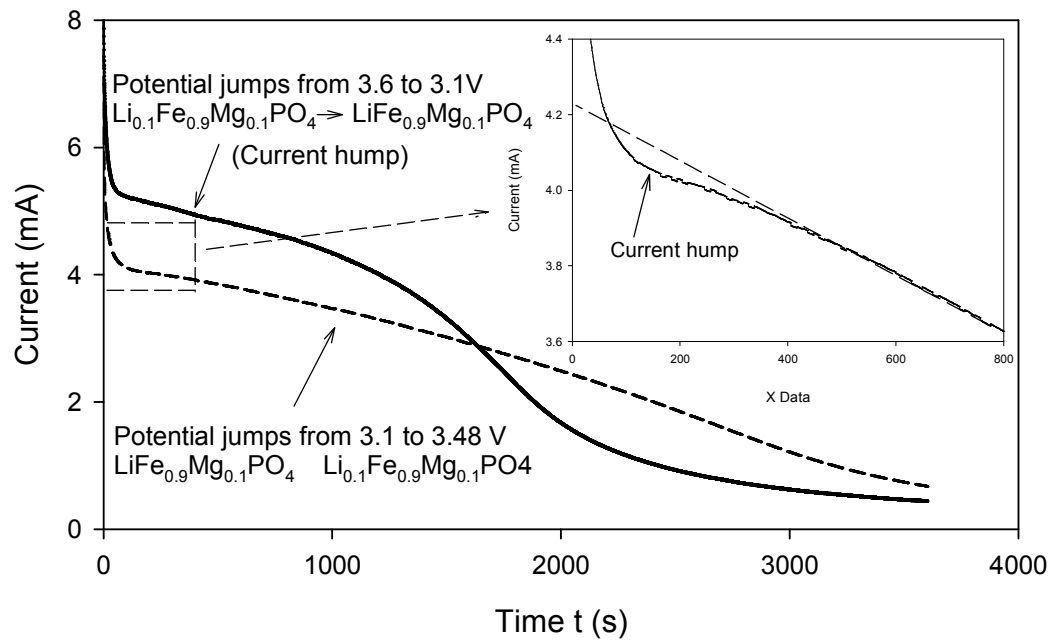
$$\xi = R_p [1 - (1 - \alpha)^{\frac{1}{3}}] \quad (4.4)$$

The reacted fraction Q_t/Q_∞ in Eq. 4.4 can be determined by the ratio of charge passed for a specific time (t) to the total charge, which is as follows:

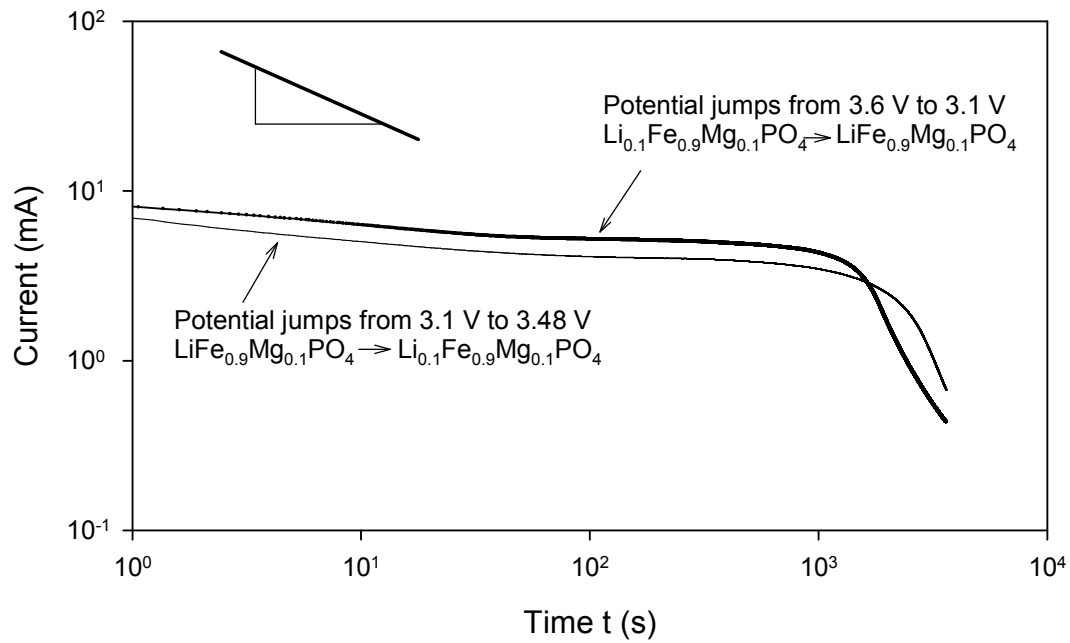
$$\alpha = \frac{\int_0^t i(t) dt}{\int_0^\infty i(t) dt} \quad (4.5)$$

where R_p is the radius of the particle and ζ is the position of phase boundary. From the $i(t)$ versus time plot obtained from PSCA measurements during charge process, reacted fraction values are computed using Eq. 4.5. Figure 4.8 shows the variation of experimentally determined α values with time t . From the plot, the total reaction time is found to be 57 min. From the variation of experimentally determined values of α with time (Figure 4.8), the position of phase boundary for different time values is obtained using Eq. 4.4, which is shown in Figure 4.9. In Figure 4.9, ζ versus t plot is found to be a straight line with a slope of 0.0154. If the reaction process is controlled by diffusion, ζ versus $t^{1/2}$ plot should be a straight line according to the analysis by Funabiki et al. [60] and Jost [63] for a diffusion-limited phase transformation with a moving phase boundary. Figure 4.9 shows a linear relationship with $t^{1.2}$ not $t^{1/2}$, which further confirms that the reaction process is not controlled by diffusion. If phase transformation (nucleation and growth) is the limiting step during the charge and discharge, fraction transformation or reacted fraction should follow the Johnson–Mehl–Avrami equation [64].

$$\alpha = 1 - \exp(-kt^m) \quad (4.6)$$



(a)



(b)

Figure 4.6: The absolute value of anodic and cathodic currents of $\text{LiFe}_{0.9}\text{Mg}_{0.1}\text{PO}_4$ (a) in a linear scale and (b) in a logarithm scale obtained by potential-step experiment. The negative charge current induced by potential jumping from 3.1 V to 3.48 V was converted to positive value to compare with discharge jumping current.

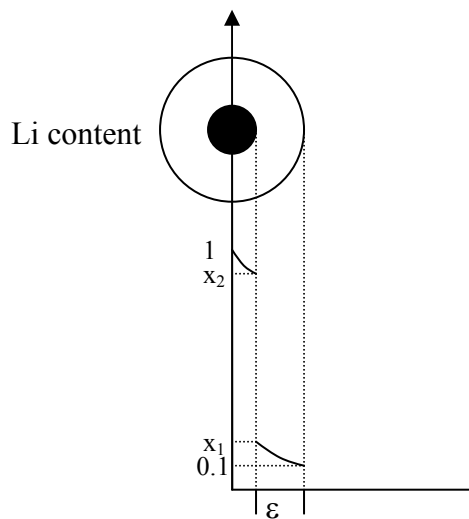
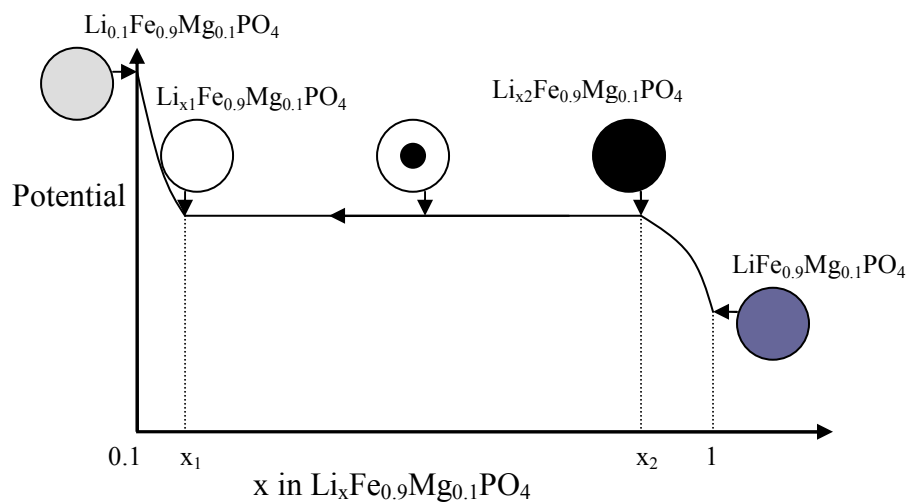


Figure 4.7: Illustration of the shrinking-core model with the juxtaposition of the two phases during the Li extraction (charge) from $\text{LiFe}_{0.9}\text{Mg}_{0.1}\text{PO}_4$ and the movement of the phase boundary.

The k ($k^{1/m}$ unit: s^{-1}) value in Eq. 4.6 depends on number of factors such as geometry of the growing nuclei, initial number of nuclei per unit volume, growth velocity of the nuclei, and dimensionality of growth [65]. Similarly the factor m depends on nucleation rate per unit volume and dimensionality of growth [65]. For convenience Eq. 4.6 can be written as

$$[-\ln(1 - \alpha)]^{1/m} = k^{1/m}t \quad (4.7)$$

The experimental and fitted values of $-\ln(1-\alpha)$ and time are shown in Figure 4.10, which resulted in values of 3.9×10^{-3} , 1.6 for k and m , respectively (fitting is achieved with a R^2 value of 0.99233, which shows the accuracy of the fit). The m value obtained from the fit being greater than 1 also shows that the reaction rate is controlled by nucleation and growth mechanism, i.e. phase transformation [65].

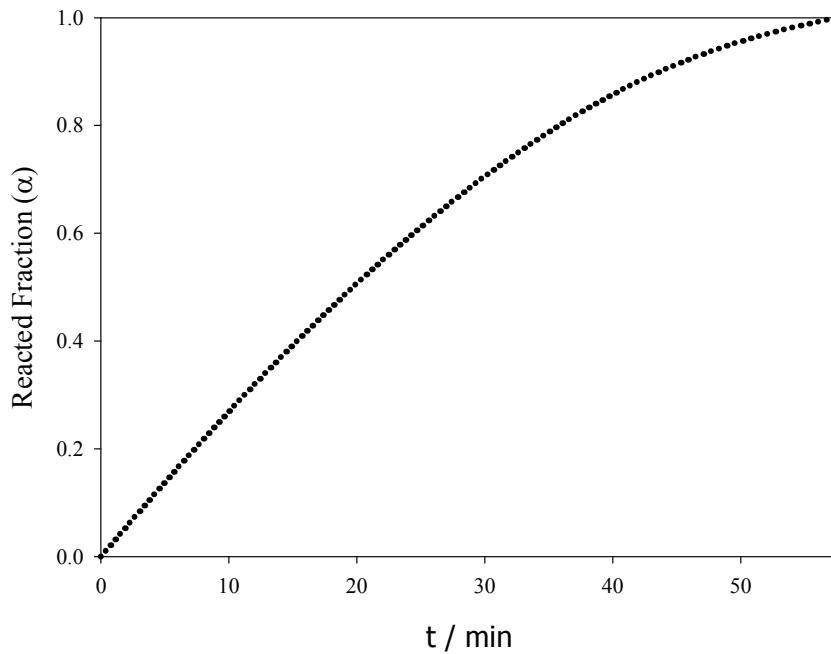


Figure 4.8: Time dependence of reacted fraction $\alpha(t)$ of fully discharged $\text{LiFe}_{0.9}\text{Mg}_{0.1}\text{PO}_4$ electrode for the charge process

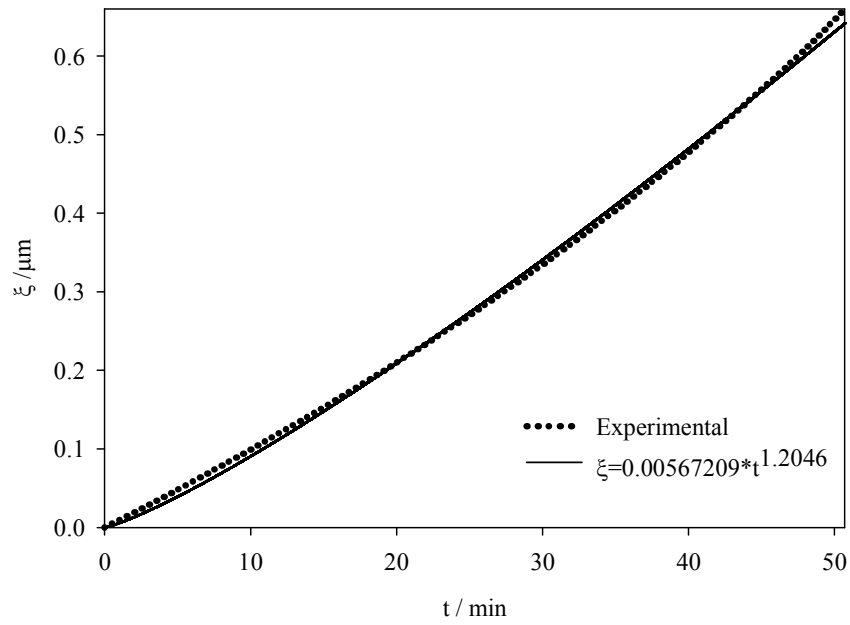


Figure 4.9: Relationship between the position of phase boundary ξ and time for fully discharged $\text{LiFe}_{0.9}\text{Mg}_{0.1}\text{PO}_4$ electrode during charge process.

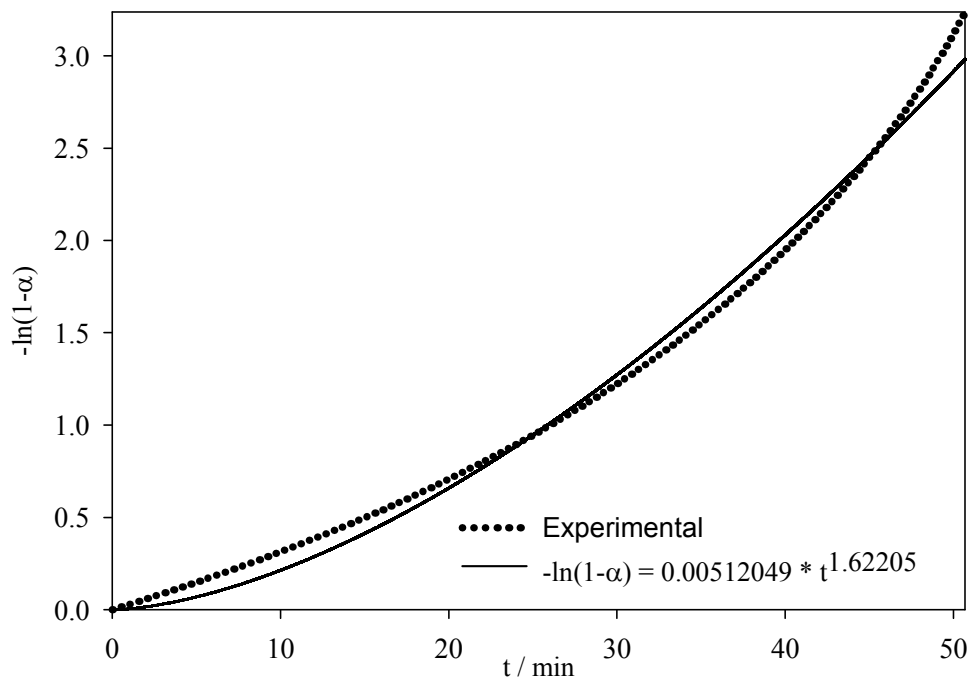


Figure 4.10: $-\ln(1-\alpha)$ plotted against time for charge process of $\text{LiFe}_{0.9}\text{Mg}_{0.1}\text{PO}_4$ electrode

4.3 Limitations of Shrinking Core Model

From the PSCA measurements, mathematical modeling and the detailed literature review that has been done on LiFePO_4 , the following inferences can be drawn:

- i. The discharge kinetics of LiFePO_4 is not controlled by only diffusion process. It may be possible that either the rate of phase transformation or both the diffusion and the rate of phase transformation are the controlling steps.
- ii. LiFePO_4 undergoes 6% volume change during the charge/discharge process and it cannot be neglected.
- iii. LiFePO_4 particles are of plate-like shape and Li^+ ion diffusion takes place in one dimension [59].

From these inferences, it is evident that the assumptions used in the development of the shrinking core model are not completely valid. Due to these assumptions, the diffusion controlled shrinking core model is limited in predicting the discharge behavior of LiFePO_4 samples.

CHAPTER 5

DEVELOPMENT OF MATHEMATICAL MODEL

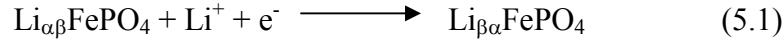
5.1 Modified SCM-1: Model Involving Only Transport in β Phase

From Chapter 4, it is evident that the discrepancy between the experimental results and the results from SCM is due to the assumption that the charge/discharge process is controlled by diffusion. Hence, to accurately predict the discharge behavior of LiFePO_4 samples, the shrinking core model should be modified based on the theory of mixed mode phase transformations. Prior to modifying the SCM, it is very important to understand the charge/discharge mechanism of LiFePO_4 .

5.1.1 Description of Discharge Process of LiFePO_4

The discharge process of the LiFePO_4 electrode can be described based on 1D diffusion of Li-ion in $\text{FePO}_4/\text{LiFePO}_4$ lattice [59]. Figure 5.1 shows the typical discharge curve of LiFePO_4 and the lithium ion concentration distribution in LiFePO_4 during discharge. Initially the fully charged LiFePO_4 particle consists of FePO_4 phase. At the beginning of the discharge, Li^+ ion inserts into surfaces of the FePO_4 particle along x-direction and diffuses into interior of the particle (Figure 5.1a). This process results in the formation of a solid solution Li_yFePO_4 (α phase, Figure 5.1a) and this process continues until the Li^+ ion content “y” in Li_yFePO_4 reaches the solid solubility limit ($C_{\alpha\beta}$). This process corresponds to the initial potential sloping line in the discharge curve (a- b

section in Figure 5.1a). Upon further discharge, the following reaction takes place at the surface, resulting in conversion of α phase present at the surface to β phase ($\text{Li}_{\beta\alpha}\text{FePO}_4$).



At this point of discharge, α and β phases co-exist in the particle and these two phases are separated by two interfaces. On further discharge, Li^+ ion diffuses through β phase and reacts with α phase at the interface, resulting in conversion of more α phase to β phase, i.e. leading to movement of both the interfaces towards the center of the particle (b-c section in Figure 5.1a). This procedure continues until both interfaces reach the center of particle, i.e. when the particle is fully formed of β phase (c point in Figure 5.1a). Further discharge leads to further diffusion of Li^+ ion into the particle and conversion of $\text{Li}_{\beta\alpha}\text{FePO}_4$ (β phase) to LiFePO_4 particle (c-d section in Figure 5.1a).

Figure 5.1b shows the Li^+ ion concentration in a planar geometry for LiFePO_4 during the discharge process. Similar to the SCM [53], the lithium ion content in α phase at the interface is considered to be equal to the equilibrium concentration $C_{\alpha\beta}$. The reason behind this assumption is because the Li concentration in α phase reaches equilibrium during the resting time before discharge and, also the lithium solubility (or discharge capacity) in α phase is very small. However, when the interface mobility is lower, the concentration of β phase (C_β) at the interface is higher than the equilibrium concentration of β phase ($C_{\beta\alpha}$) [64]. This concentration departure is required to drive the interface movement because of the non-equilibrium conditions prevailing at the interface. The lithium required for the $\alpha \rightarrow \beta$ phase transformation is provided by the chemical diffusion of lithium ion from surface to interface, due to the concentration gradient present in the β phase. The surface concentration of β phase ($C_{\beta\text{S}}$) during discharge is

always higher than the interface concentration (C_β) (Figure 5.1b) and becomes equal to the maximum lithium concentration in FePO_4 lattice (C_i) at the end of discharge. If the rate of interfacial reaction (interface mobility) is fast and the phase transformation is governed by the chemical diffusion of lithium in the β phase, the interface concentration (C_β) will be near to the equilibrium value $C_{\beta\alpha}$. This is known as the diffusion-controlled growth and it was modeled by Srinivasan et al. [53] and Zhang et al. [66] by using the SCM in spherical geometry. However, if the rate of the interfacial reaction is slow, the growth rate will be governed by the interface kinetics, i.e. the phase growth is interface-controlled [67]. In most of the phase transformations, both the interface reaction and diffusion process affect the phase growth, which can be described by the mixed control or the mixed mode phase transformations [68]. The concept of mixed mode phase transformation has been applied previously in the modeling of dissolution of spherical precipitates [69] and proeutectoid growth in Fe-C alloys [68,70,71]. It will be used for describing the discharge process in the present work.

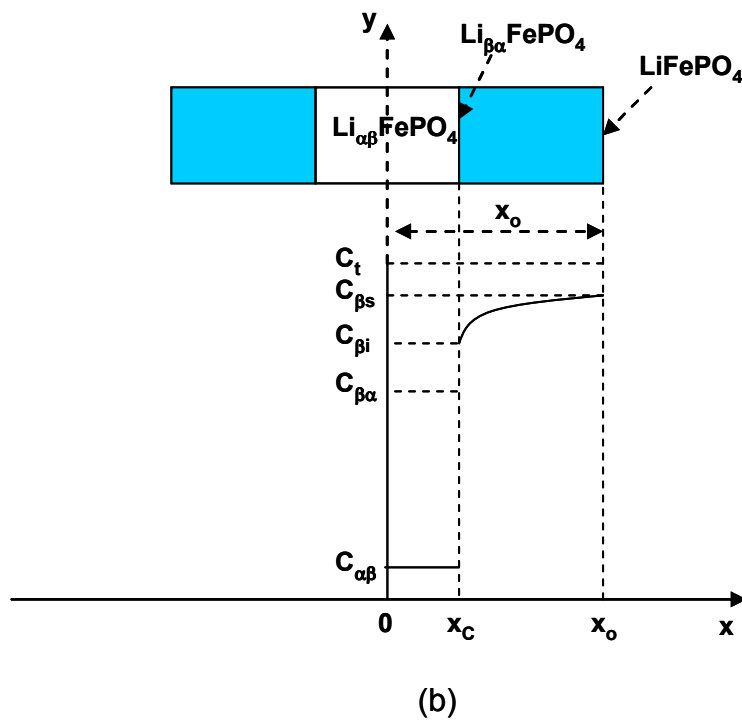
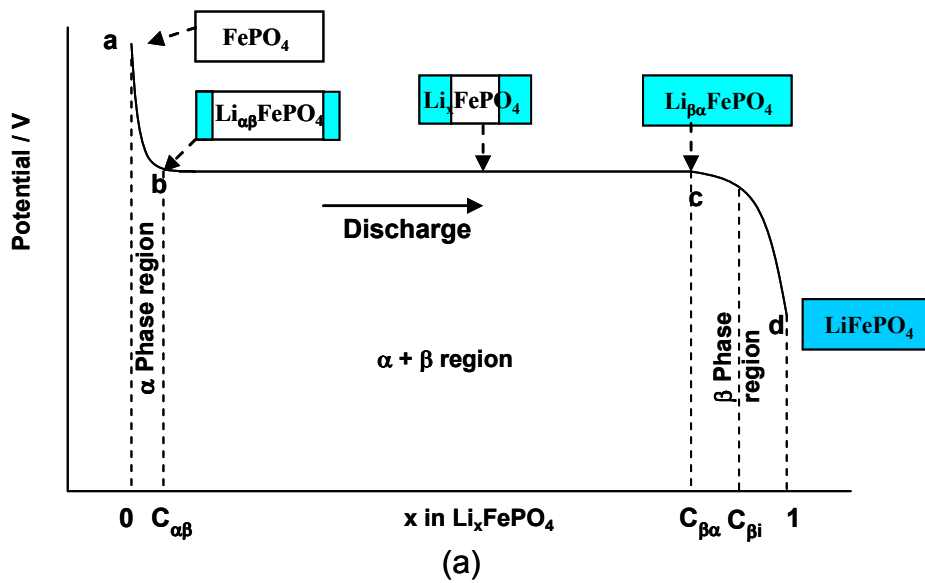


Figure 5.1: Schematic showing (a) phase transformation and (b) Li^+ ion concentration distribution during the discharge of a LiFePO_4 particle (Li insertion into FePO_4).

5.1.2 Governing Equations and Boundary Conditions

The lithium diffusion process in LiFePO₄ during the discharge process can be modeled by modifying the transport equations proposed by Srinivasan et al. [53] in rectangular coordinates instead of spherical coordinates and, by using interfacial concentration $C_{\beta i}$ to replace the equilibrium concentration $C_{\beta\alpha}$. For simplifying the model development, the initial single-phase region (a-b section, Figure 5.1a) and α phase in phase change region (b-c section, Figure 5.1a) are neglected.

Governing equations, the initial condition, and the boundary conditions for this model can be written as follows:

For Region II:

$$\frac{\partial C_{\beta}}{\partial t} = D_{\beta} \left(\frac{\partial^2 C_{\beta}}{\partial x^2} \right) \quad (5.2)$$

$$C_{\beta} = 0 \quad \text{at } t = 0 \quad (5.3)$$

$$D_{\beta} \left(\frac{\partial C_{\beta}}{\partial x} \right) = \frac{i}{F} \quad \text{at surface } x = x_0 \quad (5.4)$$

$$C_{\beta} = C_{\beta i} \quad \text{at interface } x = x_c(t) \quad (5.5)$$

The unknown interface position can be evaluated by doing a mass balance of Li⁺ ions at the interface, which is given by the following equation:

$$\frac{dx_c(t)}{dt} = \frac{D_{\beta}}{(-C_{\beta i})} \left(\frac{\partial C_{\beta}}{\partial x} \right)_{x=x_c(t)} \quad (5.6)$$

When the interface reaches the center of the particle (the dimensionless interface position reaches a value of 0.001), i.e. when the particle is full of β phase, the particle enters into the final solid solution region (c-d section, Figure 5.1a). Under these conditions the differential model given by Eq. (5.2-5.6) reduces to:

For Region III:

$$\frac{\partial C_{\beta}}{\partial t} = D_{\beta} \left(\frac{\partial^2 C_{\beta}}{\partial x^2} \right) \quad (5.7)$$

$$D_{\beta} \left(\frac{\partial C_{\beta}}{\partial x} \right) = \frac{i}{F}, \text{ at surface } (x = x_0) \quad (5.8)$$

$$D_{\beta} \left(\frac{\partial C_{\beta}}{\partial x} \right) = 0, \text{ at particle center } (x = 0) \quad (5.9)$$

The initial condition for Eq. 5.7 is the lithium ion concentration profile inside the β phase at the end of the phase change region (region II). In the system of equations, C_{β} corresponds to the concentration of Lithium inside Li_xFePO_4 particle; $C_{\beta i}$ corresponds to the actual interface concentration of Li rich phase; D_{β} corresponds to lithium chemical diffusion coefficient (electron and ionic) in Li rich (β) phase, that is assumed to be concentration independent; $x_c(t)$ corresponds to interface position and i corresponds to reaction current applied on the particle surface. To solve the system of equations, actual concentration of Li rich phase at the interface ($C_{\beta i}$) needs to be determined. This can be determined from the theory of mixed mode phase transformation.

5.1.3 Theory of Mixed Mode Phase Transformations

In mixed mode phase transformation, it is assumed that the charge/discharge process is controlled by both diffusion and rate of phase transformation. It also implies that both diffusion and phase transformation are occurring at same rate. Also, in a mixed mode phase transformation, a steady state exists across the interface leading to the balance of flux of Li^+ ion across the interface and towards the interface [64].

The flux of Li^+ ions across the interface [64] can be given by

$$j_{\text{Li}}^i = -M \times \Delta G_{\alpha-\beta}^i (C_{\beta i} - C_{\alpha i}) \quad (5.10)$$

where M is the interface mobility, which depends on the degree of coherence of interface, and the build-up of stress and deformations. $C_{\beta i}$ is the actual concentration of Lithium rich (β) phase, which is higher than the local equilibrium concentration ($C_{\beta\alpha}$). $C_{\alpha i}$ is the actual concentration of Lithium deficient (α) phase, which is higher than the local equilibrium concentration ($C_{\alpha\beta}$). $\Delta G_{\alpha-\beta}^i$ is the driving force for the occurrence of transformation from α phase to β phase. The driving force [26,27] can be expressed as follows:

$$\Delta G_{\alpha-\beta}^i = \Delta G_{\alpha-\beta}^{\text{Chem}} - \Delta G_{\alpha-\beta}^{\text{Elastic}} - \Delta G_{\alpha-\beta}^{\text{Plastic}} + \Delta G_{\alpha-\beta}^{\text{Surface}} \quad (5.11)$$

where $\Delta G_{\alpha-\beta}^{\text{Chem}}$ is the chemical free energy difference resulting from the sum of deviations

with respect to equilibrium concentration $(\frac{C_{\beta i} - C_{\beta\alpha}}{C_{\beta\alpha}}, \frac{C_{\alpha i} - C_{\alpha\beta}}{C_{\alpha\beta}})$. $\Delta G_{\alpha-\beta}^{\text{Surface}}$ is the free

energy resulting from free surfaces and it can be neglected when compared with other

terms. $\Delta G_{\alpha-\beta}^{\text{Elastic}}$ and $\Delta G_{\alpha-\beta}^{\text{Plastic}}$ are the free energies resulting from elastic and plastic

deformation. In Eq. 5.11, $\Delta G_{\alpha-\beta}^{Chem}$ supports the phase transformation, and $\Delta G_{\alpha-\beta}^{Surface}$, $\Delta G_{\alpha-\beta}^{Elastic}$, and $\Delta G_{\alpha-\beta}^{Plastic}$ act against the transformation. As a result, for the occurrence of the phase transformation, $\Delta G_{\alpha-\beta}^{Chem}$ should be always higher than the sum of the other three terms in Eq. 5.11.

In general, the phase transformation in LiFePO_4 is accompanied by 6.8% volume change between α and β the phases. As a result of the volume change, elastic and plastic deformations take place. Due to these deformations, some useful energy is spent in the formation of dislocations and some useful energy is dissipated to surrounding in the form of heat. The energy lost due to the deformations is referred to as accommodation energy. Loss of this useful energy can be seen as hysteresis (voltage difference between the charge and discharge) in the charge/discharge curves. This hysteresis value increases with the increase in volume change. Also, depending on the lattice mismatch/volume change, the boundary between the lithiated and the delithiated phases can be considered as coherent, semi-coherent, or incoherent interface [26,64]. For the cases of coherent, semi-coherent, and incoherent interfaces, the energy barrier for phase transformation is affected by elastic and plastic accommodation energies. For the case of coherent interface, the elastic accommodation energy plays a major role in the total accommodation energy. Recently, Chiang et al. [24,25,26] reported that the energy barrier for phase transformation in nano-scale LiFePO_4 (coherent interface) is mainly induced by the elastic accommodation energy ($\Delta G_{\alpha-\beta}^{Elastic}$). In their work, the calculated elastic accommodation energy increased with state of discharge and then decreased after reaching the peak at 50% state of discharge. This behavior is similar to the elastic

accommodation energy change during hydrogen insertion into some metals [72]. However, for the semi-coherent, and incoherent interfaces, the plastic accommodation energy must be considered, since it has a more important role in the phase transformation than elastic energy [72].

Effect of elastic and plastic accommodation energies on the hysteresis in systems undergoing phase transformation is evident from the study of metal-hydride systems [73-76]. The sum of the elastic and plastic accommodation energies can be determined from the following equations [77]:

$$\Delta G_{\alpha-\beta}^{Elastic} + \Delta G_{\alpha-\beta}^{Plastic} = W_{\alpha-\beta} \times V_i \quad (5.12)$$

where $W_{\alpha-\beta}$ is the total accommodation energy resulting from elastic and plastic deformation and V_i is the molar volume of α phase present in the lattice. The total accommodation energy per unit volume of the β phase formed can be given by

$$W_{\alpha-\beta} = \frac{(P^{E+P})^2 (1-\gamma)}{2\gamma K} + \frac{\sigma_y^2}{A_p \mu} \left[\frac{1}{6} + \left(\frac{r_p}{a_p} \right)^3 \ln \left(\frac{r_p}{a_p} \right) \right] \quad (5.13)$$

where σ_y is the yield stress of the α phase, r_p is the plastic zone radius, a_p is β phase radius, μ is the shear modulus of the α phase, and A_p is given by

$$A_p = \frac{(1+\nu)}{3(1-\nu)} \quad (5.14)$$

where ν is the Poisson's ratio of the α phase.

The value of (r_p/a_p) can be evaluated from the following relationship

$$\left(\frac{r_p}{a_p} \right) = \exp \left(\frac{P^{E+P}}{2\sigma_y} - \frac{1}{3} \right) \quad (5.15)$$

where P^{E+P} , the internal hydrostatic pressure in the β phase, is given by

$$P^{E+P} = 3K\gamma\varepsilon_p(1 - B^{E+P}) \quad (5.16)$$

The value of B^{E+P} can be obtained from

$$\frac{6A_p\mu\varepsilon_p}{\sigma_y}(\gamma + B^{E+P} - \gamma B^{E+P}) = \exp\left[\frac{9K\gamma\varepsilon_p}{2\sigma_y}(1 - B^{E+P}) - 1\right] \quad (5.17)$$

In the above equations, K is the bulk modulus of the α phase, γ is the ratio of K_β/K_α , and ε_p is the radial stress-free misfit strain of the β phase. Hence, the total accommodation energy expended for the charge/discharge cycle is the sum of accommodation energies lost during the forward (α to β) and reverse (β to α) transformation, given as follows:

$$\Delta G_{Loss} = W_{\alpha-\beta} \times V_\alpha + W_{\beta-\alpha} \times V_\beta \quad (5.18)$$

The details and derivations of these equations can be found in [78, 79]. From these equations, it is evident that the elastic and plastic accommodation energy depend on material properties such as yield stress, bulk modulus, shear modulus, and Poisson's ratio. To the author's knowledge, there are no data available on accommodation energy or above-mentioned material properties for LiFePO_4 in the literature. Also, it is difficult to obtain these data for LiFePO_4 through experiments.

Due to the difficulty in obtaining experimental data and due to the striking similarity of phase transformation in hydrogen insertion into metal and lithium insertion into FePO_4 [72], data on the accommodation energy for hydrogen insertion into Nb [72] and for temperature induced austenite (γ)-ferrite (α) transformation in Fe-Mn alloys [80] are used to simulate the accommodation energy during Li insertion into FePO_4 . The variation of the accommodation energy during the phase transformation in metal hydride electrode is shown in Figure 5.2.

From Figure 5.2, depending on the type of interface formed, the variation in accommodation energy during the phase transformation process is proposed to be described by the following expressions.

$$\Delta G_{\alpha-\beta}^{Elastic} + \Delta G_{\alpha-\beta}^{Plastic} = A \times P \times \Delta G_{\alpha-\beta}^{Chem} \times f(x_C(t)) \quad (5.19)$$

where

$$f(x_C(t)) = \sin(\pi x_C(t)) \quad \text{for coherent interface} \quad (5.20a)$$

$$f(x_C(t)) = 1 - x_C(t)^n \quad \text{for semi-coherent and incoherent interface} \quad (5.20b)$$

The parameter “P” in Eq. 5.19 is a proportionality factor that defines the peak value of accommodation energy. For example, if P is equal to one, the accommodation energy will have a peak value equal to the chemical driving force. Since the magnitude of accommodation energy changes with the volume change [24], the parameter “A” in Eq. 5.19 is used as the accommodation energy factor to reflect the volume change. The value of “A” will decrease with the decrease in volume change of phase transformation. From Eq. 5.20a, for the case of a coherent interface, during the initial and final stages of the transformation ($x_C(t) = 1, 0$), the accommodation energy is found to be zero and the accommodation energy is at its maximum at 50% of the transformation. This behavior is similar to the accommodation energy data reported by Chiang et al. [24].

From Eq. 5.20b, for the case of a semi-coherent and incoherent interface, during the initial stage of the transformation ($x_C(t) = 1$), the accommodation energy is found to be zero, and at the end of the transformation, the accommodation energy is at its maximum, which is similar to the variation of accommodation energy for hydrogen insertion into Nb [72]. The parameter “n” in Eq. 5.20b determines the type of variation in accommodation

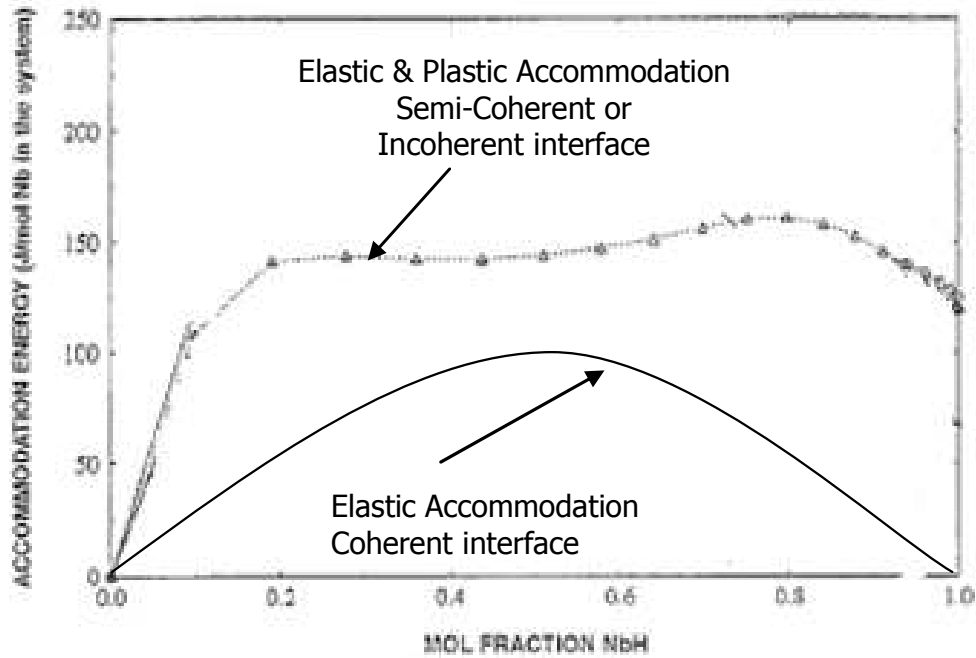


Figure 5.2: Variation of accommodation energy during hydride precipitation through the surface to center path for different aspect ratios of the precipitate (figure taken from ref. 72)

energy during the progress of transformation. For example, the value of n being close to 1 corresponds to the case of linear increase in the accommodation energy. When the value of n increases further, it corresponds to the case where the accommodation energy increases quickly during the initial stages of the transformation process and then it reaches the steady state.

The chemical energy difference in Eq. 5.20 can be expressed as follows [64]

$$\Delta G_{\alpha-\beta}^{Chem} = RT \left[\frac{(C_{\beta i} - C_{\beta \alpha})}{C_{\beta \alpha}} + \frac{(C_{\alpha i} - C_{\alpha \beta})}{C_{\alpha \beta}} \right] \quad (5.21)$$

Rearranging Eq. 5.11 by using Eq. 5.19 and Eq. 5.21, one obtains

$$\Delta G_{\alpha-\beta}^i = RT \left[\frac{C_{\beta i}}{C_{\beta\alpha}} + \frac{C_{\alpha i}}{C_{\alpha\beta}} - 2 \right] (1 - A \times P \times f(x_C(t))) \quad (5.22)$$

Similar to the case of Eq. 5.10, the diffusion flux of Li⁺ ions/electrons towards the interface can be written as follows

$$j_{Li}^\beta = D_\alpha \left(\frac{\partial C_\alpha}{\partial x} \right)_{x=x_C(t)} - D_\beta \left(\frac{\partial C_\beta}{\partial x} \right)_{x=x_C(t)} \quad (5.23)$$

From Eqs. 5.10, 5.22, and 5.23, C_{βi} can be calculated and it is given by the following expression

$$\left(\frac{C_{\beta i}}{C_{\beta\alpha}} + \frac{C_{\alpha i}}{C_{\alpha\beta}} - 2 \right) \times (C_{\beta i} - C_{\alpha i}) = \frac{D_\beta \left(\frac{\partial C_\beta}{\partial x} \right)_{x=x_C(t)} - D_\alpha \left(\frac{\partial C_\alpha}{\partial x} \right)_{x=x_C(t)}}{MRT(1 - A \times P \times f(x_C(t)))} \quad (5.24)$$

Since the actual concentration of Li deficient phase at the interface (C_{αi}) is assumed to be equivalent to equilibrium concentration of Li deficient phase at the interface phase (C_{αβ}) and α phase in region II is neglected, Eq. 5.24 reduces to

$$\left(\frac{C_{\beta i}}{C_{\beta\alpha}} - 1 \right) \times (C_{\beta i}) = \frac{D_\beta \left(\frac{\partial C_\beta}{\partial x} \right)_{x=x_C(t)}}{MRT(1 - A \times P \times f(x_C(t)))} \quad (5.25)$$

5.1.4 Solution Methodology

Eqs. 5.2-5.9 and 5.25 are converted to dimensionless form using the following variables.

$$\theta_{\beta} = \frac{C_{\beta}}{C_t} \quad \theta_{\beta\alpha} = \frac{C_{\beta\alpha}}{C_t} \quad \theta_{\beta i} = \frac{C_{\beta i}}{C_t} \quad \theta_{\beta S} = \frac{C_{\beta S}}{C_t} \quad X = \frac{x}{x_0} \quad X_c = \frac{x_c}{x_0} \quad \tau = \frac{tD_{\beta}}{x_0^2}$$

$$\delta = \frac{i\rho x_0^2}{D_{\beta} C_t F}$$

To simplify the analysis, a new dimensionless parameter Z_{β} is introduced and this parameter is related to diffusion coefficient, interface mobility, and diffusion length, as shown by the following equation.

$$Z_{\beta} = \frac{D_{\beta}}{MRTx_0}$$

The resulting systems of equations in dimensionless form are given as follows:

For Region II:

$$\frac{\partial \theta_{\beta}}{\partial \tau} = \frac{\partial^2 \theta_{\beta}}{\partial X^2} \quad (5.26)$$

$$\theta_{\beta} = 0 \quad \text{at} \quad \tau = 0 \quad (5.27)$$

$$\frac{\partial \theta_{\beta}}{\partial X} = \delta \quad \text{at surface} \quad X = 1 \quad (5.28)$$

$$\theta_{\beta} = \theta_{\beta i} \quad \text{at interface} \quad X = X_c(\tau) \quad (5.29)$$

$$\frac{dX_c(\tau)}{d\tau} = \frac{1}{(-\theta_{\beta i})} \left(\frac{\partial \theta_{\beta}}{\partial X} \right)_{X=X_c(\tau)} \quad (5.30)$$

Since both the samples used in this study have micro-meter particle size, they can be assumed to have a semi-coherent or incoherent interface. Based on this assumption, Eq. 5.25 can be converted into dimensionless form as follows:

$$\left(\frac{\theta_{\beta i}}{\theta_{\beta \alpha}} - 1 \right) \times (\theta_{\beta i}) = \frac{Z_{\beta} \left(\frac{\partial \theta_{\beta}}{\partial X} \right)_{X=X_C(\tau)}}{\left(1 - A \times P \times \left(1 - (X_C(\tau))^n \right) \right)} \quad (5.31)$$

For Region III:

$$\frac{\partial \theta_{\beta}}{\partial \tau} = \frac{\partial^2 \theta_{\beta}}{\partial X^2} \quad (5.32)$$

$$\frac{\partial \theta_{\beta}}{\partial X} = \delta, \text{ at surface } (X = 1) \quad (5.33)$$

$$\frac{\partial \theta_{\beta}}{\partial X} = 0, \text{ at particle center } (X = 0) \quad (5.34)$$

Eqs. 5.26-5.34 correspond to a nonlinear moving boundary value problem. Using the procedure mentioned in section 4.1.1, the system of equations is solved. In order to solve these equations, the values of the parameters $C_{\beta\alpha}$, C_t , x_0 , ρ , D_{β} , M , A , and n have to be known. The values of the parameters $C_{\beta\alpha}$, C_t , x_0 , and ρ are obtained from experiments (refer to section 3.4). Since there is no accurate method to determine the value of the parameters D_{β} , M , A , and n for phase transformation electrodes, guess values are given to these parameters. Once the values of all the parameters are known, dimensionless surface concentration ($\theta_{\beta s}$) as a function of time is determined for a particular current density. From $\theta_{\beta s}$, the equilibrium potential, the overpotential and the voltage during the

discharge are calculated. Figure 0.1 shows the results obtained from the modified shrinking core model for a set of parameter values ($A=1$, $D_{\beta} = 8 \times 10^{-14} \text{ m}^2/\text{s}$, $M = 1.23 \times 10^{-11} \text{ m.mol}/(\text{J.s})$, $i_0 = 0.1 \text{ A/g}$, $i = 1 \text{ C Current}$).

5.1.5 Parameter Sensitivity

Sensitivity analysis is a great tool to determine sensitivity of the model to the changes in the value of its parameters [81]. Sensitivity analysis boosts the confidence in the model by studying the uncertainties associated with the parameters in the model. Sensitivity analysis also allows us to determine the level of accuracy that is required for a parameter to make the model sufficiently useful and valid. If the tests reveal that the model is insensitive to smaller changes in the value of the parameter, then it may be possible to use an estimate rather than a value with greater precision. Sensitivity analysis can also indicate which parameter values are reasonable to use in the model. If the model behaves as expected from real world observations, it gives an indication that the values used for the parameters represent the real values. A quick and easy method to conduct the sensitivity analysis is to perform parameter sensitivity. In this method, different values are chosen for a particular parameter and with the change in the value of the parameter, the change in response of the model is observed [81].

The modified SCM-1 developed in section 5.1.2 involves parameters such as $C_{\beta\alpha}$, C_t , x_0 , ρ , D_{β} , M , and n . Since the parameters $C_{\beta\alpha}$, C_t , x_0 , and ρ are obtained from experiments, parameter sensitivity is observed for the parameters D_{β} , M , and n . To determine the parameter sensitivity, value of one parameter is changed in the model,

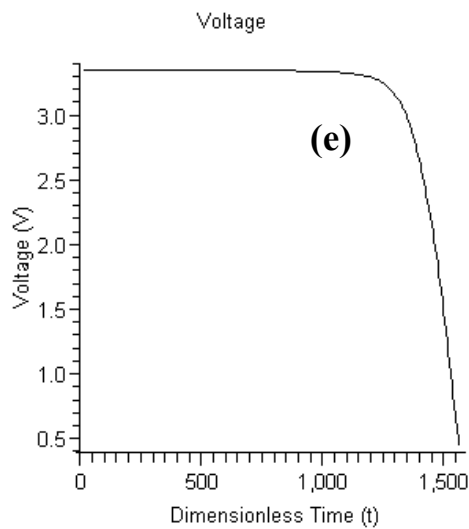
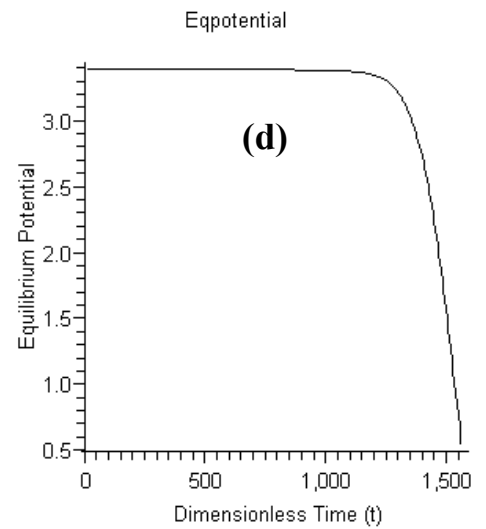
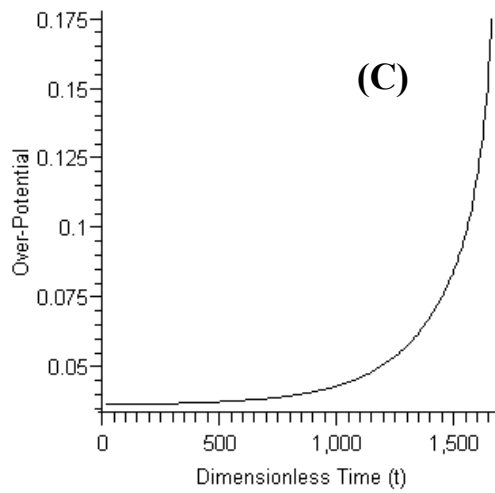
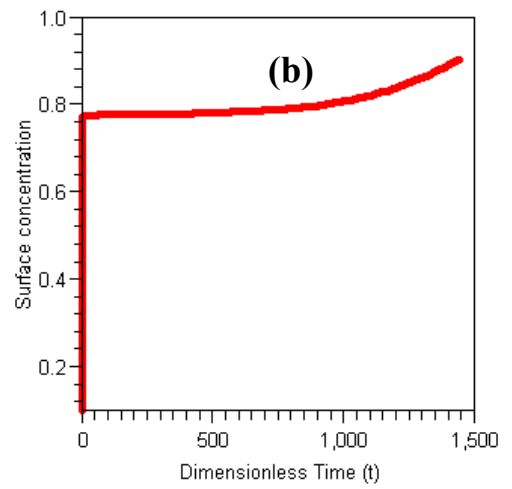
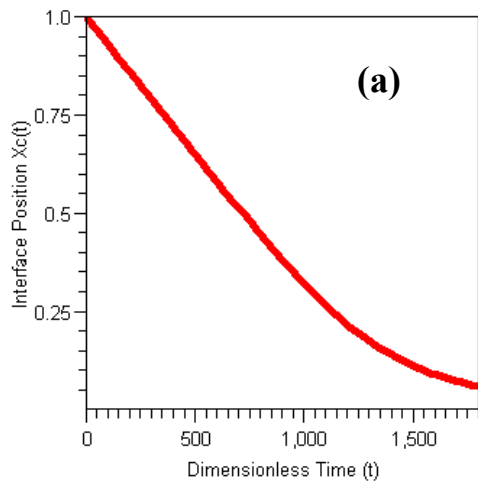


Figure 5.3:(a) Interface position of LiFePO_4 vs. dimensionless time
 (b) Dimensionless Surface concentration of LiFePO_4 vs. dimensionless time
 (c) Over-potential of LiFePO_4 vs. dimensionless time
 (d) Equilibrium potential of LiFePO_4 vs. dimensionless time
 (e) Voltage of LiFePO_4 vs. dimensionless time

while keeping the other parameters constant and the discharge curve at particular current density is determined. Here it should be noted, the discharge capacity determined from the above test should not exceed the theoretical capacity of the LiFePO_4 electrode determined from GITT experiment. Also the plots for concentration in the particle vs. time, interface position vs. time should not exhibit any abnormalities and should make sense from a practical point of view. For determining parameter sensitivity, in the modified SCM-1, the value of the parameter D_β is changed from $5 \times 10^{-17} \text{ m}^2/\text{s}$ to $10^{-13} \text{ m}^2/\text{s}$, where as the value of the parameter M is changed from 2×10^{-12} to $10^{-8} \text{ m.mol}/(\text{J.s})$ and the value of the parameter n is changed from 1 to 15. For each value of the parameter, discharge curve at 5C rate is determined. The values of the other parameters used in model are $A = 1$, $i_0 = 0.1 \text{ A/g}$, $x_0 = 0.8 \text{ }\mu\text{m}$, $\rho = 3.6 \text{ g/cm}^3$, $\theta_{\beta\alpha} = 0.771$, $C_t = 0.02044 \text{ mol/cm}^3$. The equilibrium potential equation (Eq. 4.1) for sample A is used for these simulations.

Figures 5.4, 5.5, and 5.7 show the effect of variation of the parameters D_β , M , and n in the modified SCM-1 on the discharge curve at 5C. The discharge curves presented in these figures do not exhibit any abnormalities and the discharge capacities calculated do not exceed the value of the theoretical capacity. Also the plots for concentration in the particle vs. time and interface position vs. time obtained do not show any abnormalities. From these results, it is evident that the range of values specified for the parameters are reasonable and they can be used in the modified SCM-1. From Figures 5.4 and 5.5, it can be understood that the discharge capacity decreases with the decrease in the diffusion coefficient in the β phase (D_β) and the interface mobility (M). With the decrease in D_β , a sudden drop in voltage is observed, which is due to the concentration polarization.

However, with the decrease in interface mobility, a decrease in the value of the voltage, at which the plateau is present, is observed. This is due to the phase transformation over potential and this phase transformation over potential increases with the decrease in interface mobility and increase in current density.

From Figure 5.7, a decrease in discharge capacity is observed with the increase in the value of the parameter n . The reason for the decrease in discharge capacity can be explained using Eqs. 5.19 and 5.20b. From Eqs. 5.19 and 5.20b, the accommodation energy variation during the progress of phase transformation can be calculated for materials with semi-coherent/incoherent interfaces, which is shown in Figure 5.6. From Figure 5.6, a linear increase in accommodation energy is observed for $n = 1$ and with the increase in the value of the parameter n , a sudden increase in accommodation energy is observed. Due to the sudden increase in accommodation during the initial stages of phase transformation, a larger amount of driving force is required in the initial stages for the phase transformation to proceed in the forward direction, resulting in slower phase transformation kinetics. From Figures 5.6 and 5.7, it can be inferred that the type of variation in accommodation energy during the phase transformation does also influence the discharge capacity.

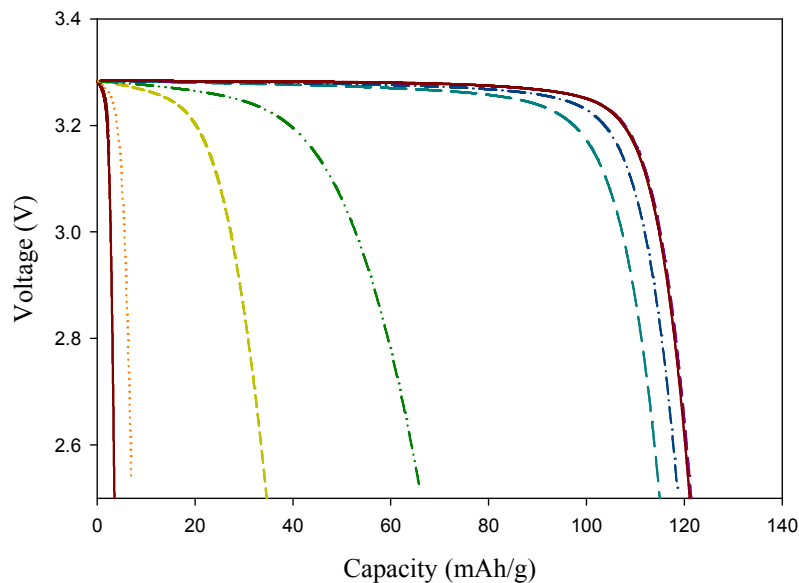


Figure 5.4: Effect of the parameter D_β on discharge curve at 5C obtained from modified SCM-1 with $M = 1 \times 10^{-10}$ m.mol/(J.s), $n = 2.2$ (From left: $D_\beta = 5 \times 10^{-17}$, 1×10^{-16} , 5×10^{-16} , 1×10^{-15} , 5×10^{-15} , 1×10^{-14} , 5×10^{-14} , and 1×10^{-13} m²/s)

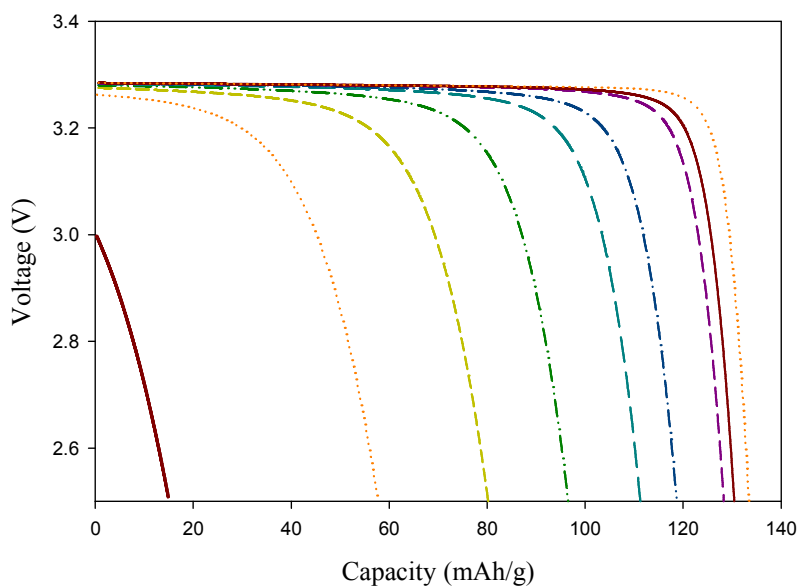


Figure 5.5: Effect of the parameter M on discharge curve at 5C obtained from modified SCM-1 with $D_\beta = 1 \times 10^{-14}$ m²/s, $n = 2.2$ (From left: $M = 2 \times 10^{-12}$, 5×10^{-12} , 1×10^{-11} , 2×10^{-11} , 5×10^{-11} , 1×10^{-10} , 5×10^{-10} , 1×10^{-19} , and 1×10^{-8} m.mol/(J.s))

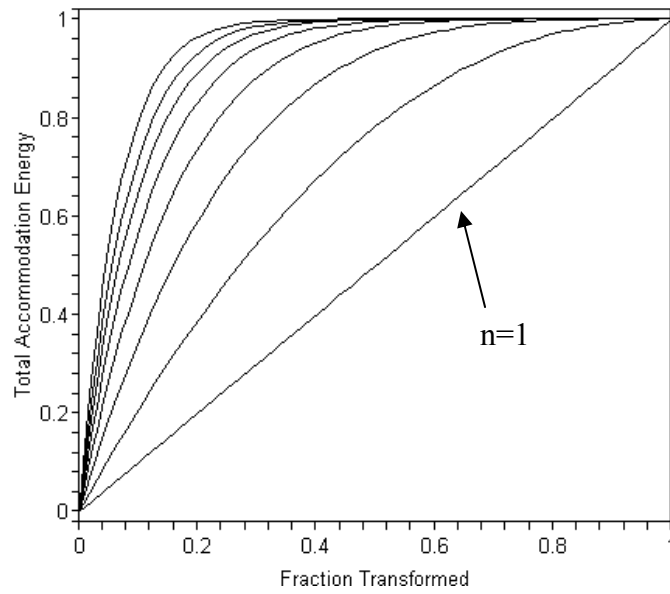


Figure 5.6: Effect of parameter n on accommodation energy variation during phase transformation ($n = 15, 12, 10, 8, 6, 4, 2.2,$ and 1)

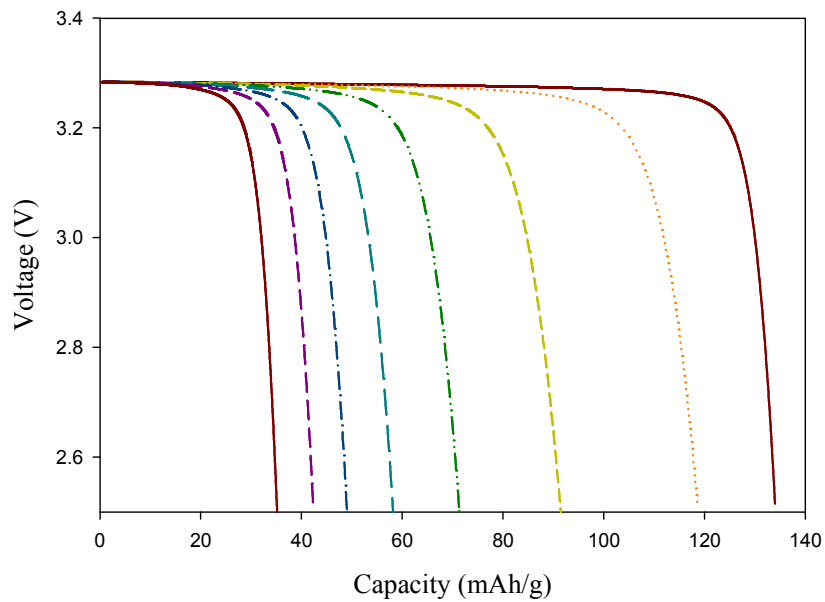


Figure 5.7: Effect of the parameter n on discharge curve at 5C obtained from modified SCM-1 with $D_{\beta} = 1 \times 10^{-14} \text{ m}^2/\text{s}$, $M = 1 \times 10^{-10} \text{ m.mol}/(\text{J.s})$ (From left: $n = 15, 12, 10, 8, 6, 4, 2.2,$ and 1)

5.1.6 Pseudosteady-State (PSS) Solution

Generally, a pseudosteady-state refers to a particular time, where the concentration profiles inside the particle are at steady state, for a particular value of shrinking core radius [52]. Pseudosteady-state can be obtained for the equations in region II in the modified SCM by assuming the steady state in Eq. 5.26, which is given as follows:

$$\frac{\partial^2 \theta_\beta}{\partial X^2} = 0 \quad (5.35)$$

The boundary conditions for Eq. 5.35 are

$$\frac{\partial \theta_\beta}{\partial X} = \delta \text{ at surface } X = 1 \quad (5.36)$$

Rearranging Eqs. 5.29 and 5.31

$$\theta_\beta = \frac{1}{2} \left[\theta_{\beta\alpha} + \sqrt{\theta_{\beta\alpha}^2 + \frac{4\theta_{\beta\alpha} Z_\beta \left(\frac{\partial \theta_\beta}{\partial X} \right)_{X=X_C(\tau)}}{\left(1 - A \times P \times \left(1 - (X_C(\tau))^{2.2} \right) \right)}} \right] \text{ at interface } X = X_C(\tau) \quad (5.37)$$

Solving Eq. 5.35-5.37 results in

$$\theta_\beta = \delta \times (X - X_C(\tau)) + \frac{1}{2} \left[\theta_{\beta\alpha} + \sqrt{\theta_{\beta\alpha}^2 + \frac{4Z_\beta \theta_{\beta\alpha} \delta}{\left(1 - A \times P \times \left(1 - (X_C(\tau))^{2.2} \right) \right)}} \right] \quad (5.38)$$

The dimensionless surface concentration ($\theta_{\beta S}$) can be obtained by substituting $X = 1$ in Eq. 5.38.

$$\theta_{\beta S} = \delta \times (1 - X_C(\tau)) + \frac{1}{2} \left[\theta_{\beta\alpha} + \sqrt{\theta_{\beta\alpha}^2 + \frac{4Z_\beta \theta_{\beta\alpha} \delta}{\left(1 - A \times P \times \left(1 - (X_C(\tau))^{2.2} \right) \right)}} \right] \quad (5.39)$$

The unknown interface position $X_C(\tau)$ in Eq. 5.39 can be calculated by solving the following equation:

$$\frac{dX_C(\tau)}{d\tau} = \frac{-2\delta}{\left[\theta_{\beta\alpha} + \sqrt{\theta_{\beta\alpha}^2 + \frac{4Z_\beta \theta_{\beta\alpha} \delta}{\left(1 - A \times P \times \left(1 - (X_C(\tau))^{2.2}\right)\right)}} \right]} \quad (5.40)$$

Eq. 5.40 is obtained by rearranging Eq. 5.30 with the aid of Eq. 5.38. The initial condition for Eq. 5.39 is $X_C(\tau) = 1$ at $\tau = 0$.

To cross check the accuracy of PSS solution, the solution obtained from Eq. 5.39 is compared with the solution obtained for system of equations using numerical method of lines (MOL). For particular values of parameters, the dimensionless interface position ($X_C(\tau)$) and the dimensionless surface concentration ($\theta_{\beta s}$) as a function of time are determined using both the methods. To find out the region of validity for PSS solution, the dimensionless interface position and the dimensionless surface concentration as a function of time are determined at different current densities ($i = 0.1, 0.2, 0.5,$ and $1C$ or $\delta = 0.001, 0.002, 0.005,$ and 0.01) and at different Z_β values ($0.004, 4$). To change the dimensionless parameter Z_β , while keeping the dimensionless current density (δ) constant, the parameter M is changed and the parameter D_β is kept constant.

Figures 5.8 and 5.9 show the dimensionless interface position and dimensionless surface concentration at different current densities and at $Z_\beta = 0.004$, obtained from both the methods. The profiles for interface position at different current densities obtained from PSS solution match with the profiles obtained from MOL. The surface concentration profiles obtained from PSS solution match reasonably with the profiles

obtained from MOL, though the sudden increase in surface concentration is not well predicted by PSS solution. Similarly, Figures 5.10 and 5.11 show the dimensionless interface position and dimensionless surface concentration at different current densities and at $Z_\beta = 4$, obtained from both the methods. From Figure 5.10, it is evident that the PSS solution underpredicts the time for the interface to reach center of the particle, at all currents. Similar behavior can be observed in concentration profiles (Figure 5.11). From these results, it can be concluded that the pseudosteady-state solution is valid for very low values of the parameter Z_β ($Z_\beta = 0.004$) or very high values of interface mobility.

5.1.7 Parameter Estimation for D_β , M , n , and A

For Sample A:

In order to predict the discharge curves of sample A from the modified SCM-1, the value of the parameters $C_{\beta\alpha}$, C_t , x_0 , ρ , i_0 , D_β , A , M , and n have to be known. The values of parameters $C_{\beta\alpha}$, C_t , x_0 , ρ , and i_0 for sample A are obtained from experiments (ref. to section 3.4.2 and 3.4.3). Since the effect of the accommodation energy on the phase transformation is not known, the value of the accommodation energy factor “ A ” is taken as 1; this case will be considered as the base case, and it will be decreased with the

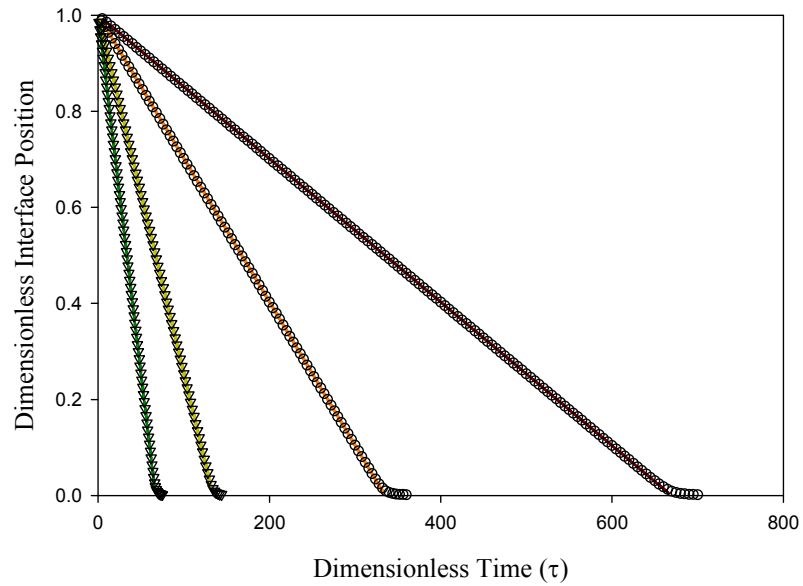


Figure 5.8: Dimensionless interface position as a function of dimensionless time at different current densities (From left: 1C, 0.5C, 0.2C, and 0.1C) obtained from PSS (Lines) and numerical method of lines (Symbols) (Values of the parameters used: $D_{\beta} = 3.8 \times 10^{-15} \text{ m}^2/\text{s}$, $M = 1 \times 10^{-8} \text{ m.mol}/(\text{J.s})$, $Z = 0.0004$)

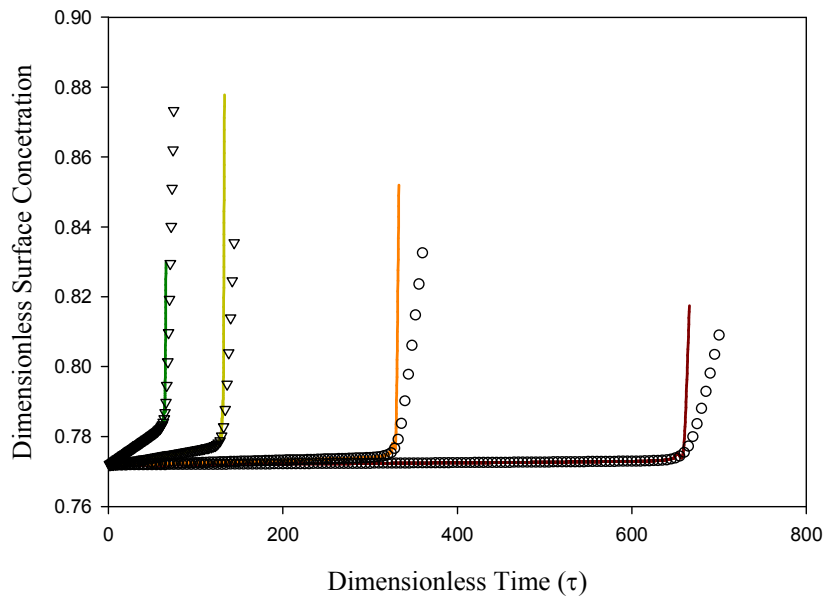


Figure 5.9: Dimensionless surface concentration as a function of dimensionless time at different current densities (From left: 1C, 0.5C, 0.2C, and 0.1C) obtained from PSS (Lines) and numerical method of lines (Symbols) (Values of the parameters used: $D_{\beta} = 3.8 \times 10^{-15} \text{ m}^2/\text{s}$, $M = 1 \times 10^{-8} \text{ m.mol}/(\text{J.s})$, $Z = 0.0004$)

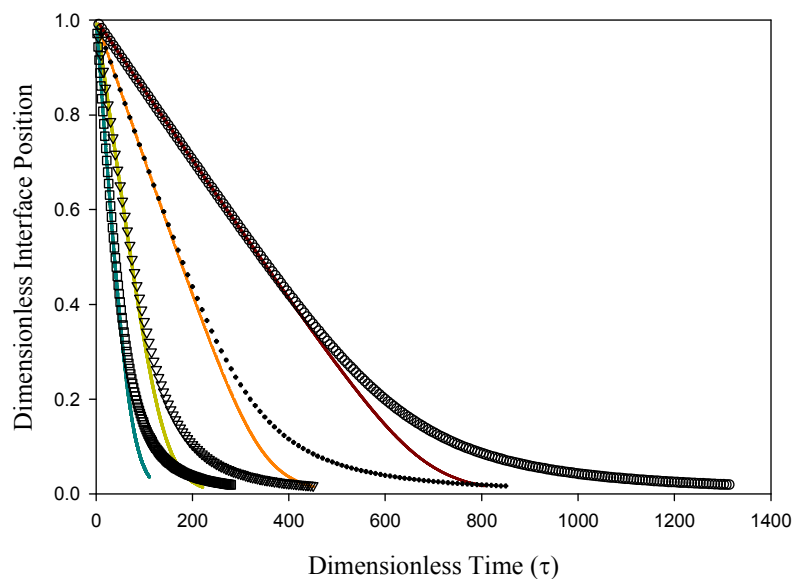


Figure 5.10: Dimensionless interface position as a function of dimensionless time at different current densities (From left: 1C, 0.5C, 0.2C, and 0.1C) obtained from PSS (Lines) and numerical method of lines (Symbols) (Values of the parameters used: $D_{\beta} = 3.8 \times 10^{-15} \text{ m}^2/\text{s}$, $M = 1 \times 10^{-12} \text{ m.mol}/(\text{J.s})$, $Z = 4$)

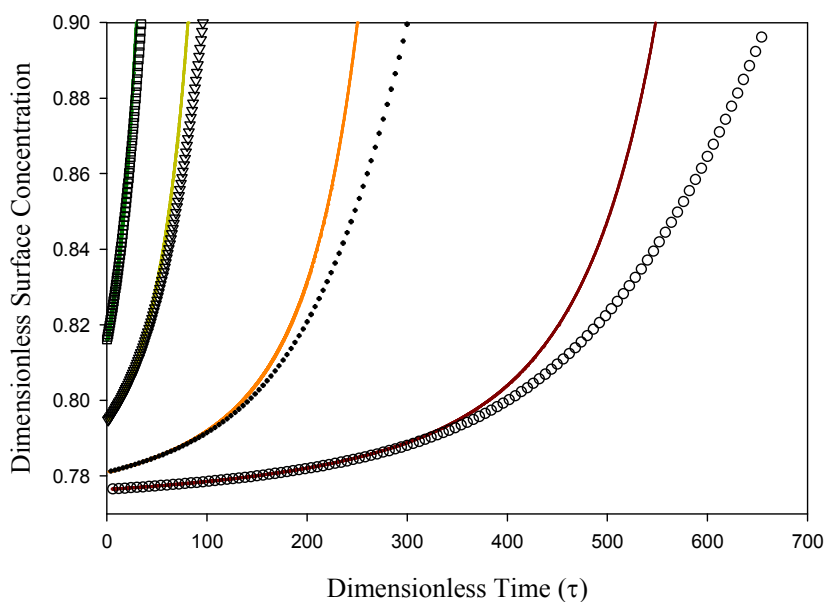


Figure 5.11: Dimensionless surface concentration as a function of dimensionless time at different current densities (From left: 1C, 0.5C, 0.2C, and 0.1C) obtained from PSS (Lines) and numerical method of lines (Symbols) (Values of the parameters used: $D_{\beta} = 3.8 \times 10^{-15} \text{ m}^2/\text{s}$, $M = 1 \times 10^{-12} \text{ m.mol}/(\text{J.s})$, $Z = 4$)

decrease in volume change. Since there are no accurate experimental techniques to determine the value of the parameters D_β , M , and n for phase transformation electrodes, the values of these parameters are obtained by trial and error method. Initially guess values are given to these parameters and the profiles for dimensionless surface concentration as a function of time at 5C and 2C currents are determined. From the surface concentration profiles, the profiles for equilibrium potential, the over-potential and the voltage at 5C and 2C currents during the discharge are determined. In general, the slope and length of initial and final descending lines, and voltage plateaus in the discharge curve differ from one LiFePO_4 sample to another LiFePO_4 sample, depending on the type of material preparation process and electrode preparation process. As a result, the exact prediction of the slope and length of initial and final descending lines, and voltage plateaus at different current densities is possible only for one set of parameter values. Hence, if the discharge curves obtained from modified SCM-1 at 5C and 2C currents, matches with the experimental discharge curves (Figure 5.12), guess values given are considered as the real values of the parameters D_β , M , and n for sample A. Once the values of these parameters are determined, using these values, discharge curves at other current densities are determined from modified SCM-1. In case of mismatch between experimental discharge curves and discharge curves obtained from modified SCM-1, the guess values are changed and the above procedure is repeated.

By using this procedure, the fitted values for parameters D_β , M , and n for sample A are found to be $8 \times 10^{-14} \text{ m}^2/\text{s}$, $1.3 \times 10^{-11} \text{ m.mol}/(\text{J.s})$, and 2.2, respectively. The methodology adopted here for parameter estimation and model validation is similar to that of earlier works published in the literature [22,53,66].

For Sample B:

Similarly, the experimental discharge curves at 20C and 10C for sample B (Figure 5.13) are used to estimate the values of parameters D_β , M , and n of Sample B. The values of parameters used in this simulation for Samples A and B are listed in Table 1.

5.1.8 Model Validation

Since experimental discharge curves at two particular currents are used to predict the values of the parameters D_β , M , and n , experimental discharge curves at other currents are used to validate the model. If the predicted discharge curves from the model at other currents match with the experimental discharge curves, the model is considered as validated. Here, the modified shrinking core model is validated by (i) comparing the

Table 5.1: List of parameter values used for modeling LiFePO_4 cathode materials and for further analysis

Parameter	LiFePO_4	LiFePO_4
	Sample A	Sample B
Length of the FePO_4 particle ($2x_0$) (μm)	0.8	0.8
Density of FePO_4 particle (ρ) (g/cm^3)	3.6	3.6
Chemical diffusion coefficient in β phase (D_β) (m^2/s)	8×10^{-14}	3.2×10^{-13}
Interface mobility (M) ($\text{m.mol}/(\text{J.s})$)	1.3×10^{-11}	1.85×10^{-10}
Dimensionless equilibrium concentration of Li rich phase ($C_{\beta\alpha}/C_t$)	0.77	0.85
Exchange current (i_0) (A/g)	0.1	0.25
Accommodation energy factor (A)	1.0	1.0
N	2.2	2.2
C_t (mol/cm^3)	0.02044	0.02119

calculated discharge curves of sample A at different current densities (1C, 0.5C, 0.2C, and 0.1C) by using parameters estimated from fitting experimental discharge curves at other currents (2C and 5C) with experimental discharge curves at same currents (1C, 0.5C, 0.2C, and 0.1C); (ii) simulating and comparing with experimental discharge curves of two LiFePO_4 samples which have large difference in rate performance; and (iii) comparing the modified SCM-1 at high interface mobility ($M \rightarrow \infty$) with conventional SCM. Figure 5.12 shows the voltage vs. discharge capacity curves for LiFePO_4/A at different currents (0.1C to 5C) obtained from the experiment and the model predictions. Plateau potentials, end of discharge values, and discharge curves obtained from the model seem to match well with the experimental results at all currents. By using the estimated parameter values for Sample B in the model, the discharge curves at 5C, 2C, 1C, 0.5, 0.2C, and 0.1C are obtained and are also compared with the experimental discharge curves as shown in Figure 5.13.

From the comparison of experimental and model discharge curves for samples A and B, one can see a strong validation of the model in predicting the discharge behavior. Apart from this, when the interface mobility is changed to 1.3×10^{-8} m.mol/(J.s), the modified SCM-1 predictions for discharge behavior at different currents are similar to the discharge behavior predicted from the SCM in rectangular geometry (Figure 5.14). Here, it should be noted that the SCM used is a particle scale model and it does not include the porous electrode theory. The similarity in the results obtained from both models also strongly supports the applicability of the model to a wide range of electrodes whose discharge process is controlled by either diffusion or rate of phase transformation.

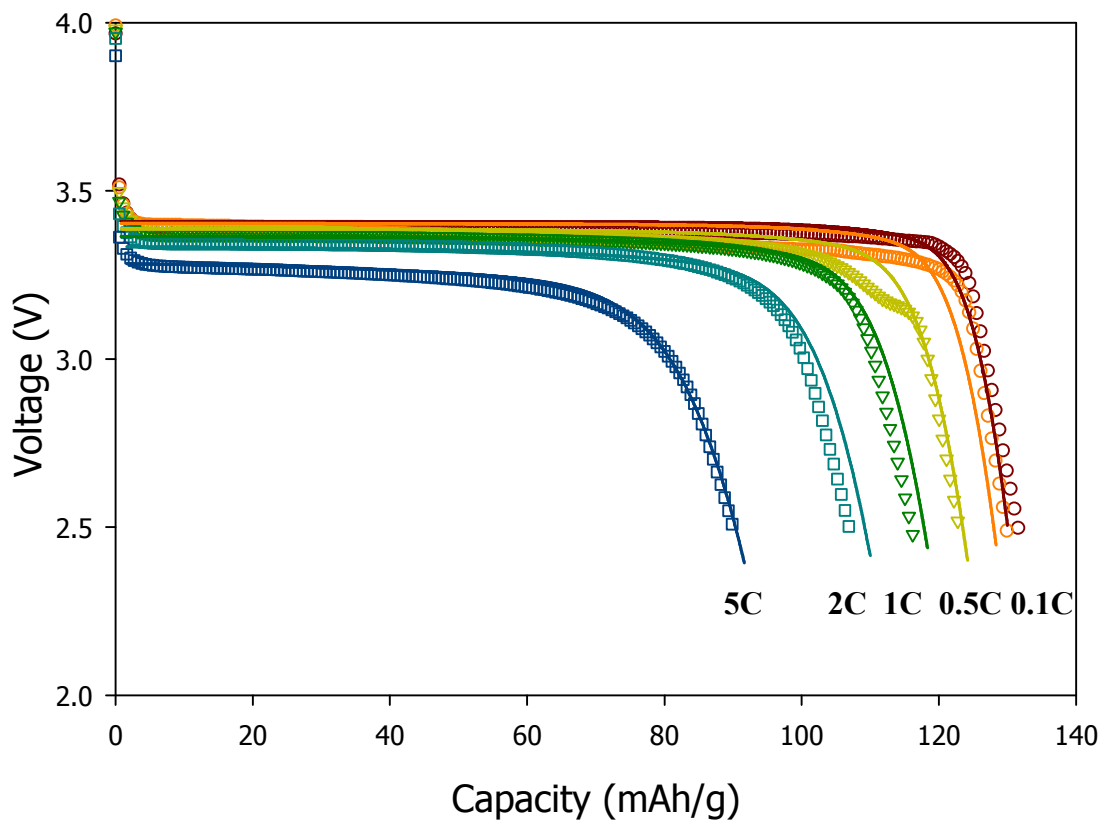


Figure 5.12: Discharge curves of LiFePO₄/A obtained from experiment and modified SCM-1 at 5C, 2C, 1C, 0.5C, 0.2C, and 0.1C (symbols: Experiment, lines: Model)

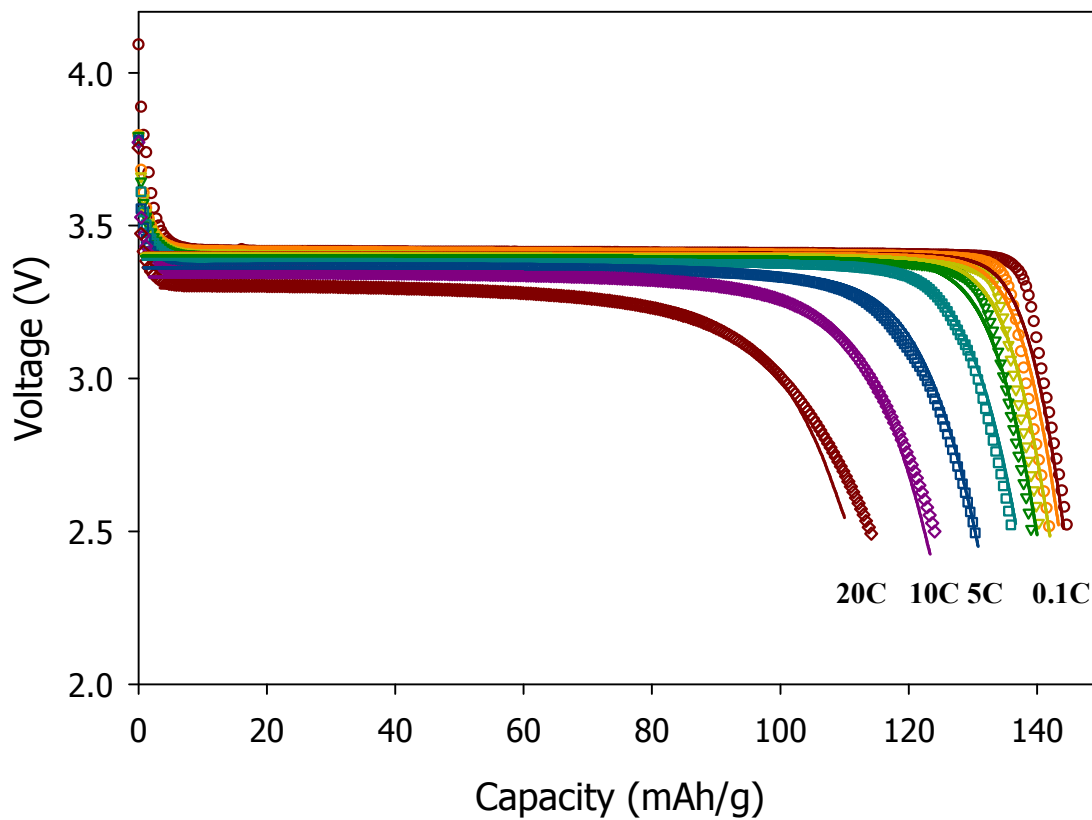


Figure 5.13: Discharge curves of LiFePO₄/B obtained from experiment and modified SCM-1 at 20C, 10C, 5C, 2C, 1C, 0.5C, 0.2C, and 0.1C (symbols: Experiment, lines: Model)

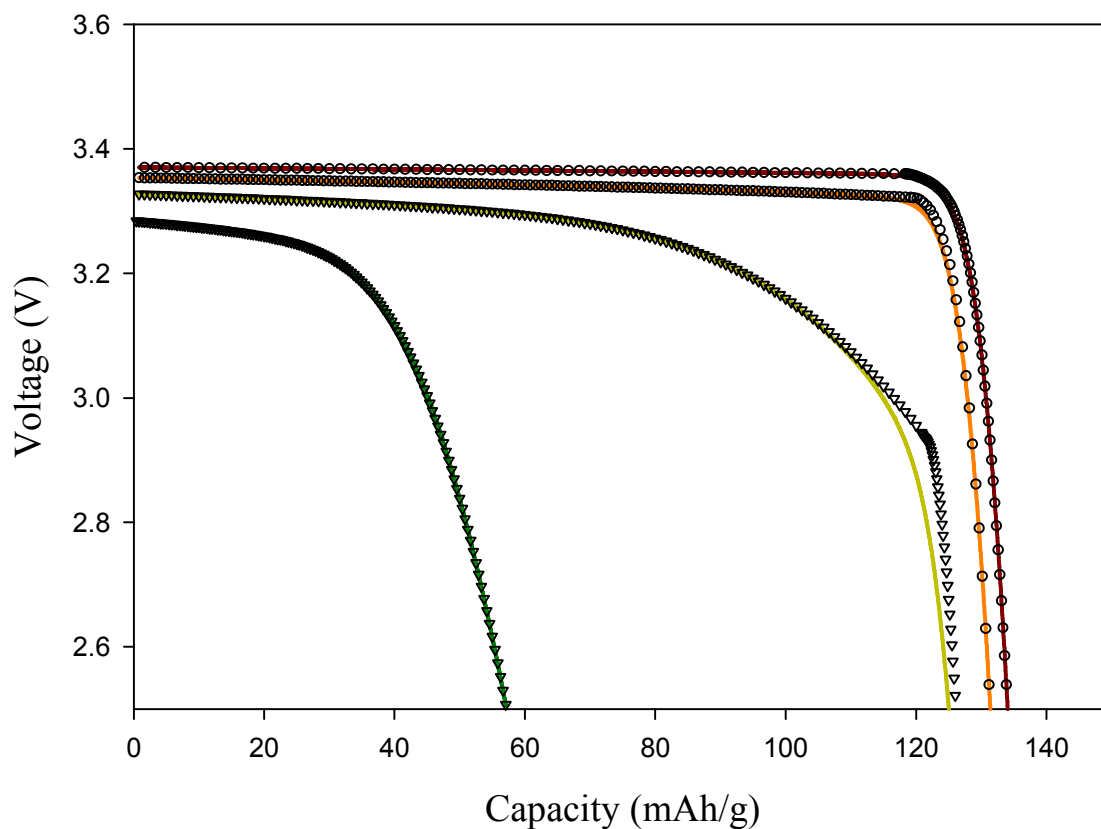


Figure 5.14: Discharge curves at 5C, 2C, 1C, 0.5C obtained from modified SCM-1 (with $M = 1 \times 10^{-8}$ m.mol/(J.s), $n = 2.2$) and SCM with rectangular geometry (particle scale model only). Values of the common parameters for both the models: $D_{\beta} = 8 \times 10^{-16}$ m²/s, $i_0 = 0.1$ A/g, $C_t = 0.02044$ mol/cm³, $\rho = 3.6$ gm/cm³, $\theta_{\beta\alpha} = 0.7718$.

5.2 Modified SCM-2: Model Involving Transport in α and β Phases

As mentioned in section 2.1, Chiang et al. [24,25,26] have reported that the rate capability of LiFePO_4 can be improved by increasing its solid solution range. Ever since this finding, there has been lot of interest in developing LiFePO_4 cathode materials with extended solid solution. Although the modified SCM-1 is able to predict the discharge behavior of samples A and B, it cannot be used for predicting the discharge behavior of LiFePO_4 materials with extended solid solution limits such as $\text{Li}_{0.99}\text{Nb}_{0.01}\text{FePO}_4$ [24,25]. This is due to the assumption used in the model that lithium solubility in lithium deficient (α) phase is negligible. Since samples A and B have very narrow initial solid solution (α) region, the effect of Li^+ ion transport in this region has negligible influence on the rate capability. However, for electrode materials such as $\text{Li}_{0.99}\text{Nb}_{0.01}\text{FePO}_4$, the Li^+ ion transport processes in the initial solid solution region cannot be neglected. Hence to predict the discharge behavior of electrode materials with extended solid solution and to determine the influence of solid solution range on rate capability, modified SCM-1 needs to be further modified. This new model should account for the three key processes taking place in LiFePO_4 during discharge: (1) Diffusion of Li^+ ion in Li rich (β) phase, (2) Transfer of Li^+ ion across the α/β phase boundary (*phase transformation*), and (3) diffusion of Li^+ ion in Li deficient (α) phase. Prior to developing the new model, it is essential to understand the lithium ion concentration distribution in FePO_4 particle during discharge.

5.2.1 Li⁺ ion Concentration Distribution in the LiFePO₄ Particle during Discharge Process

At the beginning of the discharge process, Li⁺ ion inserts into surfaces of the electrode particle and diffuses into the interior of the particle. This process results in the formation of α solid solution, and the process continues until the Li⁺ ion content (x) in Li_xFePO₄ reaches the solid solubility limit ($C_{\alpha\beta}$). This process corresponds to the initial potential sloping line in the discharge curve (a-b section in Figure 5.15). Further insertion of Li⁺ ion into the lattice leads to the saturation of lithium ion in the solid solution phase (Li_xFePO₄). When the lithium ion saturation level (x) in the solid solution phase reaches $C_{\alpha i}$, a β phase with concentration of $C_{\beta i}$ will be formed in the α matrix, and as a result the value of discharge overpotential increases to the growth overpotential (b'-c' in Figure 5.15). The discharge overpotential is caused by a misfit strain energy resulting from the molar volume difference between α and β phases. During further discharge, the β phase formed in the electrode near the boundary gradually increases in size, forming a continuous β phase layer with a lithium concentration of $C_{\beta i}$ (c' in Figure 5.15) at the interface, which is higher than equilibrium concentration $C_{\beta\alpha}$. In addition to this, the interface concentration of the α phase ($C_{\alpha i}$) is also higher than the equilibrium concentration ($C_{\alpha\beta}$). The growth of the β phase corresponds to the c'-d' section in Figure

5.15. The relative difference $(\frac{C_{\beta i} - C_{\beta\alpha}}{C_{\beta\alpha}}, \frac{C_{\alpha i} - C_{\alpha\beta}}{C_{\alpha\beta}})$ between the real and equilibrium

interface concentrations in α and β phases will act as driving force to overcome the energy barrier (misfit accommodation energy and interfacial energy) for phase growth.

Further, lithium insertion will result in a growth of the β phase toward the center of the particle. Once the α phase completely transforms into the β phase, subsequent lithium will start to dissolve into β phase and form a solid solution with lithium ion concentration varying from $C_{\beta i}$ to I (c'-d section in Figure 5.15).

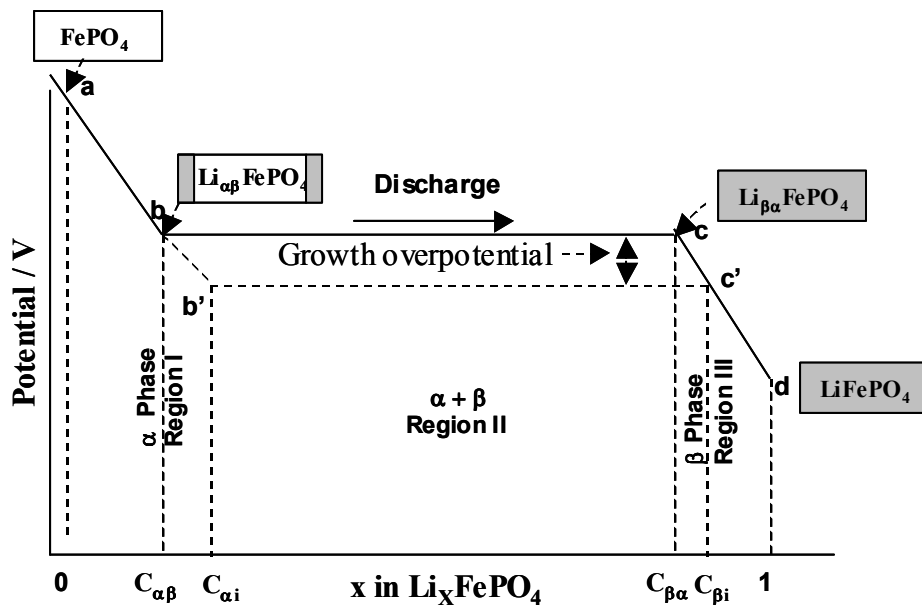
5.2.2 Governing Equations and Boundary Conditions

The lithium ion diffusion process in LiFePO_4 during the discharge process can be modeled by modifying the transport equations proposed by Zhang et al. [66] based on the theory of mixed-mode phase transformations (ref. to section 5.1.3). Since the discharge process is assumed to be controlled by a mixed-ion diffusion process and phase transformation, the interfacial Li rich phase concentration ($C_{\beta i}$) and interfacial Li deficient phase concentration ($C_{\alpha i}$) will be different from the equilibrium concentrations $C_{\beta\alpha}$ and $C_{\alpha\beta}$ in region II (Figure 5.15b). In addition, the transport equations reflect the use of Cartesian geometry instead of spherical geometry. The differential equations, initial condition, and boundary conditions of the governing model can be written as follows:

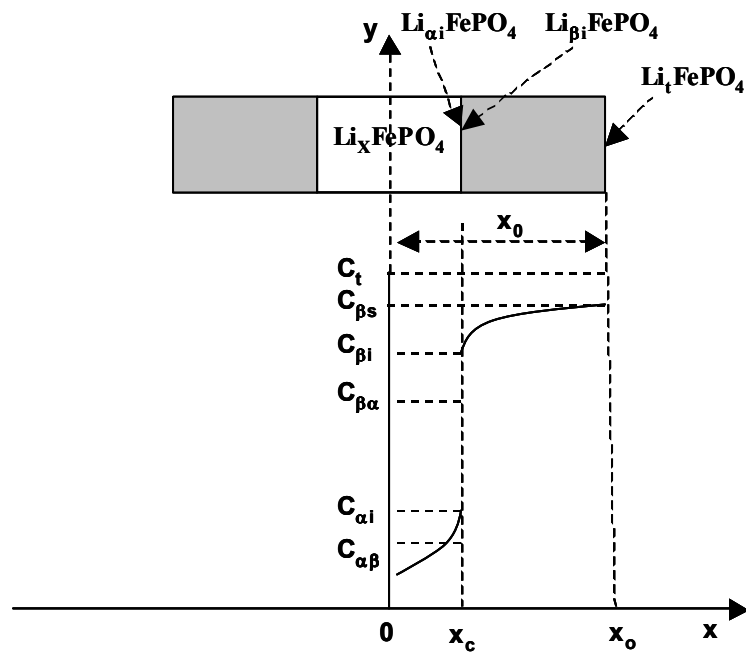
Region I ($0 \leq x \leq x_0$):

$$\frac{\partial C_{\alpha}}{\partial t} = D_{\alpha} \left(\frac{\partial^2 C_{\alpha}}{\partial x^2} \right) \quad (5.41)$$

$$C_{\alpha} = 0, \quad t = 0 \quad (5.42)$$



(a)



(b)

Figure 5.15: Schematic showing (a) phase transformation and (b) Li^+ ion concentration distribution during the discharge of a LiFePO_4 particle (Li insertion into FePO_4).

$$D_{\alpha} \left(\frac{\partial C_{\alpha}}{\partial x} \right) = \frac{i}{F}, x = x_0 \quad (5.43)$$

$$\frac{\partial C_{\alpha}}{\partial x} = 0, x = 0 \quad (5.44)$$

When the concentration at the particle surface ($x = x_0$) reaches the maximum solubility of the initial solid solution α phase ($C_{\alpha\beta}$), the discharge process enters into the second region.

Region II:

In α Phase ($0 \leq x \leq x_C(t)$):

$$\frac{\partial C_{\alpha}}{\partial t} = D_{\alpha} \left(\frac{\partial^2 C_{\alpha}}{\partial x^2} \right) \quad (5.45)$$

$$\frac{\partial C_{\alpha}}{\partial x} = 0, x = 0 \quad (5.46)$$

$$C_{\alpha} = C_{\alpha\beta}, x = x_C(t) \quad (5.47)$$

The initial condition for Eq. 5.45 is given by the lithium ion concentration profile inside the particle (in region I) taken when the surface concentration $C_{\alpha}|_{x=x_0}$ reaches $C_{\alpha\beta}$.

In β Phase ($x_C(t) \leq x \leq x_0$):

$$\frac{\partial C_{\beta}}{\partial t} = D_{\beta} \left(\frac{\partial^2 C_{\beta}}{\partial x^2} \right) \quad (5.48)$$

$$C_{\beta} = C_{\beta\alpha}, t = 0 \quad (5.49)$$

$$D_{\beta} \left(\frac{\partial C_{\beta}}{\partial x} \right) = \frac{i}{F}, x = x_0 \quad (5.50)$$

$$C_{\beta} = C_{\beta i}, x = x_C(t) \quad (5.51)$$

The position of the interface ($x_C(t)$) can be determined by performing a mass balance of lithium ions at the interface:

$$\frac{dx_C(t)}{dt} = \frac{D_{\alpha} \left(\frac{\partial C_{\alpha}}{\partial x} \right)_{x=x_C(t)} - D_{\beta} \left(\frac{\partial C_{\beta}}{\partial x} \right)_{x=x_C(t)}}{(C_{\beta i} - C_{\alpha i})} \quad (5.52)$$

When the interface reaches the center of the particle ($x_C(t)=0$), i.e. when the particle is completely full of β phase, the discharge process enters into the third region:

Region III ($0 \leq x \leq x_0$):

$$\frac{\partial C_{\beta}}{\partial t} = D_{\beta} \left(\frac{\partial^2 C_{\beta}}{\partial x^2} \right) \quad (5.53)$$

$$D_{\beta} \left(\frac{\partial C_{\beta}}{\partial x} \right) = \frac{i}{F}, x = x_0 \quad (5.54)$$

$$\frac{\partial C_{\beta}}{\partial x} = 0, x = 0 \quad (5.55)$$

The initial condition for Eq. 5.53 is given by the lithium ion concentration profile inside the β phase at the end of the region II.

In order to solve the system of equations in region II (Eqs. 5.45-5.52), the interfacial concentration of the β and the α phases ($C_{\beta i}$ and $C_{\alpha i}$) need to be determined.

The Li deficient phase concentration at the interface (C_{ai}) in Figure 5.15 can be estimated by considering the driving force to be equal in both the phases.

$$\frac{C_{ai} - C_{\alpha\beta}}{C_{\alpha\beta}} = \frac{C_{\beta i} - C_{\beta\alpha}}{C_{\beta\alpha}} \quad (5.56)$$

Eq. 5.56 implies that the overpotential resulting from phase transformation kinetics is equal in both the phases (Figure 5.15a).

The Li rich phase concentration at the interface ($C_{\beta i}$) is determined from the theory of mixed-mode phase transformations (ref. to section 5.1.3), which is given below.

$$\left(\frac{C_{\beta i}}{C_{\beta\alpha}} + \frac{C_{ai}}{C_{\alpha\beta}} - 2 \right) \times (C_{\beta i} - C_{ai}) = \frac{D_{\beta} \left(\frac{\partial C_{\beta}}{\partial x} \right)_{x=x_C(t)} - D_{\alpha} \left(\frac{\partial C_{\alpha}}{\partial x} \right)_{x=x_C(t)}}{MRT \left(1 - A \times P \times \left(1 - (x_C(t))^n \right) \right)} \quad (5.57)$$

As mentioned earlier, due to the micrometer particle size of sample A and sample B, the interface in these samples is assumed to be semi-coherent.

5.2.3 Solution Methodology

Eqs. 5.41-5.57 are converted to dimensionless form using the following variables.

$$\theta_{\alpha} = \frac{C_{\alpha}}{C_t} \quad \theta_{\alpha\beta} = \frac{C_{\alpha\beta}}{C_t} \quad \theta_{ai} = \frac{C_{ai}}{C_t} \quad \theta_{\alpha S} = \frac{C_{\alpha S}}{C_t} \quad \theta_{\beta} = \frac{C_{\beta}}{C_t} \quad \theta_{\beta\alpha} = \frac{C_{\beta\alpha}}{C_t}$$

$$\theta_{\beta i} = \frac{C_{\beta i}}{C_t} \quad \theta_{\beta S} = \frac{C_{\beta S}}{C_t} \quad X = \frac{x}{x_0} \quad X_C = \frac{x_c}{x_0} \quad \tau = \frac{t D_{\beta}}{x_0^2}$$

$$\delta_1 = \frac{i \rho x_0^2}{D_{\alpha} C_t F} \quad \delta_2 = \frac{i \rho x_0^2}{D_{\beta} C_t F} \quad Z_{\beta} = \frac{D_{\beta}}{MRT x_0} \quad Z_{\alpha} = \frac{D_{\alpha}}{MRT x_0}$$

The resulting dimensionless equations correspond to a nonlinear coupled moving boundary value problem. The procedure mentioned in section 4.1.1 is used to solve the system of equations to obtain the profiles for dimensionless surface concentration. To check for the accuracy of the method of lines, the system of equations is also solved by using the numerical approach mentioned in ref [66]. The comparison between the results obtained from two methods indicates that they match well, which shows the accuracy of numerical method of lines in solving moving boundary type problems.

5.2.4 Equations for Equilibrium Potential and Overpotential

Equilibrium Potential:

To obtain the discharge curves from the model developed in section 5.2.2, the equations for equilibrium potential and the overpotential needs to be determined. Here, it should be noted that the equilibrium potential equations presented in section 4.1.2 could not be used for the new model, as the initial potential sloping line or the initial solid solution (α) region is neglected. To consider the initial solid solution region, Eqs. 4.1 and 4.2 are modified as follows:

For Sample A:

$$U = 3.3929 + 0.63 \times e^{(-500(x)^{1.2})} - 6.5 \times e^{\left(\frac{-0.52}{(x)^{12.5}}\right)} \quad (5.58)$$

For Sample B:

$$U = 3.4245 + 0.85 \times e^{(-800(x)^{1.3})} - 17 \times e^{\left(\frac{-0.98}{(x)^{14}}\right)} \quad (5.59)$$

where Li^+ ion content x in LiFePO_4 in Eqs. 5.58 and 5.59 is the ratio of the surface concentration to the maximum concentration of lithium that can be incorporated into FePO_4 lattice (C_t).

Figures 5.16 and 5.17 show the equilibrium potential curves for samples A and B obtained from GITT experiments and empirical equations. From these figures, a close match can be observed between experimental results and the empirical equations. The solid phase lithium concentration at the surface, obtained by solving the system of equations, is inserted into the Eqs. 5.58 and 5.59 and the equilibrium potential as a function of time is then calculated.

Over potential:

The over potential can be calculated using following equation [58],

$$i = i_o \left(\frac{(C_t - C_{as})}{\left(C_t - \left(\frac{C_{\alpha}|_{x=0} + C_{as}}{2} \right) \right)} \times e^{\left(\frac{\alpha F \eta(t)}{RT} \right)} - \frac{C_{as}}{\left(\frac{C_{\alpha}|_{x=0} + C_{as}}{2} \right)} \times e^{\left(-\frac{\alpha F \eta(t)}{RT} \right)} \right)$$

for region I

(5.60)

$$i = i_o \left(\frac{(C_t - C_{\beta s})}{(C_t - C_{\beta \alpha})} \times e^{\left(\frac{\alpha F \eta(t)}{RT} \right)} - \frac{C_{\beta s}}{C_{\beta \alpha}} \times e^{\left(-\frac{\alpha F \eta(t)}{RT} \right)} \right) \text{ for}$$

region II and region III

(5.61)

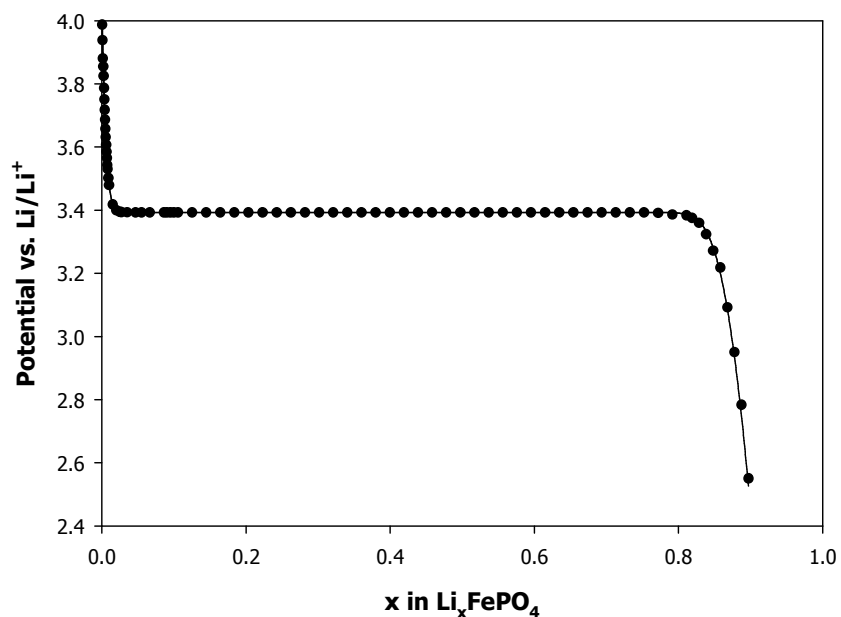


Figure 5.16: Equilibrium Potential vs. Li content x in $\text{Li}_x\text{FePO}_4/\text{A}$ obtained from Experiment (Symbols) and Eq. 5.58 (Line)

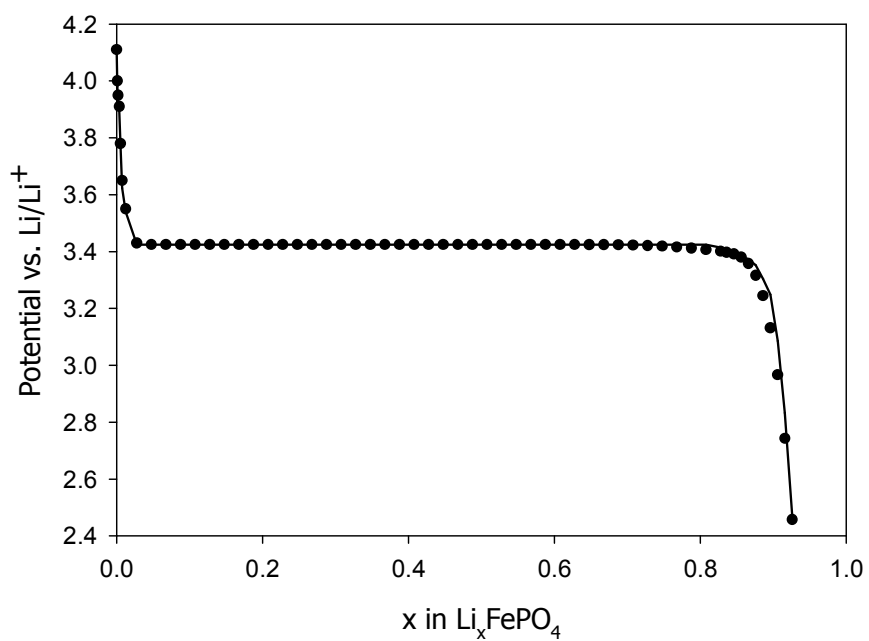


Figure 5.17: Equilibrium Potential vs. Li content x in $\text{Li}_x\text{FePO}_4/\text{B}$ obtained from Experiment (Symbols) and Eq. 5.59 (Line)

Where i_0 is the exchange current, $C_{\beta S}$ is the surface concentration in the β phase, $C_{\alpha S}$ is the surface concentration in the α phase and $C_{\alpha} \Big|_{x=0}$ is the concentration at the center of the particle. $\frac{C_{\alpha t} + C_{\alpha S}}{2}$ is approximately equal to the equilibrium concentration. The voltage of LiFePO_4 electrode is calculated by adding the overpotential to the equilibrium potential.

5.2.5 Parameter Estimation

To obtain the discharge curves from the modified SCM-2, the values of the parameters $C_{\beta\alpha}$, $C_{\alpha\beta}$, C_t , x_0 , ρ , i_0 , A , D_{β} , D_{α} , M , and n have to be known. The values of the parameters $C_{\beta\alpha}$, $C_{\alpha\beta}$, C_t , x_0 , ρ , and i_0 are obtained from experiments (refer to section 3.4). The procedure for estimating the values of the parameters A , D_{β} , M , and n is given in section 5.1.7. By using this procedure, the estimated values for D_{β} , M , and n for sample A are $8 \times 10^{-14} \text{ m}^2/\text{s}$, $7.3 \times 10^{-12} \text{ m mol}/(\text{J}\cdot\text{s})$, and 2.2, respectively, and the estimated values for D_{β} , M , and n for sample B are $3.2 \times 10^{-13} \text{ m}^2/\text{s}$, $1.05 \times 10^{-10} \text{ m mol}/(\text{J}\cdot\text{s})$, and 2.2, respectively. The diffusion coefficient in the α phase is considered to be six times higher than that of the β phase [82] and no additional efforts are made to determine the value from fitting or other approaches. The values of parameters used in this simulation for Samples A and B are listed in Table 5.2.

5.2.6 Model Validation

The procedure mentioned in section 5.1.8 is used to validate the modified SCM-2. Different from the modified SCM-1, the new model is validated by matching not only the plateau potentials, the end of discharge values, but also the initial discharge curves of samples A and B, which cannot be done by the modified SCM-1. Figures 5.18 and 5.19 show the voltage vs. discharge capacity curves for the samples A and B LiFePO_4 at different currents, obtained from experiment and the modified SCM-2. The excellent agreement between the experimental and the modeling results at all currents is due to the low active material loading (3 mg/cm^2). As mentioned earlier, Sample B has higher rate capability than sample A. The reason for high rate capability of sample B can be determined by comparing the parameters values for samples A and B (Table 5.2). From Table 5.2, it is evident that both the samples have same diffusion length and sample A has higher solid solution range than sample B. From the results on rate capability of $\text{Li}_{0.99}\text{Nb}_{0.01}\text{FePO}_4$ [24,25], it is understood that LiFePO_4 materials with higher solid solution range will exhibit high rate capability. However, in spite of having high solid solution range, sample A has lower rate capability than sample B. This is due to 14 times higher interface mobility and 4 times higher β phase chemical diffusion coefficient of sample B.

Table 5.2: List of parameter values used for modeling LiFePO₄ cathode materials

Parameter	LiFePO ₄ Sample A	LiFePO ₄ Sample B
Length of the FePO ₄ particle ($2x_0$) (μm)	0.8	0.8
Density of FePO ₄ particle (ρ) (g/cm^3)	3.6	3.6
Chemical diffusion coefficient in β phase (D_β) (m^2/s)	8×10^{-14}	3.2×10^{-13}
Chemical diffusion coefficient in α phase (D_α) (m^2/s)	$6 \times D_\beta$	$6 \times D_\beta$
Interface mobility (M) ($\text{m.mol}/(\text{J.s})$)	7.3×10^{-12}	1.05×10^{-10}
Dimensionless equilibrium concentration of Li Deficient phase ($\theta_{\alpha\beta}$)	0.015	0.027
Dimensionless equilibrium concentration of Li rich phase ($\theta_{\beta\alpha}$)	0.77	0.85
Exchange current (i_0) (A/g)	0.1	0.25
Accommodation energy factor (A)	1.0	1.0
Proportionality Factor (P)	1.0	1.0
N	2.2	2.2
C_t (mol/cm^3)	0.02044	0.02119

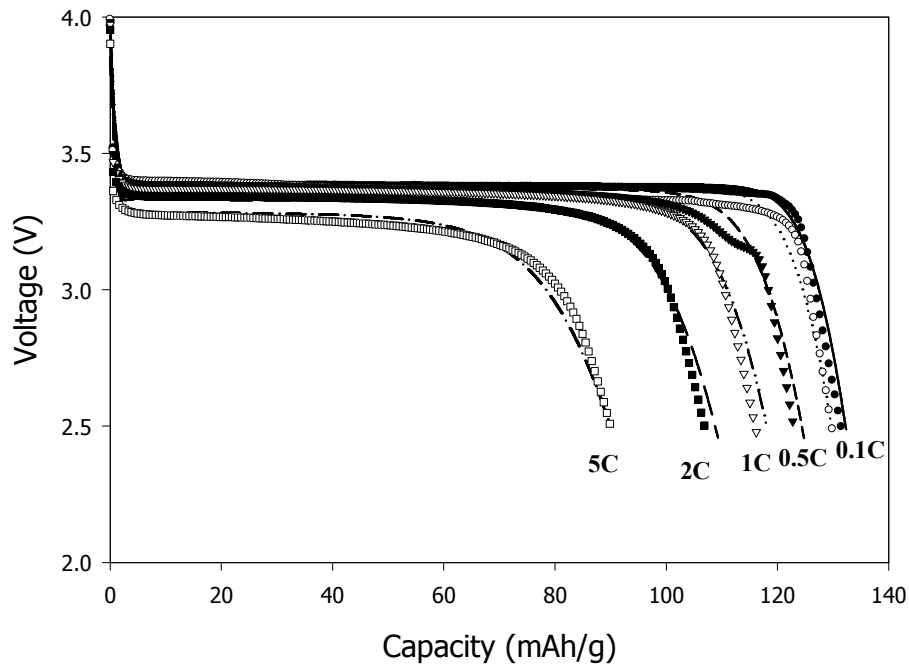


Figure 5.18: Discharge curves of LiFePO₄/A obtained from experiment and modified SCM-2 at 5C, 2C, 1C, 0.5C, 0.2C, and 0.1C (symbols: Experiment, lines: Model)

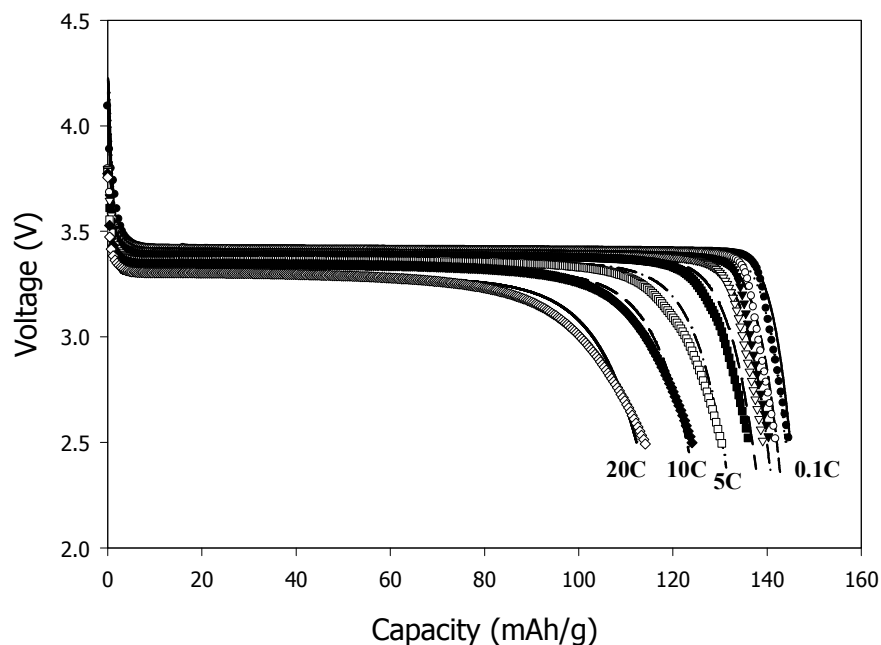


Figure 5.19: Discharge curves of LiFePO_4/B obtained from experiment and modified SCM-2 at 20C, 10C, 5C, 2C, 1C, 0.5C, 0.2C, and 0.1C (symbols: Experiment, lines: Model)

From section 2.1, it is evident that the cation-doped nanoscale LiFePO_4 (sample NC) has high rate capability than LiFePO_4 from Aldrich chemical (sample AC) (Figure 5.20) due to the extended miscibility gap, which resulted from formation of a coherent interface between the α and β phases. To validate the model further, an effort is made to predict the difference in rate capability behaviors of these two samples. Particle size/diffusion length, solid solution limits, and equilibrium potential curves for the two samples are taken from ref [25]. Table 5.3 shows the values of the parameters used in the model for sample AC and sample NC. Sample NC is considered to have coherent interface and Eq. 5.20a is used to define the variation in accommodation energy for

coherent interface. Sample AC is considered to have semi-coherent interface between α and β phases and Eq. 5.20b is used to define the variation in accommodation energy for semi-coherent interface. Since the coherent interface has higher interface mobility than the semi-coherent interface, a higher interface mobility value is used for sample NC compared to sample AC. For both of the samples, the value of the parameter A is taken as 1. This implies that the lattice strains in the samples are high and not relieved. The following equations are used for obtaining the equilibrium potential curves from the model:

For Sample AC:

$$U = 3.442 + 6.5 \times e^{(-2200(x)^{1.3})} - 3.85 \times e^{\left(\frac{-0.98}{(x)^{65}}\right)} \quad (5.62)$$

For Sample B:

$$U = 3.447 + 0.85 \times e^{(-90(x)^{1.3})} - 3.85 \times e^{\left(\frac{-0.98}{(x)^{8.8}}\right)} \quad (5.63)$$

Figure 5.21 shows the rate capability behavior of two samples predicted by the modified SCM-2. The rate capability behavior of the two samples predicted from the model is similar to that of the rate capability behavior observed from experiments, as shown in Figure 5.20. The difference in rate capability observed for the two samples is due to the difference in their solid solution range and the types of interface. These results strongly validate the applicability of the model to electrode materials with different rate-controlling mechanisms, different solid solution ranges, and different interface structures. Hence the model developed in this contribution is applicable for predicting the discharge

behavior of any other electrodes with phase transformation such as $\text{Li}_4\text{Ti}_5\text{O}_{12}$ in Li ion battery and metal-hydride electrodes in Ni/MH batteries.

Table 5.3: The values of the parameters used in the model for Sample AC and Sample NC.

Parameter	LiFePO₄ Sample AC	LiFePO₄ Sample NC
Length of the FePO ₄ particle ($2x_0$) (μm)	0.113	0.043
Density of FePO ₄ particle (ρ) (g/cm^3)	3.6	3.6
Chemical diffusion coefficient in β phase (D_β) (m^2/s)	8×10^{-16}	8×10^{-18}
Chemical diffusion coefficient in α phase (D_α) (m^2/s)	$6 \times D_\beta$	$6 \times D_\beta$
Interface mobility (M) ($\text{m.mol}/(\text{J.s})$)	7.0×10^{-12}	7.3×10^{-11}
Dimensionless equilibrium concentration of Li Deficient phase ($\theta_{\alpha\beta}$)	0.01	0.117
Dimensionless equilibrium concentration of Li rich phase ($\theta_{\beta\alpha}$)	0.98	0.804
Exchange current (i_0) (A/g)	0.1	0.1
Accommodation energy factor (A)	1.0	1.0
Proportionality Factor (P)	1.0	0.5
N	2.2	2.2
C_t (mol/cm^3)	0.02030	0.02032

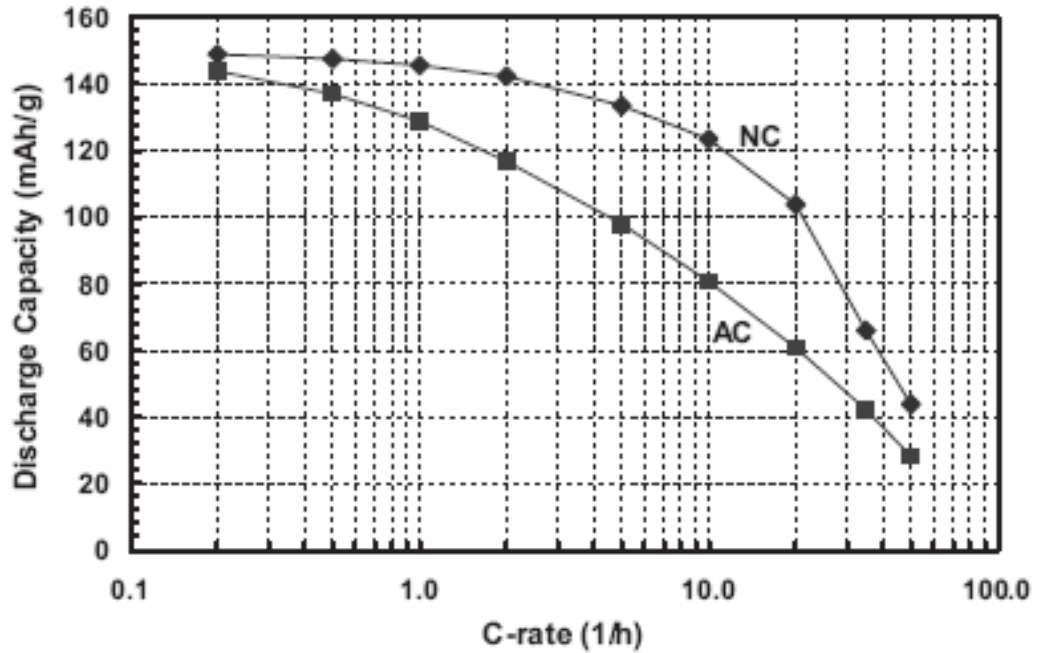


Figure 5.20: Comparison of specific discharge capacity versus galvanostatic discharge rate for Sample NC (top) Sample AC (bottom) (Figure taken from ref. 25)

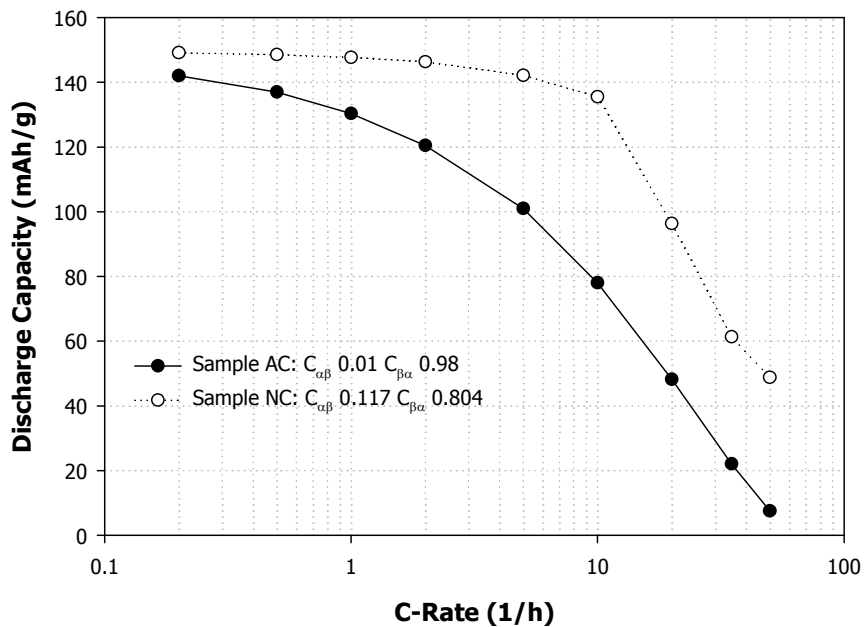


Figure 5.21: Rate capability behavior predicted from the modified SCM-2 for Sample NC and Sample AC reported in ref [25]. Parameters used for Sample NC: D_{β} : $1 \cdot 10^{-17} \text{ m}^2/\text{s}$, M : $3 \cdot 10^{-11} \text{ m.mol}/(\text{J.s})$, $A=1$, $P= 0.5$, Interface=Coherent. Parameters used for Sample AC: D_{β} : $8 \cdot 10^{-16} \text{ m}^2/\text{s}$, M : $7.3 \cdot 10^{-12} \text{ m.mol}/(\text{J.s})$, $A=1$, $P=1$, Interface=Semi-Coherent.

CHAPTER 6

RATE CAPABILITY ANALYSIS

From Chapter 2, it is evident that the increase in rate capability achieved for LiFePO₄ has been attributed to factors such as increase in electronic conductivity, Li-ion conductivity, rate of phase transformation, solid solution range, and reduction in particle size. Although there has been large improvement in the rate capability of LiFePO₄, the actual reason behind the improvement and how these factors affect the rate capability are not clear. Here, an effort made is to determine the influence of these factors on rate capability of LiFePO₄ from the modified SCM-1 and the modified SCM-2.

6.1 Effect of Lithium Chemical Diffusion in β Phase and Interface Mobility on Rate Capability

Range of β phase chemical diffusion coefficient (D_β):

As mentioned earlier, the lithium ion and the electron in LiFePO₄ form a dilute binary electrolyte [22]. Due to this reason, the chemical diffusion coefficient D (total lithium ion and electron) can be obtained by following equation [22]:

$$\hat{D} = \frac{2D_e D_i}{D_e + D_i} \quad (6.1)$$

where D_i and D_e are diffusion coefficients of Li⁺ ion and electron, respectively. Similarly, the total conductivity (σ) of lithium ion and electron, can be obtained based on the Nernst-Einstein equation [83],

$$\sigma = \frac{2\sigma_{Li}\sigma_e}{\sigma_{Li} + \sigma_e} \quad (6.2)$$

The total conductivity of LiFePO₄/A calculated from electronic conductivity (5×10^{-4} S/cm [32]) and ionic conductivity (1.5×10^{-5} S/cm [32]) is found to be 2.9×10^{-5} S/cm. Based on the relationship between conductivity and chemical diffusion coefficient of LiFePO₄ proposed by Whittingham et al. [83], the total chemical diffusion coefficient of LiFePO₄ is found to be 10^{-13} m²/s. This value is within the range between 10^{-11} – 10^{-13} m²/s determined from Mossbauer spectroscopy [84], although it is slightly lower than the calculated theoretical value of 10^{-11} m²/s [83] and much higher than the value of 10^{-18} m²/s determined from GITT [85], cyclic voltammetry [86], and EIS [85]. The low value for the chemical diffusion coefficient measured from EIS, GITT, and cyclic voltammetry is due to the slow phase transformation because the chemical diffusion coefficient measured here is actually an “effective” chemical diffusion coefficient, which is influenced by phase transformation. EIS, GITT, and CV for the measurement of the chemical diffusion coefficient are proven to be valid only for solid solution reactions [85]. To investigate the effects of β phase chemical diffusion coefficient on the discharge kinetics of LiFePO₄, the range for β phase chemical diffusion coefficient for our simulations is chosen to be in between 5×10^{-17} m²/s 3.2×10^{-13} m²/s, and these values covered almost the entire range of data reported in the literature.

Range of interface mobility (M):

The range of M values used in this simulation for LiFePO₄ is determined by comparing the phase transformation in LiFePO₄ with the phase transformation in Ti-alloy

and steel at 720°C; this has been well-studied using mixed-control model [71]. Sietsma et al. reported M value of 10^{-12} m.mol/(Js) for Ti-alloys and 10^{-9} m.mol/(Js) for steel [71]. Since the phase transformation rate of LiFePO₄ under potential-step chronoamperometry (PSCA) at room temperature [54] lies between the phase transformation of Ti-alloy and steel at 720°C [71], the interface mobility range in between 3×10^{-12} – 1.3×10^{-8} m. mol/(J.s) is considered for the simulation.

Rate Capability vs. M and D_β:

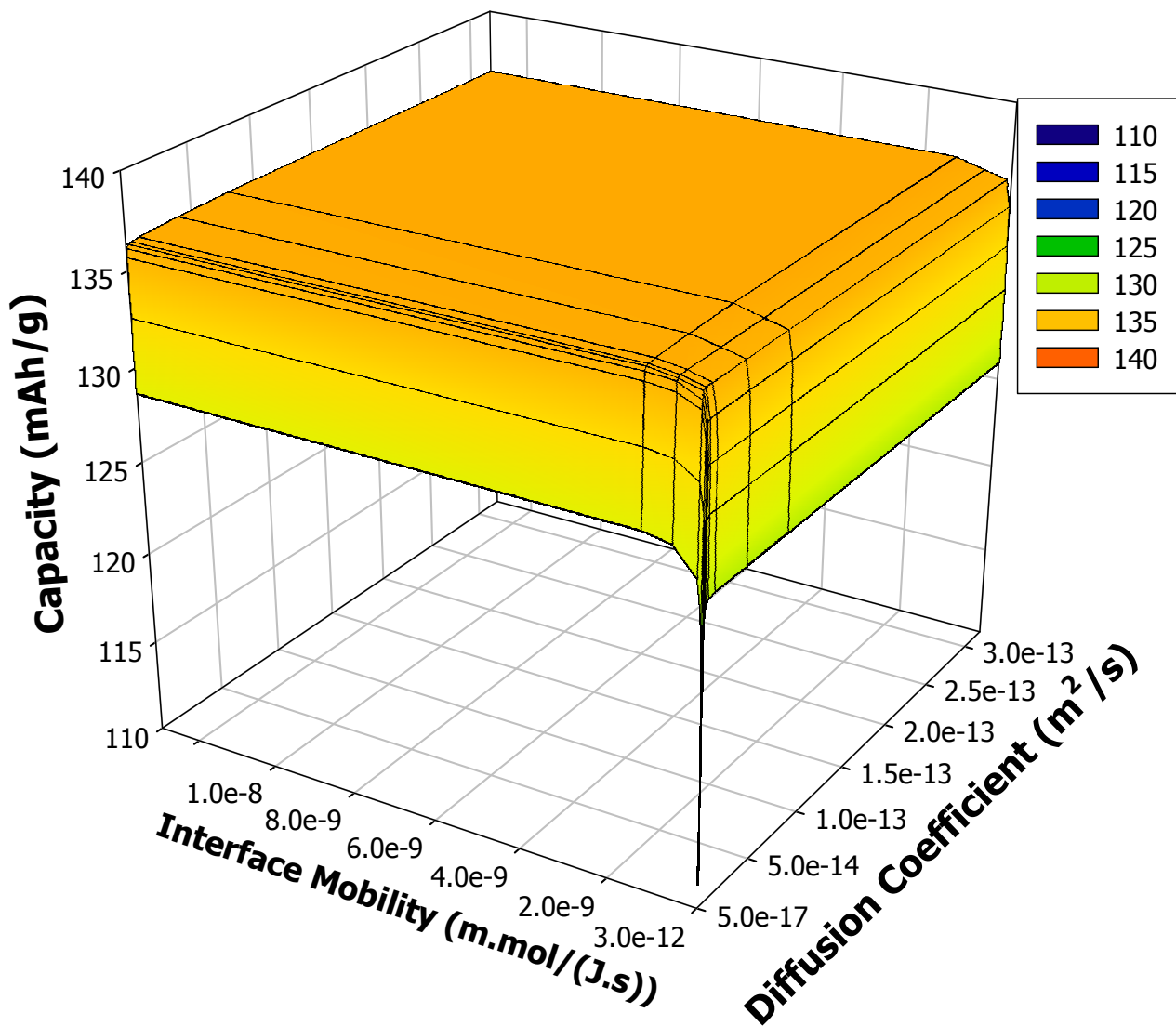
To determine the effect of chemical diffusion in β phase and interface mobility on rate capability, the discharge capacities of LiFePO₄ at 0.1C, 5C and 10C, and at different values of D_β and M are obtained by using the modified SCM-1. The values of the parameters other than D_β and M are assumed to have the same value as that of sample A (Table 5.1). The value of the parameter D_β is changed from 5×10^{-17} m²/s to 3.2×10^{-13} m²/s and at each value of the parameter D_β, the value of the parameter M is changed from 3×10^{-12} to 1.3×10^{-8} m mol/(J.s)). At each value of D_β and M, the discharge capacities at 0.1C, 5C and 10C are determined from the modified SCM-1. From the discharge capacities at 0.1C, 5C and 10C, discharge rate capability at 5C (ratio of the discharge capacity at 5C to the discharge capacity at 0.1C) and discharge rate capability at 10C (ratio of the discharge capacity at 10C to the discharge capacity at 0.1C) are calculated. Figure 6.1 shows 3-D graphs for the discharge capacity at 0.1C and 5C as a function of interface mobility and β phase chemical diffusion coefficient. Figures 6.2 and 6.3 show the contour plots for rate capability at 5C and 10C as a function of M and D_β. From

Figures 6.1, 6.2, and 6.3, the results for a micron-sized LiFePO₄ particle with $C_{\beta\alpha}$ equivalent to 0.77 can be summarized as follows:

- When D_{β} is lower than 5×10^{-16} m²/s, discharge capacity at lower currents such as 0.1C start to decrease (Figure 6.1a). As a result, D_{β} higher than 5×10^{-16} m²/s is required for achieving high discharge capacity at low currents.
- When D_{β} is lower than 2×10^{-15} m²/s, a rapid decrease in discharge capacity at 5C is observed (Figure 6.1 b). When M is lower than 1.3×10^{-11} m mol/(J.s), a moderate decrease in discharge capacity at 0.1C (Figure 6.1 a) and a large decrease in discharge capacity at 5C is observed (Figure 6.1 b). Hence, to achieve a high discharge capacity at low currents and a high rate capability at high currents, the value of D_{β} should be higher than 2×10^{-15} m²/s, and the value of M should be higher than 1.3×10^{-11} m mol/(J.s).
- When D_{β} is lower than 2×10^{-15} m²/s, the interface mobility does not have much influence on the rate capability at 5C (Figure 6.2) and rate capability at 10C (Figure 6.3), i.e. the discharge process at 5C and 10C is controlled by diffusion.
- When M is lower than 1.3×10^{-11} m.mol/(J.s), the chemical diffusion coefficient in β phase does not have much influence on the rate capability at 5C (Figure 6.2) and rate capability at 10C (Figure 6.3), i.e. the discharge process at 5C and 10C is controlled by interface mobility.
- Based on the estimated values of chemical diffusion coefficient and interface mobility, positions of sample A and sample B are marked on the rate capability contour plot (Figure 6.2). From Figure 6.2, it is clear that the rate capability at 5C for sample A can only be improved by increasing the interface mobility, which

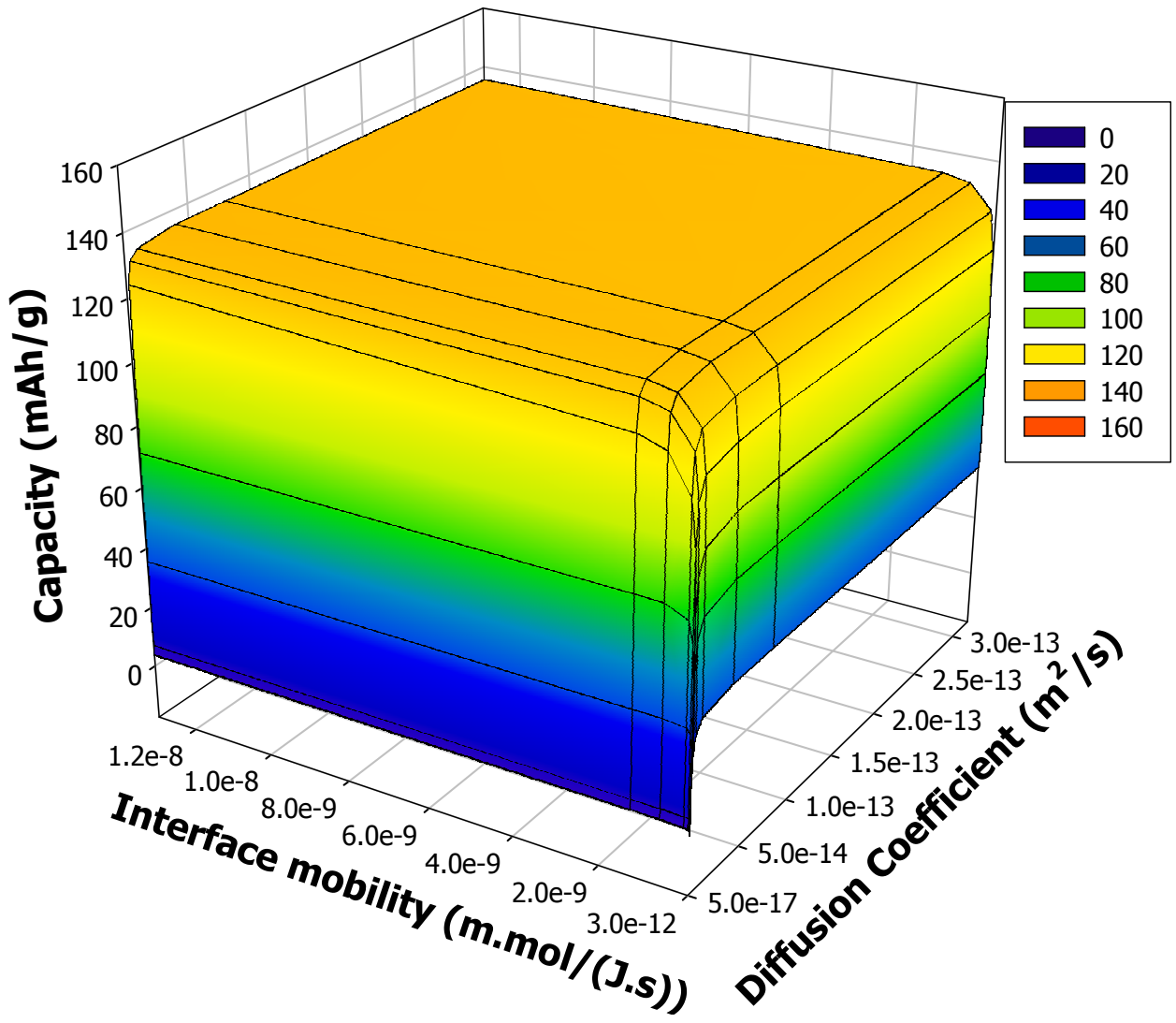
implies that discharge process at 5C is controlled by the interface mobility. Similar conclusions can be drawn for rate capability of sample B at 5C (Figure 6.2) and 10C (Figure 6.3). The higher rate performance of Sample B than that of sample A is mainly due to fast interface mobility with slight contribution from the improved chemical diffusion coefficient.

- Contour plots shown in Figures 6.2 and 6.3 are extremely useful, as they show the required β phase chemical diffusion coefficient and interface mobility values for achieving the desired rate capability. For example, in order to achieve 80% or higher rate capability at 5C, β phase chemical diffusion coefficient should be higher than $2 \times 10^{-15} \text{ m}^2/\text{s}$ and interface mobility should be higher than $3.9 \times 10^{-11} \text{ m mol}/(\text{J.s})$ (Figure 6.2). Similarly, in order to achieve 80% or higher rate capability at 10C, β phase chemical diffusion coefficient should be higher than $4 \times 10^{-15} \text{ m}^2/\text{s}$ and interface mobility should be higher than $3.9 \times 10^{-11} \text{ m mol}/(\text{J.s})$ (Figure 6.3).
- The same rate capability can be achieved at different values of the β phase chemical diffusion coefficient and interface mobility (Figures 6.2 and 6.3).



(a)

Figure 6.1: Simulated discharge capacity of LiFePO_4 at different currents as a function of Interface Mobility and β phase chemical diffusion coefficient (a: 0.1C, b:5.0C)



(b)

Figure 6.1: Continued

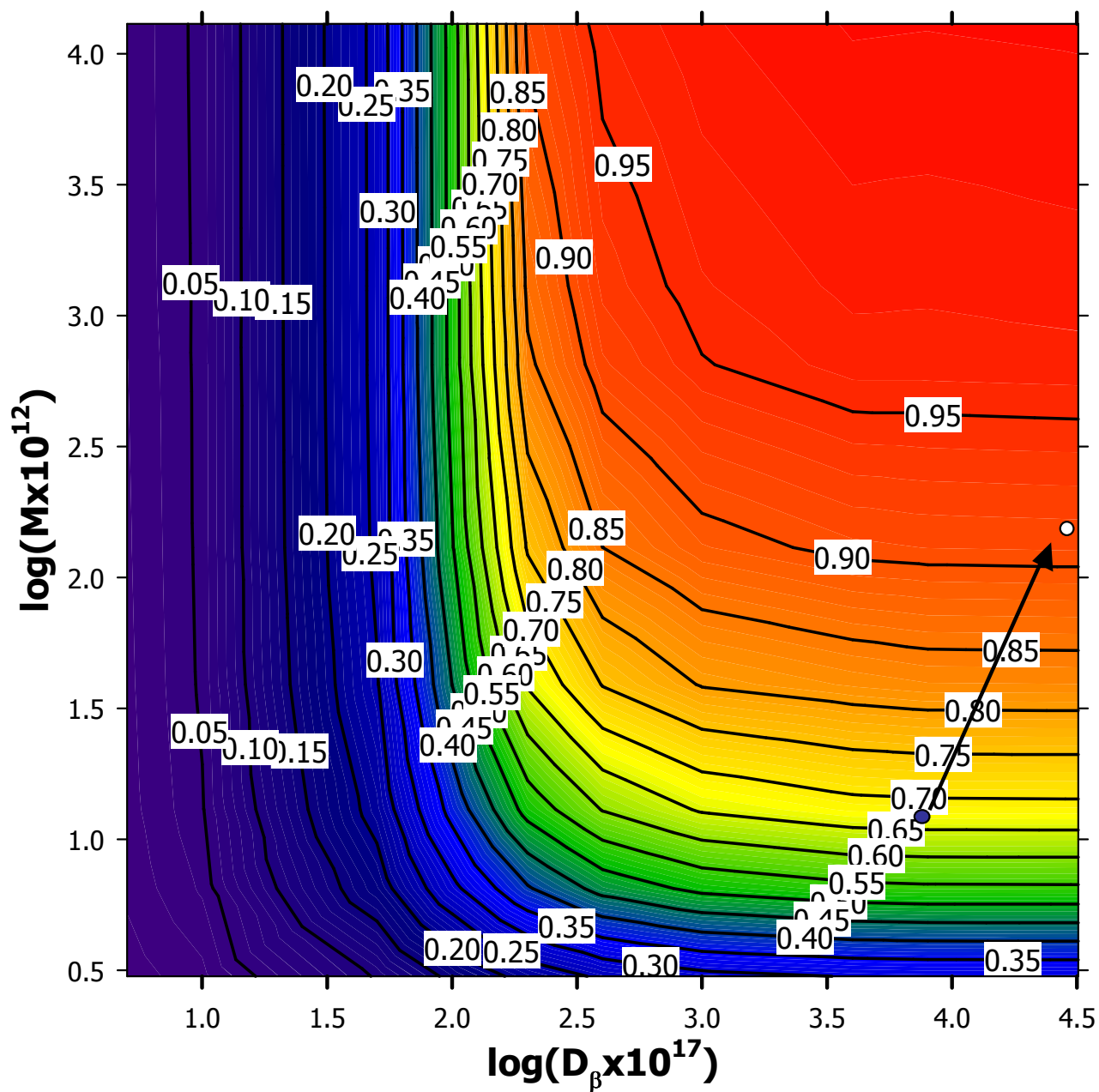


Figure 6.2: Contour plot for ratio of discharge capacity (simulated) at 5C to discharge capacity (simulated) at 0.1C for LiFePO₄ as a function of interface mobility and β phase chemical diffusion coefficient. The capacity ratio at 5C to 0.1C for Sample A (blue circle) and Sample B (white circle) are also shown for comparison

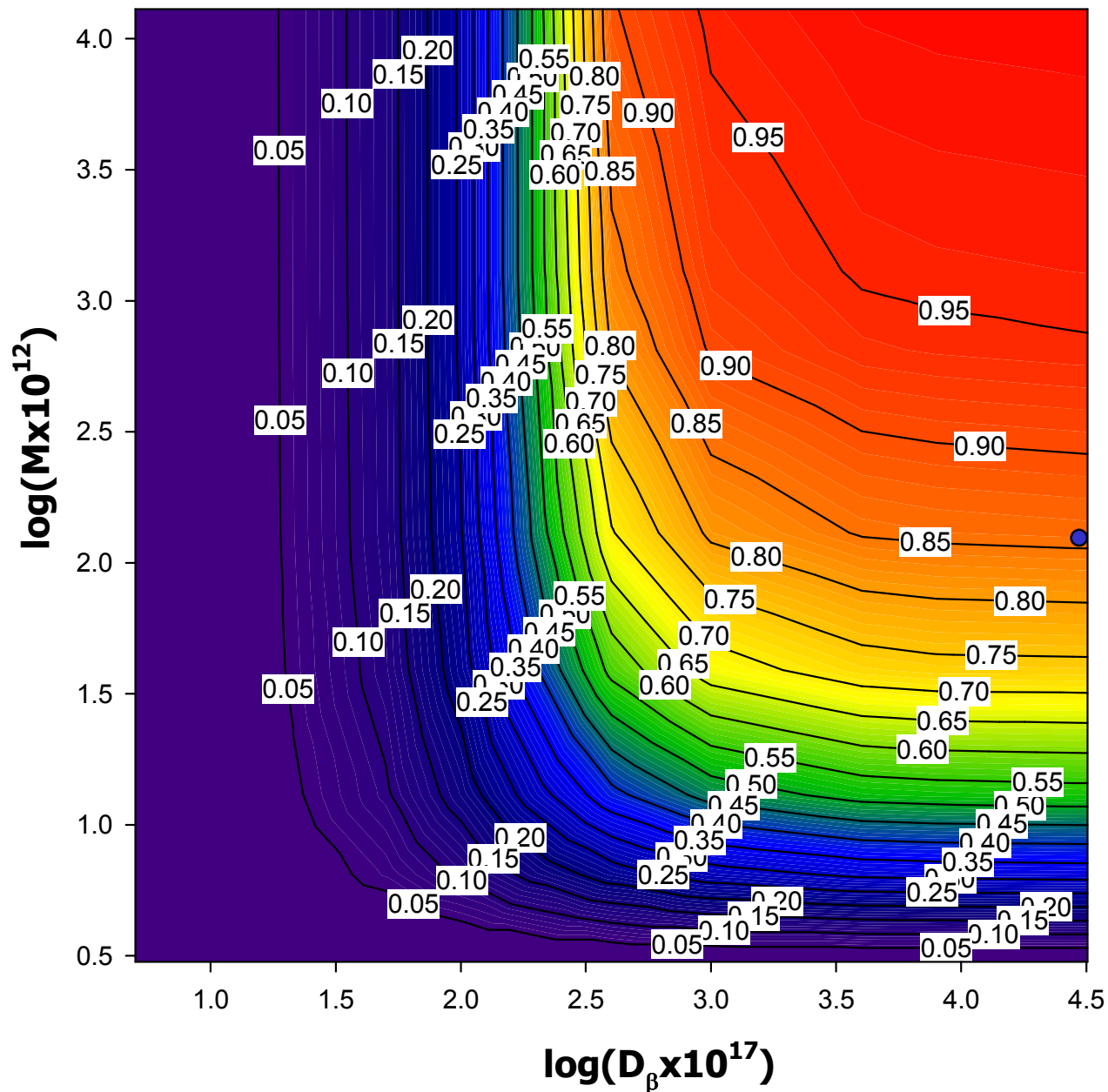


Figure 6.3: Contour plot for ratio of discharge capacity (simulated) at 10C to discharge capacity (simulated) at 0.1C for LiFePO_4 as a function of interface mobility and β phase chemical diffusion coefficient. The capacity ratio at 10C to 0.1 C for Sample B (blue circle) is also shown.

6.2 Effect of Solid Solution Range on Rate Capability

The results recently reported [24-28] suggest that the doping/substitution affects the α and the β solid solutions ranges, which largely changed the rate performance of LiFePO_4 . In order to get a broader understanding on the relation between the solid solution and the rate capability, we investigated the effects of increasing the α solid solution alone, increasing the β solid solution alone and increasing both α and β solid solutions simultaneously on the discharge behavior and rate capability. The effect of extending the β solid solution alone on rate capability is analyzed using the modified SCM-1. The effect of increasing the α solid solution alone on the rate capability and the effect of increasing both α and β solid solutions simultaneously on the rate capability are analyzed using modified SCM-2.

Generally, the increase in solid solution range in LiFePO_4 will reduce the crystallographic mismatch due to a small concentration difference between $\theta_{\alpha\beta}$ and $\theta_{\beta\alpha}$. The decrease in the crystallographic mismatch may change the nature of the interface from incoherent to semi-coherent, and even to coherent. It will also change the accommodation energy, which can be captured in the model by the variation of the accommodation energy factor A and $f(x_C(t))$ (Eqs. 5.19, 5.20a, and 5.20b). In order to simplify the calculation, it is assumed that the interface maintains its state (semi-coherent) during the change in solid solution region and that the accommodation energy decreases linearly with the decrease in concentration range. Changing the solid solution range means to change the equilibrium concentrations of Li deficient (α) and Li rich (β) phases. This is also evident from looking at the equilibrium potential curves of sample AC

LiFePO₄ and sample NC LiFePO₄ [24-26]. Throughout this analysis, the maximum lithium that can be incorporated into the FePO₄ lattice (C_t) is assumed to remain constant with the doping/substitution.

6.2.1 Effect of β phase Solid Solution Range and β Phase Chemical Diffusion

Coefficient on Rate Capability

The influence of β phase solid solution range on rate capability of LiFePO₄ is determined by decreasing the value of the parameter $\theta_{\beta\alpha}$ in the modified SCM-1 from 0.77 to 0.1, i.e. from a phase change material to a complete solid solution material. With the change in $\theta_{\beta\alpha}$, the accommodation energy is decreased. This is done by decreasing the value of the parameter A linearly with the change in $\theta_{\beta\alpha}$ (the value of the parameter A is taken as the ratio of $\theta_{\beta\alpha}$ to 0.77). With the change in $\theta_{\beta\alpha}$, the equilibrium potential curves are also changed by changing the coefficients in Eq. 4.1. The change in $\theta_{\beta\alpha}$ will also increase the chemical diffusion rate in β phase due to a high concentration difference in the β phase (Figure 5.1). Hence, at each value of $\theta_{\beta\alpha}$, the value of D_β is changed in steps from 5×10^{-17} to 3.2×10^{-13} m²/s and discharge capacities at 0.1C, 5C, and 10C are calculated. In these simulations, the parameters other than A , $\theta_{\beta\alpha}$, and D_β are assumed to have the values same as that of sample A. Figure 6.4 shows the equilibrium potential curves obtained from Eq. 4.1, which correspond to $\theta_{\beta\alpha}$ values of 0.77, 0.63, 0.49, 0.39, 0.30, 0.20, and 0.10, respectively. Figure 6.5 shows 3-D graphs for the discharge capacity at 0.1C and 5C obtained from the model as a function of the β phase solid solution range

($\theta_{\beta\alpha}$) and β phase chemical diffusion coefficient (D_{β}). Figures 6.6 and 6.7 show the contour plots of rate capability at 5C and 10C as a function of $\theta_{\beta\alpha}$ and D_{β} for Sample A.

The discharge behavior of a micron sized LiFePO_4 particle with an interface mobility of 1.3×10^{-11} m.mol/(J.s), with different β phase solid solution ranges and β phase chemical diffusion coefficient values can be summarized as follows:

- Irrespective of the value of D_{β} , increase in discharge capacity at 0.1C (Figure 6.5a) and rate capability (Figures 6.5b, 6.6, and 6.7) are observed with the increase in solid solution range from $\theta_{\beta\alpha} = 0.77$ to $\theta_{\beta\alpha} = 0.5$, which is consistent with the experimental results reported by Chiang et al. [24,25,26].
- Interestingly, the discharge capacity at 0.1C (Figure 6.5a) begins to decrease when the electrode material has more than 50% solid solution. Similarly, the rate capability at 5C is found to decrease when the electrode material has more than 70% solid solution material (Figure 6.6). This behavior becomes more pronounced at 10C (Figure 6.7). The phase transformation during discharge of LiFePO_4 has two opposite effects on the discharge rate. On one hand, it induces concentration partitioning at the phase boundary, which results in faster lithium insertion rate compared to pure lithium chemical diffusion. On the other hand, the accommodation energy induced by the concentration difference between two phases decreases the phase transformation rate. Therefore, there exists an optimal solid solution range (Figures 6.6 and 6.7) where the discharge capacity and rate capability reach the highest.

- To achieve 80% rate capability at 5C (Figure 6.6), micron size LiFePO_4 with an interface mobility of 1.3×10^{-11} m.mol/(J.s) should have more than 27% solid solution.
- The same rate capability can be achieved at different solid solution ranges and different chemical diffusion coefficient values. But, the highest rate capability and discharge capacity is possible for materials with 50% solid solution range, though the chemical diffusion coefficient values are low (Figure 6.6).

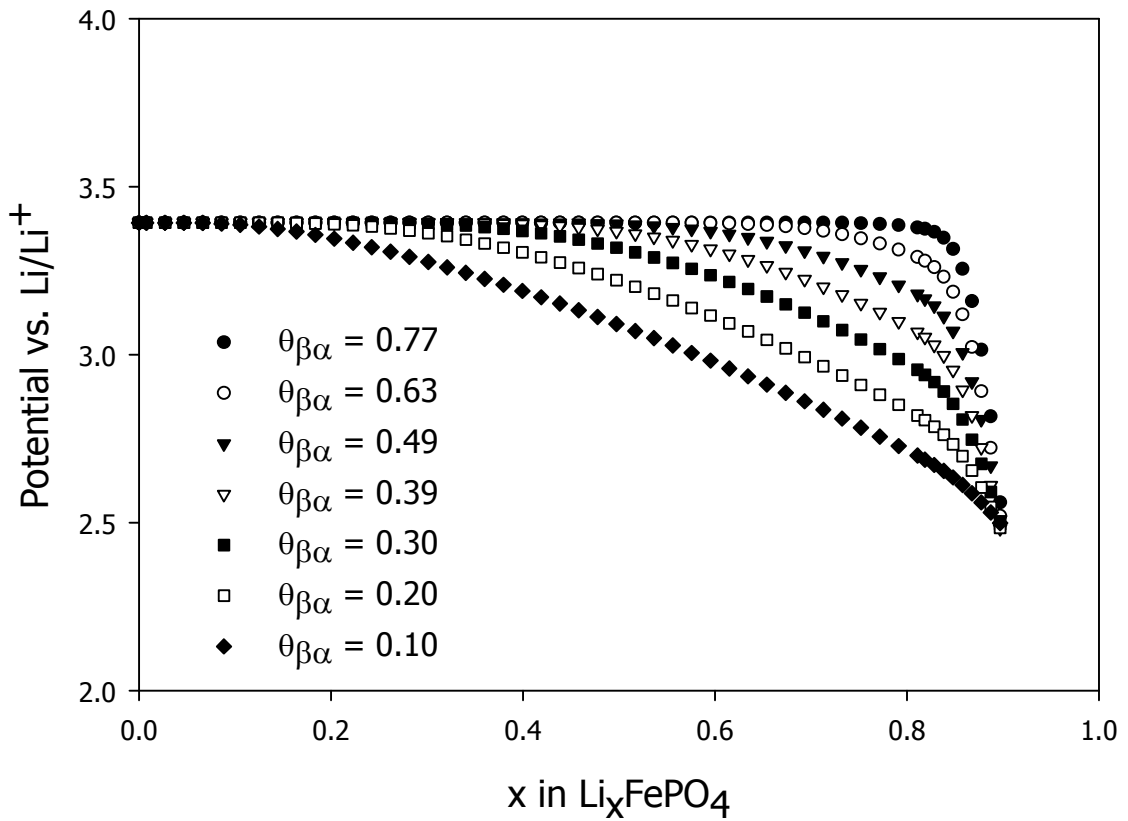
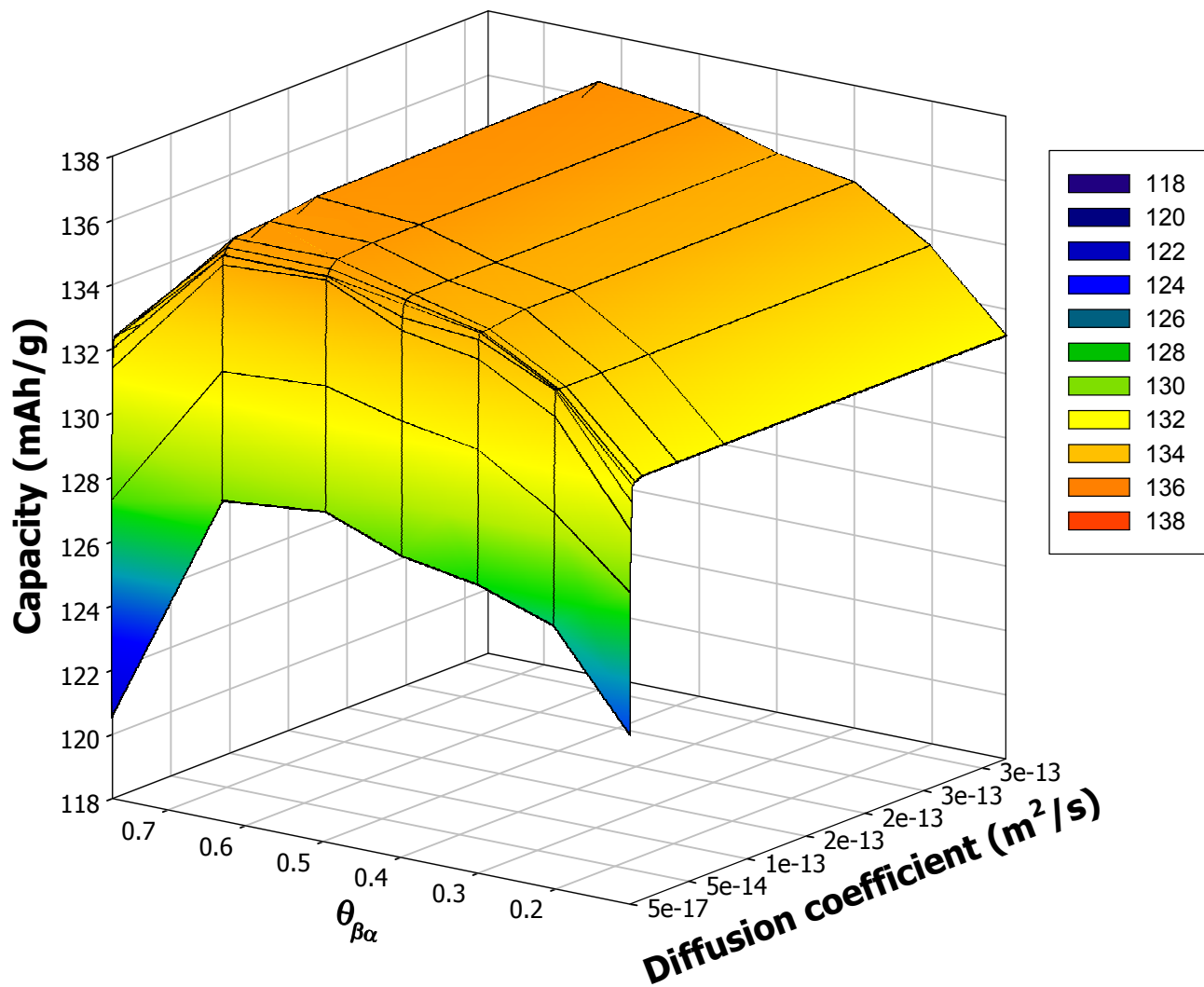
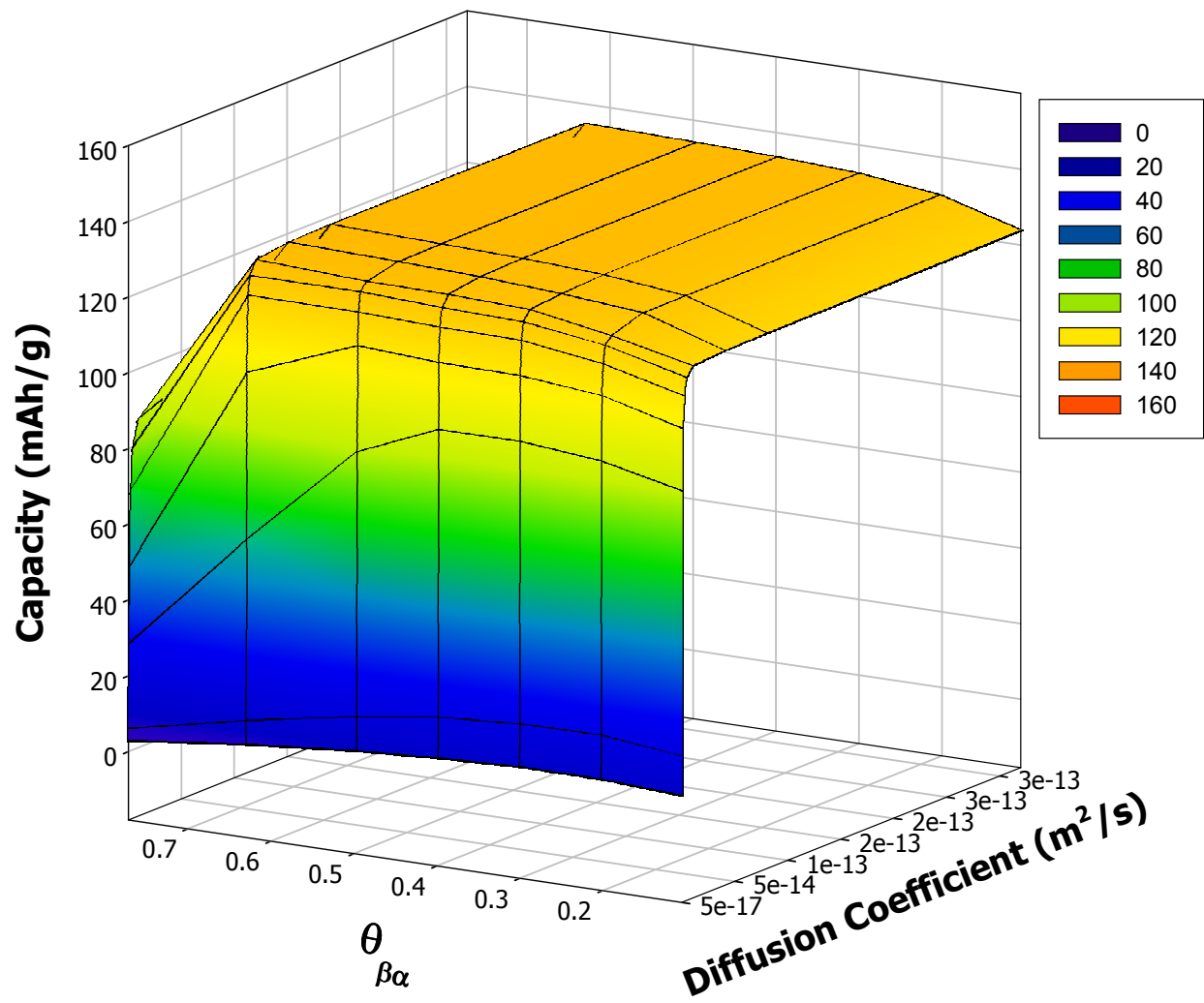


Figure 6.4: Equilibrium Potential Curves (obtained from Eq. 4.1 with different coefficients) for LiFePO_4 with different β phase solid solution range as a function of Li content in FePO_4 during discharge process.



(a)

Figure 6.5: Simulated discharge Capacity of LiFePO₄ at different Currents as a function of β phase Solid Solution Range and β phase chemical diffusion coefficient (a: 0.1C, b:5.0C)



(b)

Figure 6.5: Continued

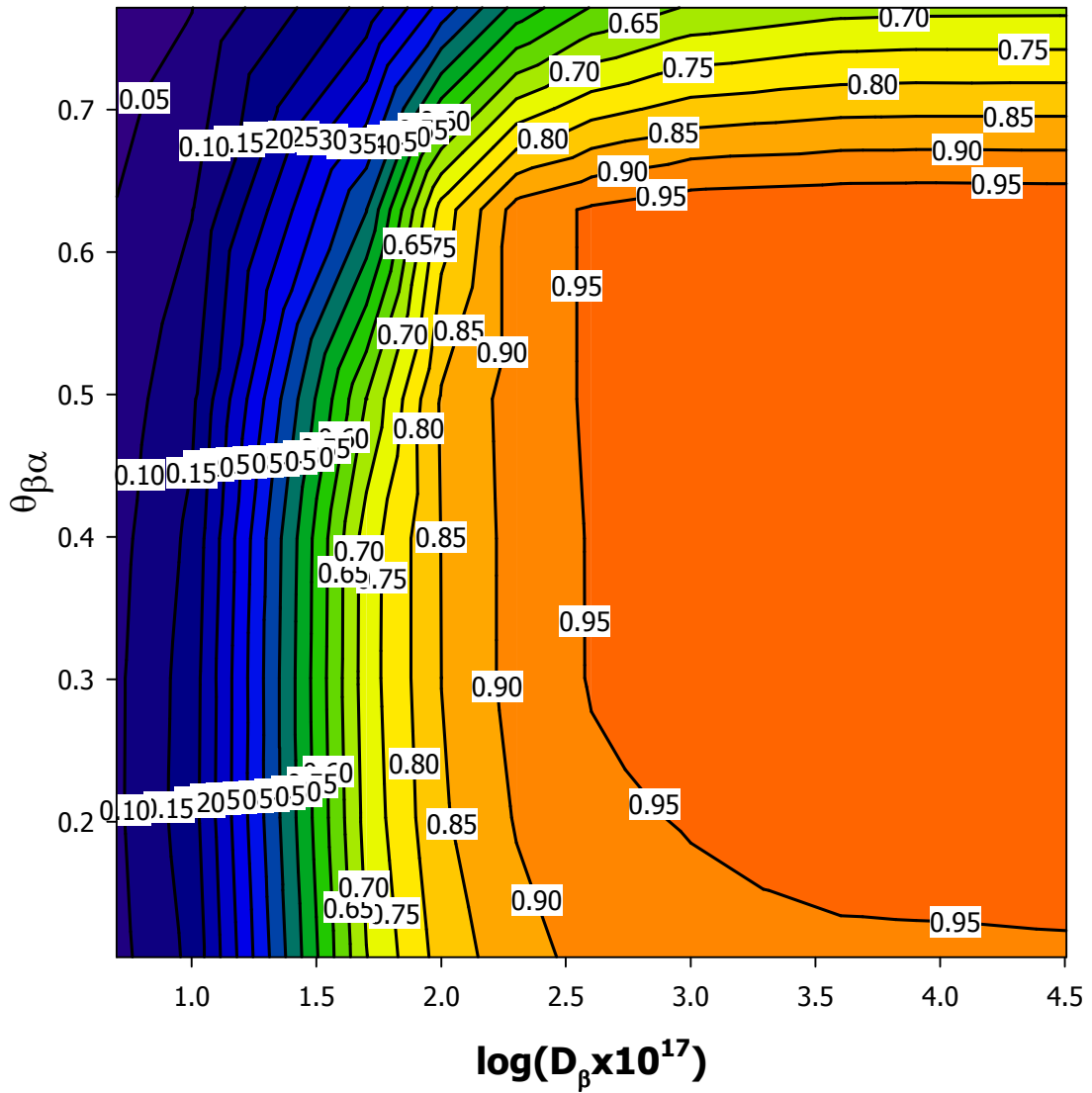


Figure 6.6: Contour plot for ratio of discharge capacity (simulated) at 5C to discharge capacity (simulated) at 0.1C for LiFePO₄ as a function of β phase chemical diffusion coefficient and β phase solid solution range.

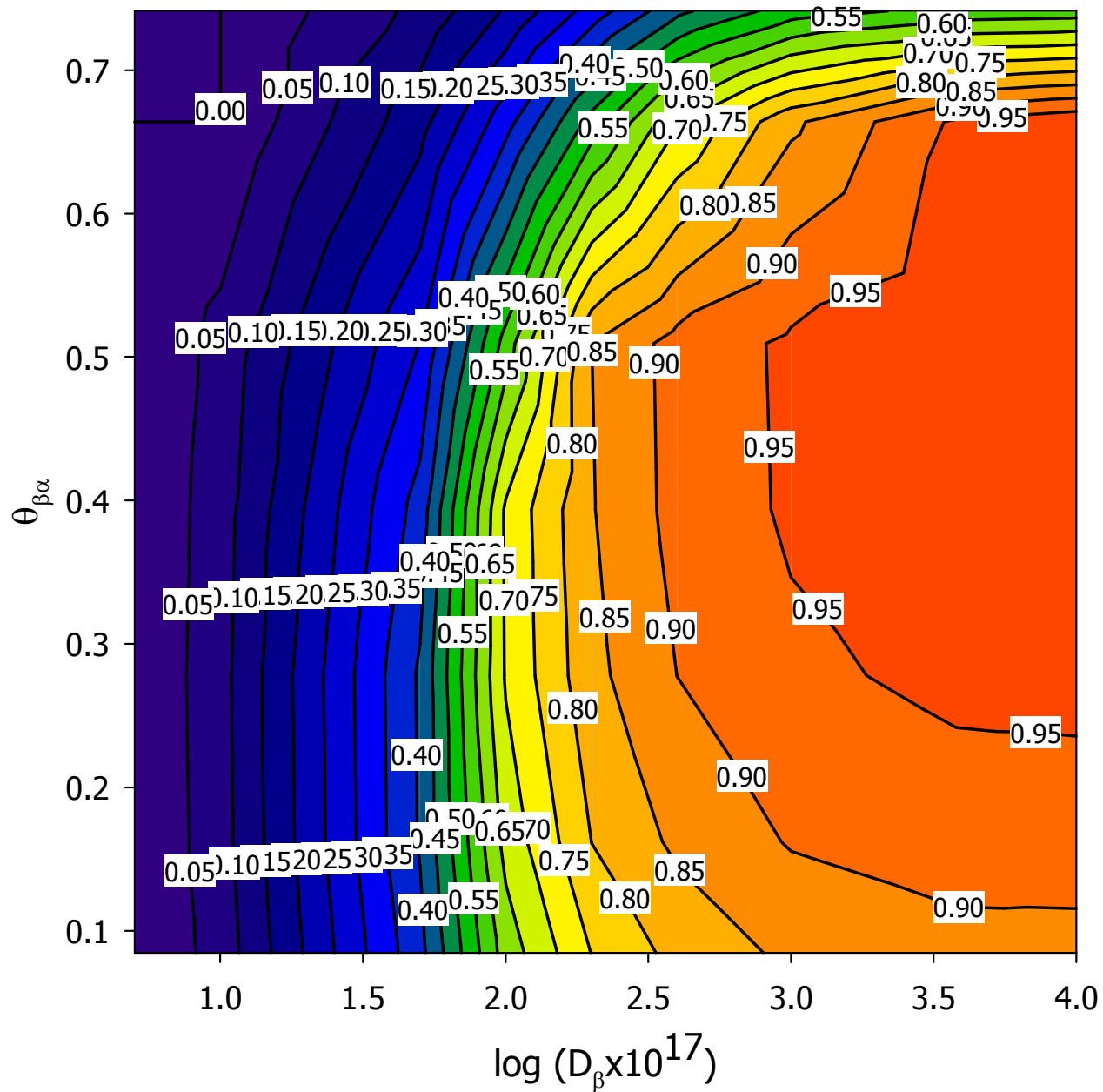


Figure 6.7: Contour plot for ratio of discharge capacity (simulated) at 10C to discharge capacity (simulated) at 0.1C for LiFePO₄ as a function of β phase chemical diffusion coefficient and β phase solid solution range.

6.2.2 Effect of Extending the α Solid Solution Range on Rate Capability

The effect of increasing the α solid solution range of LiFePO_4 on the rate performance is determined by increasing the $\theta_{\alpha\beta}$ from 0.015 to 0.4 (while keeping $\theta_{\beta\alpha}$ constant) in the modified SCM-2, i.e. from a phase change material to a large solid solution material. With the change in $\theta_{\alpha\beta}$, the value of the parameter A is changed (the value of parameter A was taken as the ratio of $(\theta_{\beta\alpha}-\theta_{\alpha\beta})$ to $(0.77-0.015)$). With the change in $\theta_{\alpha\beta}$, the equilibrium potential curves are also changed by changing the coefficients in Eq. 5.58. Using the modified SCM-2, the discharge behaviors of LiFePO_4 with different α solid solution limits at current densities of 5C, 10C, and 20C are simulated. Throughout these simulations, the parameters other than $\theta_{\alpha\beta}$ and A are assumed to have the same values as that of sample A (Table 5.2). Also, it is assumed that changing the α solid solution range does not change the chemical diffusion coefficients in α and β phases (D_α , D_β) and the interface mobility (M). Figure 6.8 shows the equilibrium potential curves obtained from Eq. 5.58, which correspond to $\theta_{\alpha\beta}$ values of 0.015, 0.1, 0.15, 0.2, 0.25, 0.30, 0.35, and 0.4, respectively. The discharge curves of LiFePO_4 with different α solid solution limits at 5C, 10C, and 20C are shown in Figures 6.9 and 6.10. The discharge capacity of LiFePO_4 seems to increase monotonically with the increase in α solid solution irrespective of discharge current used. However, at lower currents up to 5C (Figure 6.9), the discharge capacity reaches the maximum value with small increase in $\theta_{\alpha\beta}$ and remains constant with further increase in $\theta_{\alpha\beta}$. At higher currents such as 20C (Figure 6.10), a constant increase in the discharge capacity is observed with the increase

in $\theta_{\alpha\beta}$. From these results, it can be suggested that the cathode materials with higher α solid solution exhibit higher rate capability than the materials with lower α solid solution, provided that the chemical diffusion coefficients and interface mobility are not lowered with the increase in α solid solution.

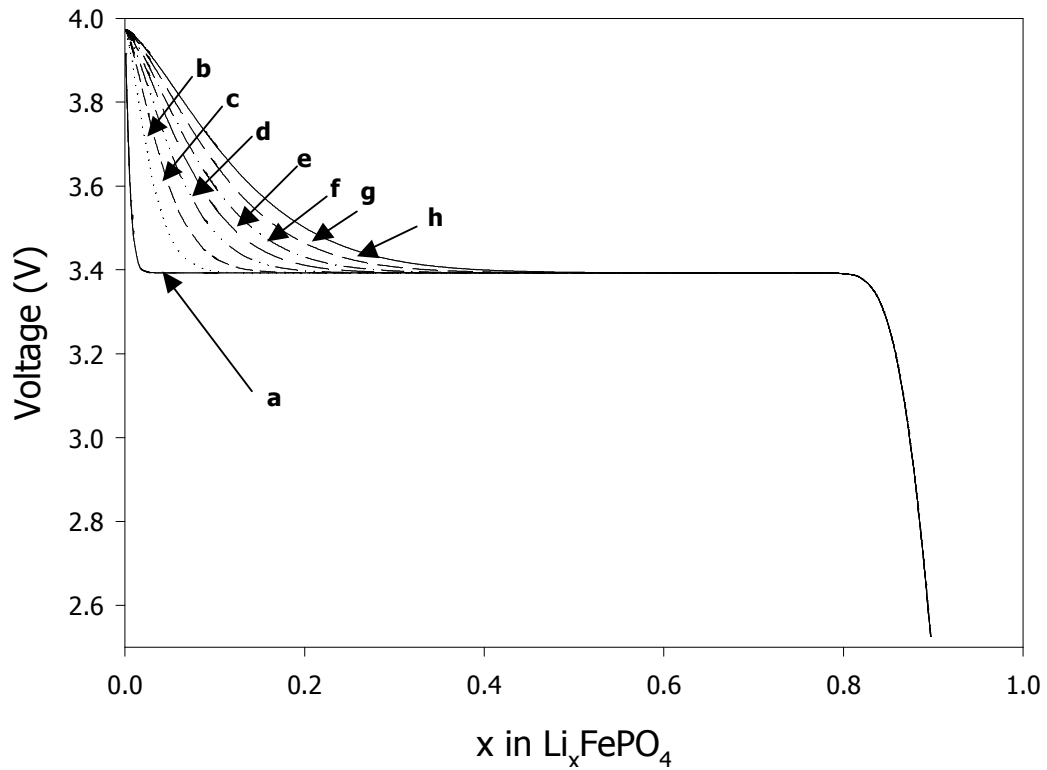


Figure 6.8: Equilibrium Potential Curves (obtained from Eq [25] with different coefficients) for LiFePO_4 with different α solid solution range (different $\theta_{\alpha\beta}$ and $\theta_{\beta\alpha}=0.77$) as a function of Li content in FePO_4 during discharge process ($\theta_{\alpha\beta} = \text{a:}0.015, \text{b:}0.1, \text{c:}0.15, \text{d:}0.2, \text{e:}0.25, \text{f:}0.3, \text{g:}0.35, \text{h:}0.4$)

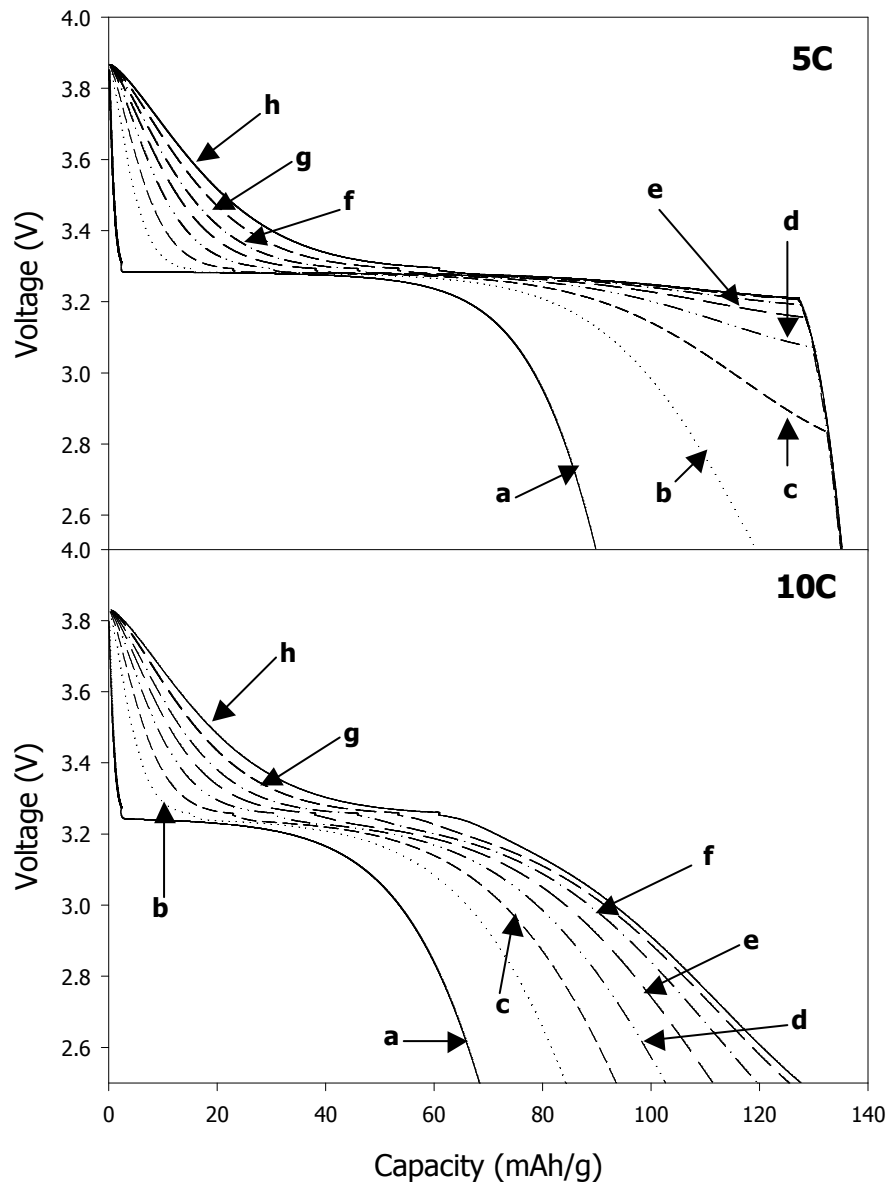


Figure 6.9: Discharge curves of LiFePO_4 with different α solid solution limits ($\theta_{\alpha\beta} = \text{a:}0.015, \text{b:}0.1, \text{c:}0.15, \text{d:}0.2, \text{e:}0.25, \text{f:}0.3, \text{g:}0.35, \text{h:}0.4$) at 5C and 10C

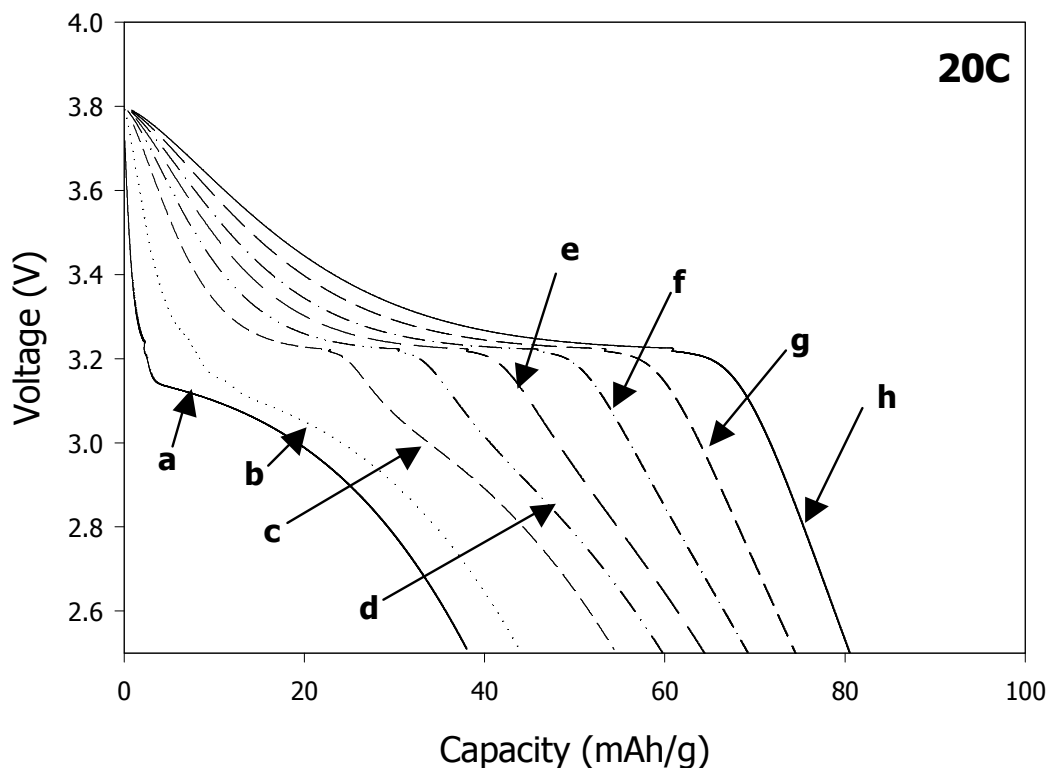


Figure 6.10: Discharge curves of LiFePO_4 with different α solid solution limits ($\theta_{\alpha\beta} = \text{a:}0.015, \text{b:}0.1, \text{c:}0.15, \text{d:}0.2, \text{e:}0.25, \text{f:}0.3, \text{g:}0.35, \text{h:}0.4$) at 20C

6.2.3 Effect of Extending the α and β Solid Solutions Simultaneously on Rate Capability

The effect of increasing α and β solid solutions of LiFePO_4 simultaneously on the rate performance is determined by increasing the $\theta_{\alpha\beta}$ from 0.015 to 0.35 while changing $\theta_{\beta\alpha}$ from 0.77 to 0.45 in the modified SCM-2, i.e. from a phase change material to a solid solution material. With the change in $\theta_{\alpha\beta}$ and $\theta_{\beta\alpha}$, the value of the parameter A is changed (the value of parameter A was taken as the ratio of $(\theta_{\beta\alpha} - \theta_{\alpha\beta})$ to $(0.77 - 0.015)$).

With the change in $\theta_{\alpha\beta}$ and $\theta_{\beta\alpha}$, the equilibrium potential curves are also changed by changing the coefficients in Eq. 5.58. Using the modified SCM-2, the discharge behavior of LiFePO_4 with different α and β solid solution limits at current densities of 0.1C, 10C, and 20C are simulated. Throughout these simulations, the parameters other than $\theta_{\alpha\beta}$, $\theta_{\beta\alpha}$, and A are assumed to have the same values as that of sample A (Table 5.2). Also, it is assumed that changing the α and β solid solution ranges does not change the chemical diffusion coefficients in α and β phases (D_α , D_β) and the interface mobility (M). Figure 6.11 shows the equilibrium potential curves obtained from Eq. 5.58, with different values $\theta_{\alpha\beta}$ corresponding to 0.015, 0.1, 0.15, 0.2, 0.25, 0.30, 0.35, and $\theta_{\beta\alpha}$ corresponding to 0.77, 0.7, 0.65, 0.6, 0.55, 0.5, 0.45, respectively. Figures 6.12 and 6.13 show the discharge behavior of LiFePO_4 with different α and β solid solution limits at different current densities (0.1C, 10C, and 20C). The variation of discharge capacity at different C-rates with solid solution range is summarized in Figure 6.14a. At all the currents, the discharge capacity reaches the maximum value with small increase in the solid solution region and remains constant with further increase. From these results, it seems that increasing both the solid solutions simultaneously is more beneficial than increasing one of the solid solutions, as the former one leads to a higher rate capability. However, when the chemical diffusion coefficient in the β phase is lowered by 2 orders of magnitude ($8 \times 10^{-16} \text{ m}^2/\text{s}$), extending the solid solution range is found to enhance rate performance at low discharge rates as well as at high discharge rates (Figure 6.14b).

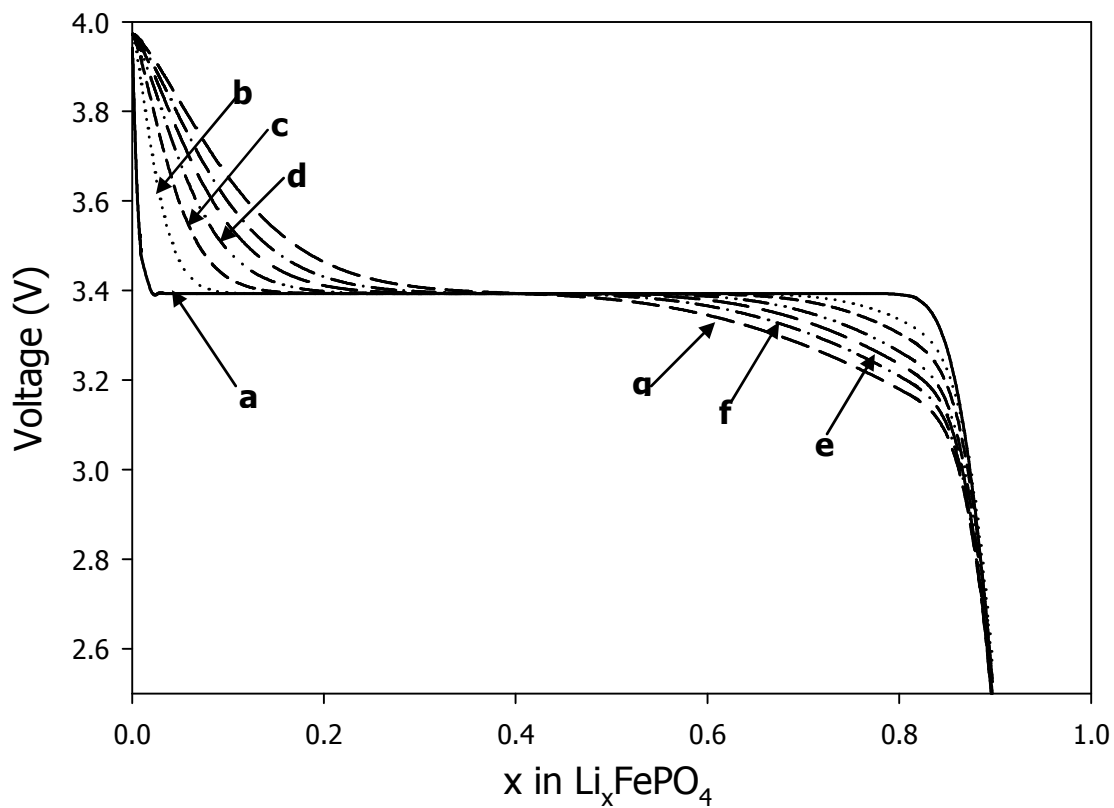


Figure 6.11: Equilibrium Potential Curves (obtained from Eq. 5.58 with different coefficients) for LiFePO_4 with different α and β solid solution ranges as a function of Li content in FePO_4 during discharge process ($\theta_{\alpha\beta}$ & $\theta_{\beta\alpha}$: a=0.015&0.77, b=0.1&0.7, c=0.15&0.65, d=0.2&0.6, e=0.25&0.55, f=0.3&0.5, g=0.35&0.45)

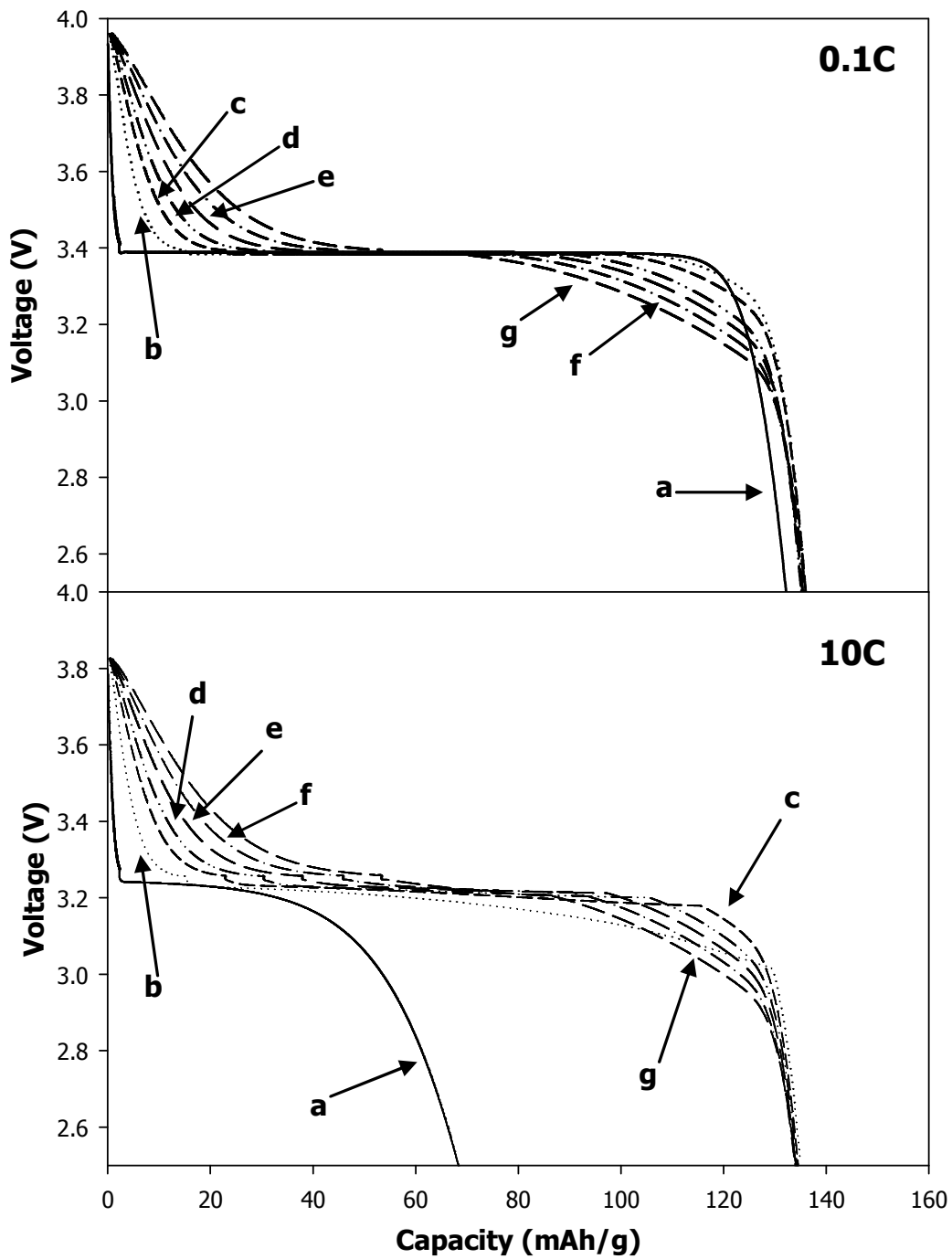


Figure 6.12: Discharge curves of LiFePO₄ with different α and β solid solution limits ($\theta_{\alpha\beta}$ & $\theta_{\beta\alpha}$: a=0.015&0.77, b=0.1&0.7, c=0.15&0.65, d=0.2&0.6, e=0.25&0.55, f=0.3&0.5, g=0.35&0.45) at 0.1C and 10C

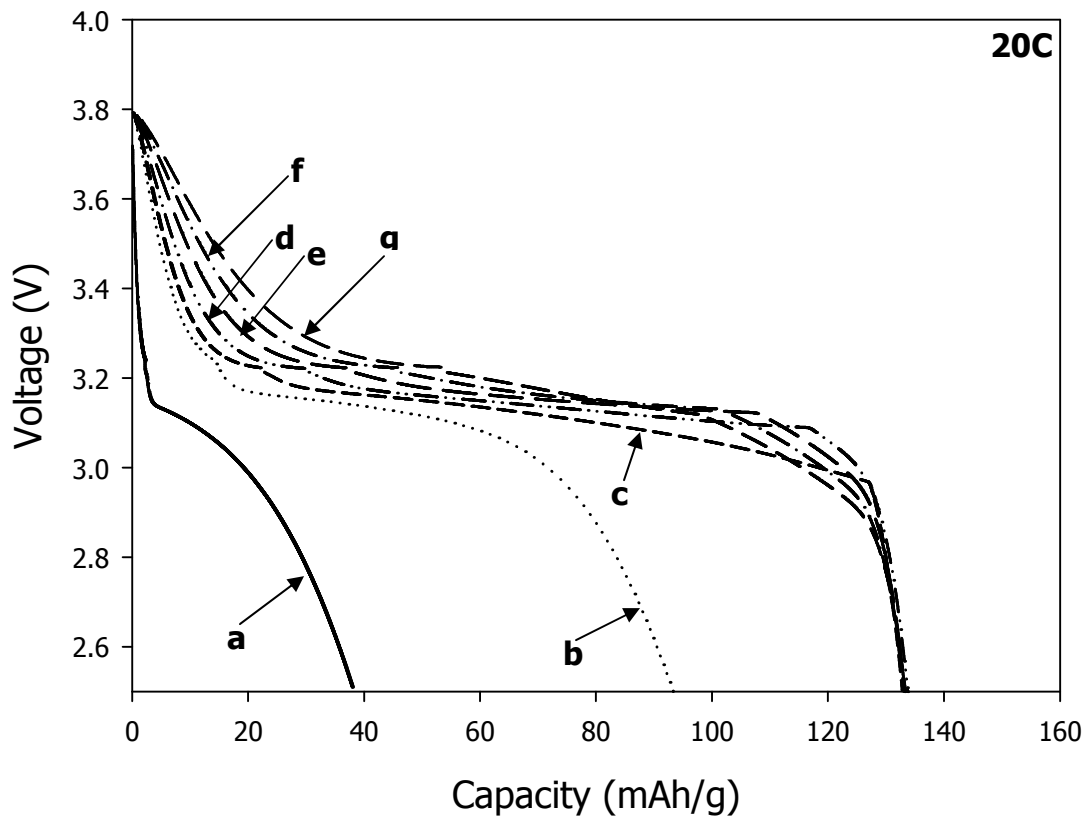


Figure 6.13: Discharge curves of LiFePO_4 with different α and β solid solution limits ($\theta_{\alpha\beta}$ & $\theta_{\beta\alpha}$: a=0.015&0.77, b=0.1&0.7, c=0.15&0.65, d=0.2&0.6, e=0.25&0.55, f=0.3&0.5, g=0.35&0.45) at 20C

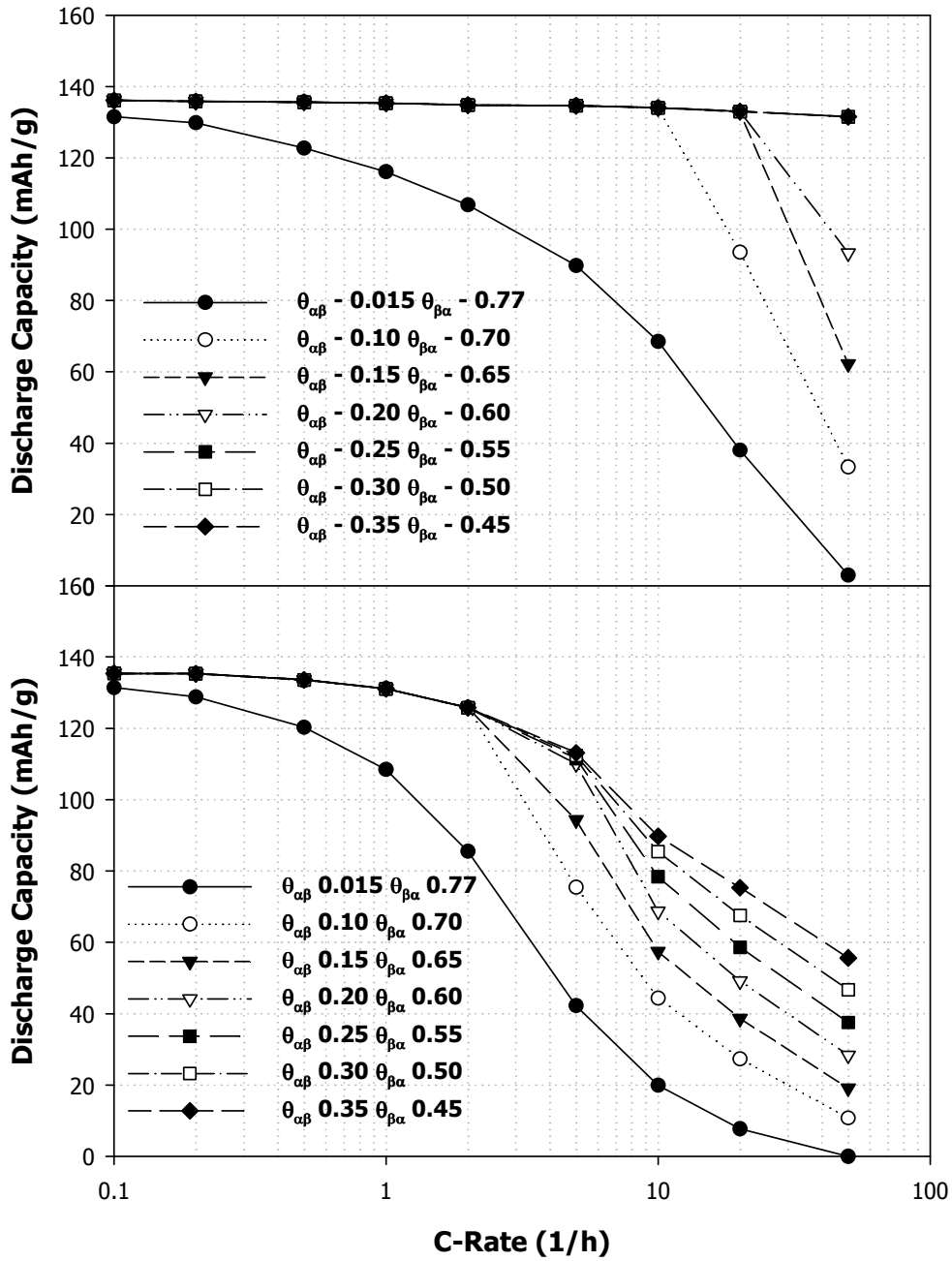


Figure 6.14: Effect of increasing α and β solid solutions on rate capability of LiFePO_4 with a chemical diffusion coefficient (D_β) of a: $8 \times 10^{-14} \text{ m}^2/\text{s}$, b: $8 \times 10^{-16} \text{ m}^2/\text{s}$.

6.3 Effect of Accommodation Energy on Rate Capability

Another possible method to improve the rate capability of LiFePO₄ electrode is to decrease the accommodation energy, while still maintaining a high solid solution range or high Li concentration difference between two phases in the phase transformation. For example, Li₄Ti₅O₁₂ exhibits a higher rate capability than LiFePO₄, in spite of a low solid solution range. This was attributed to a low volume change during the charge/discharge process [31], which in turn resulted in low accommodation energy. In order to investigate this phenomenon, the effect of accommodation energy on the rate performance of LiFePO₄ is studied by decreasing the values of the accommodation energy factor A in the modified SCM-1, while maintaining β phase chemical diffusion coefficient and interface mobility constant. Figure 6.15 shows the discharge capacity results at 10C current as a function of the parameter A , i.e. volume change/accommodation energy. From Figure 6.15, a large increase in discharge capacity is observed with the decrease in volume change. Therefore, the technology that can decrease volume change in the phase transformation of LiFePO₄ will enhance the rate performance.

Although Li₄Ti₅O₁₂ has a lower chemical diffusion coefficient (due to its low electronic conductivity) than that of LiFePO₄, Li₄Ti₅O₁₂ still has much high rate capability than that of LiFePO₄ due to zero volume change. To explore the effect of Li chemical diffusion coefficients on the rate capability of Li₄Ti₅O₁₂, the values of discharge capacity at 10C are calculated for different volume changes (A : 0.0-1.0) as well as at different β phase chemical diffusion coefficients (D_{β} : 5×10^{-17} – 3.2×10^{-13} m²/s), while keeping the other parameters constant (same as that of sample A) (Table 5.1). Figure 6.16

shows the discharge capacity at 10C as a function of volume change and β phase chemical diffusion coefficient. Except when the values of β phase chemical diffusion coefficient are lower than $5 \times 10^{-16} \text{ m}^2/\text{s}$, the rate performance is mainly controlled by the volume change rather than β phase chemical diffusion coefficient. Similarly, the values of discharge capacity at 10C are calculated for different volume changes (A: 0.5-1.0) as well as at different interface mobilities (3×10^{-12} - $1.3 \times 10^{-9} \text{ m.mol}/(\text{J.s})$), while keeping the other parameters constant (same as that of sample A)(Table 5.1). Figure 6.17 shows the discharge capacity at 10C as a function of volume change and interface mobility. Except when the value of interface mobility is lower than $6.5 \times 10^{-12} \text{ m.mol}/(\text{J.s})$, the rate performance is greatly improved by the reduction in volume change.

From these results, it is evident that the volume change plays a vital role in improving the rate capability, which can be readily observed from the high rate capability of $\text{Li}_4\text{Ti}_5\text{O}_{12}$. The low volume change occurring in $\text{Li}_4\text{Ti}_5\text{O}_{12}$ results in high interface mobility and rapid phase transformation rate, leading to the high rate capability.

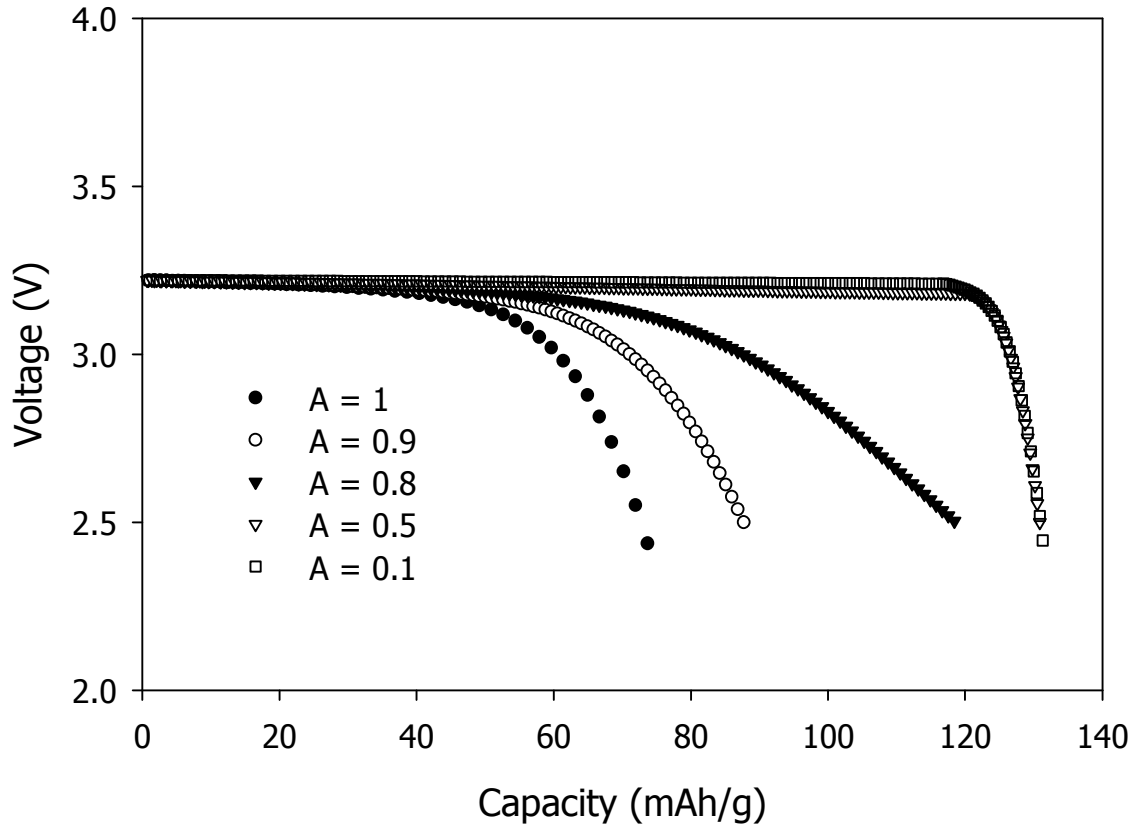


Figure 6.15: Effect of accommodation energy factor on discharge curves of LiFePO₄ at 10C current

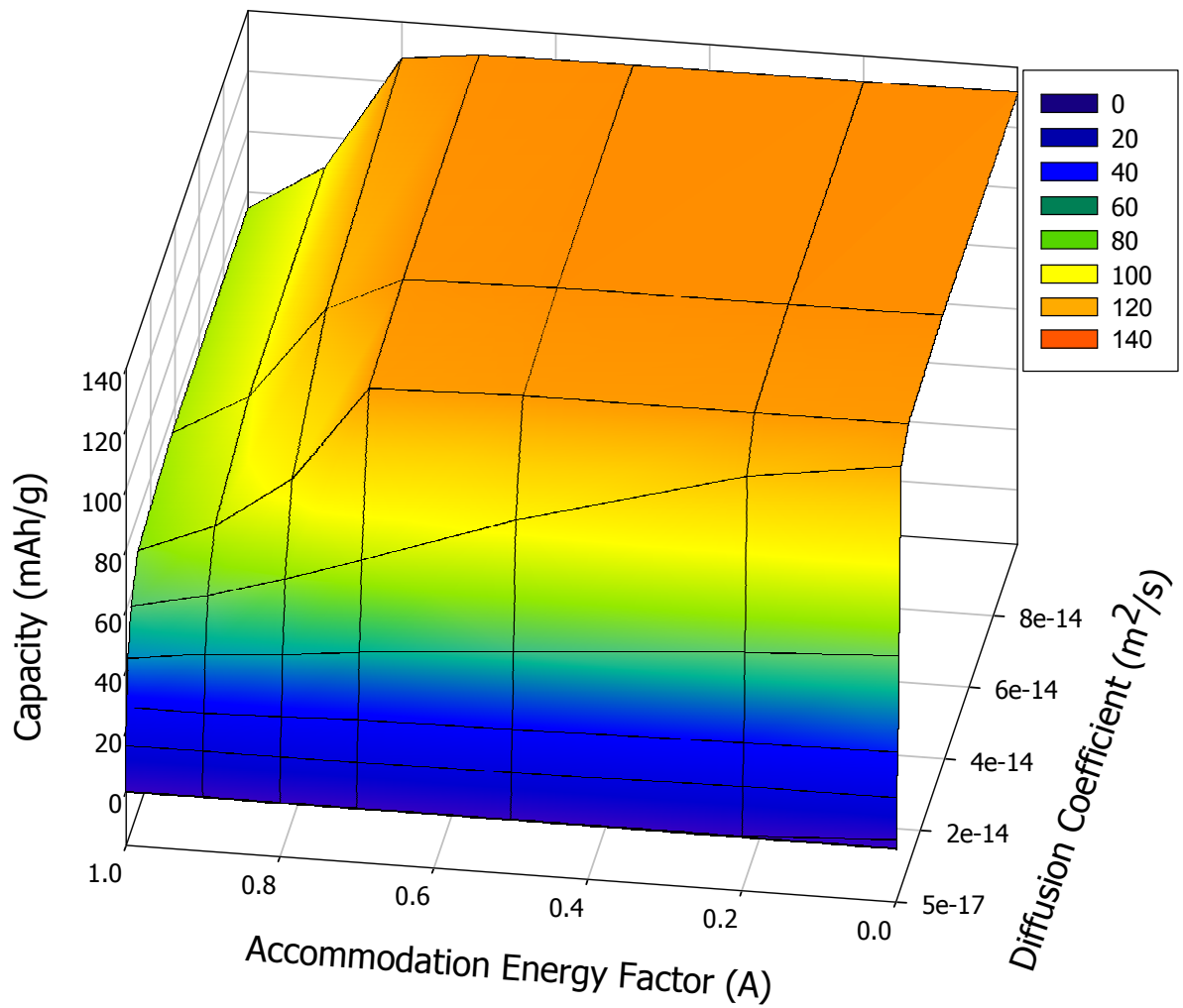


Figure 6.16: Effect of accommodation energy factor and β phase chemical diffusion coefficient on discharge capacity of LiFePO_4 at 10C current

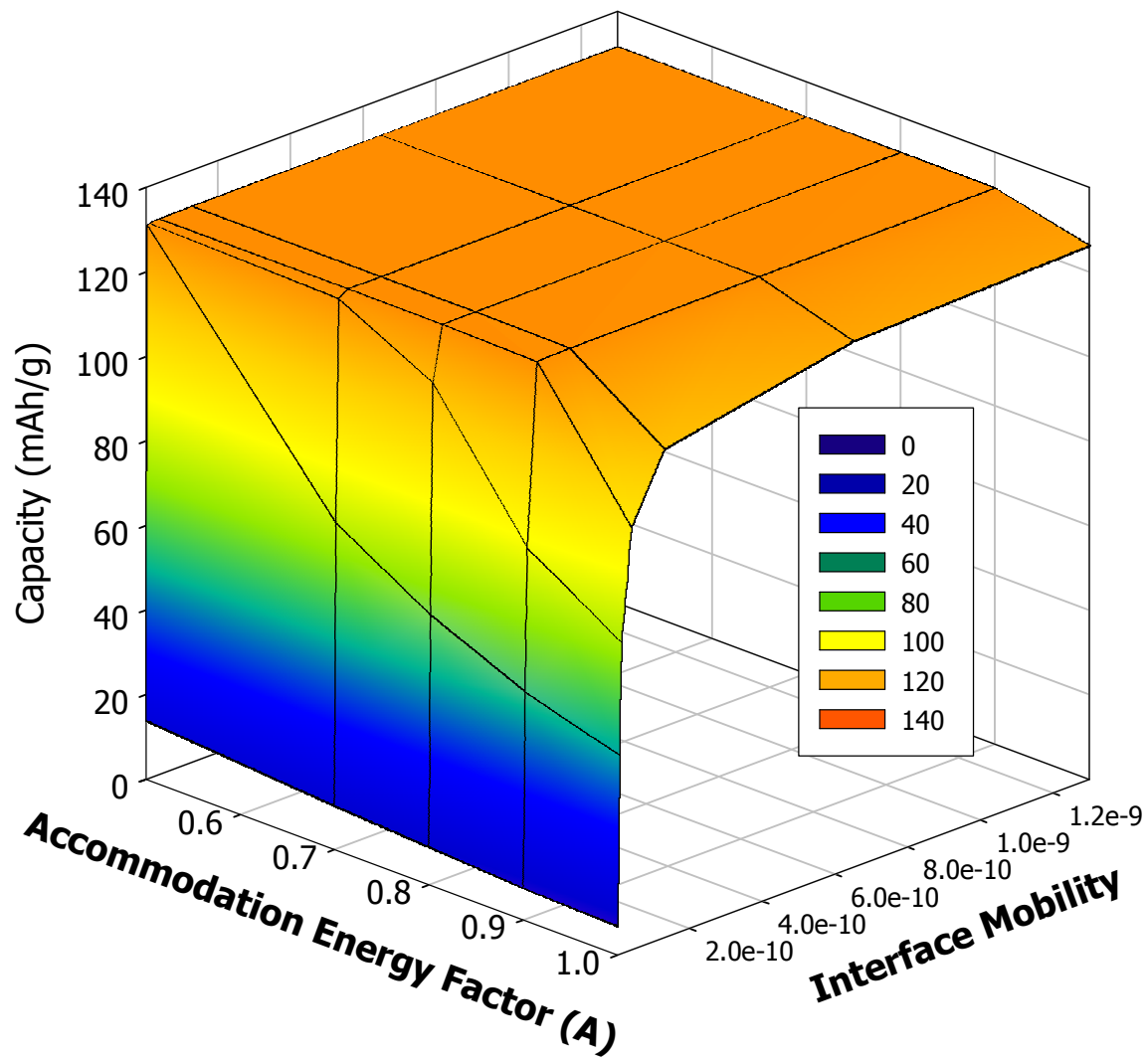


Figure 6.17: Effect of accommodation energy factor and Interface Mobility on discharge capacity of LiFePO₄ at 10C current

6.4 Effect of Particle Size/Diffusion Length on Rate Capability

As mentioned in section 2.1, reducing the particle size to nano meters is found to increase the rate capability of LiFePO_4 greatly [36-39]. Here, an effort is made to determine the influence of particle size on the rate capability of LiFePO_4 from the modified SCM-2. This is done by changing the Li^+ ion diffusion length (x_0) from $1.5 \mu\text{m}$ to 40 nm , while keeping all the other parameters constant (same as that of sample A). Figure 6.18 shows the discharge capacity of LiFePO_4 at 1C, 10C, and 20C as a function of diffusion length. As shown in Figure 6.18, the discharge capacity at 1C increases linearly with the decrease in diffusion length, which is in agreement with the recent reported results [39]. Contrary to the behavior observed at 1C, discharge capacity at high currents (10C and 20C) increases greatly with the decrease in diffusion length. These results imply that it is possible to attain a high rate capability for LiFePO_4 by reducing the size to the order of the nano scale. Similarly high rate capability can be obtained for materials with lower chemical diffusion (Figure 6.19) or lower interface mobility (Figure 6.20) by reducing the diffusion length. From these results, it is evident that the nano materials are very promising electrode materials for Li-ion batteries in high rate applications such as HEVs and EVs.

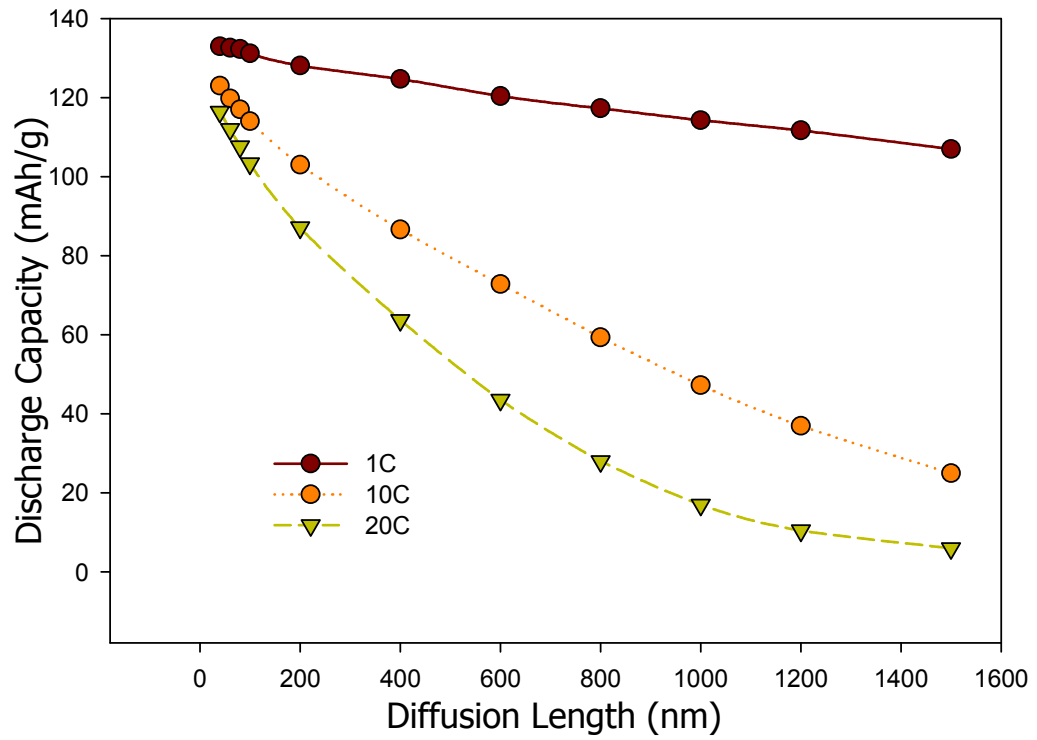


Figure 6.18: Effect of particle radius on discharge capacity of LiFePO_4 at different currents ($D_\beta = 8 \times 10^{-15} \text{ m}^2/\text{s}$, $M = 6.3 \times 10^{-12} \text{ m} \cdot \text{mol}/(\text{J} \cdot \text{s})$)

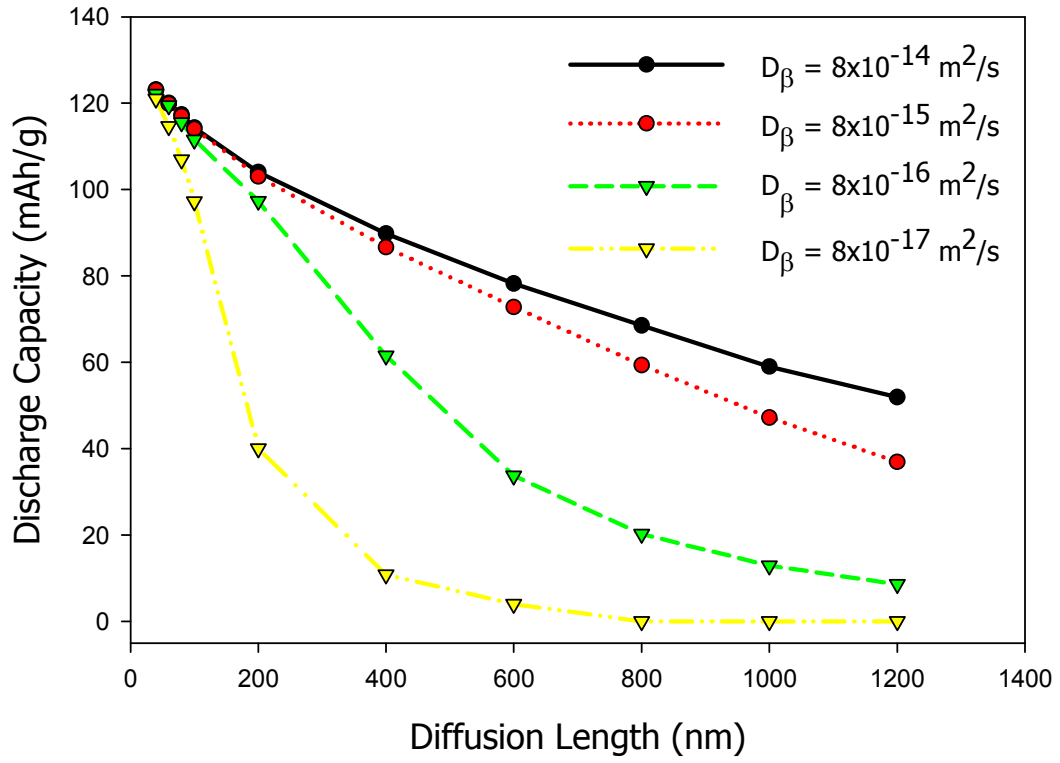


Figure 6.19: Effect of diffusion length on discharge capacity of LiFePO_4 at 10C with different chemical diffusion capabilities ($M = 6.3 \times 10^{-12} \text{ m mol}/(\text{J s})$)

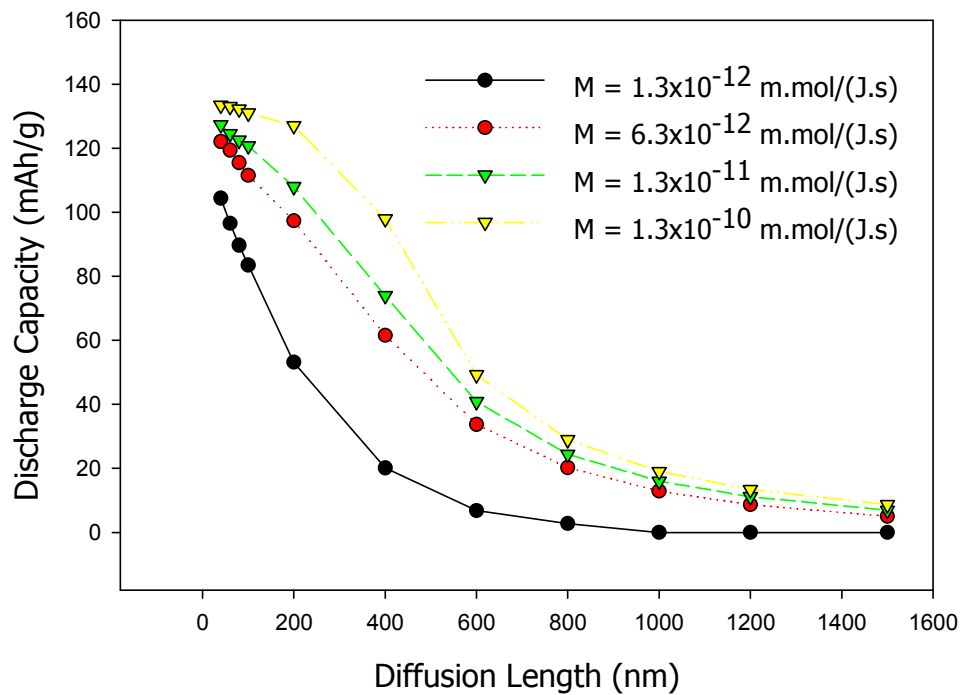


Figure 6.20: Effect of diffusion length on discharge capacity of LiFePO_4 at 10C with different interface mobilities ($D_\beta = 8 \times 10^{-16} \text{ m}^2/\text{s}$)

CHAPTER 7

CONCLUSIONS

Shrinking core model is the only mathematical model, which is applicable to LiFePO_4 cathode materials. However, it cannot accurately predict the discharge behavior of LiFePO_4 at different discharge currents. In this doctoral dissertation work, it is found that the disagreement between experimental discharge curves and the discharge curves obtained from shrinking core model is due to the restrictive assumption (charge/discharge process of LiFePO_4 is controlled by diffusion) used in the development of shrinking core model. Also the charge/discharge process of LiFePO_4 is found to be controlled by both diffusion and phase transformation. Based on these findings and by modifying the shrinking core model, a new mathematical is developed. The difference between the modified shrinking core model and the original shrinking core model is incorporation of parameters relating to phase transformation such as interface mobility and volume change. Due to the addition of these parameters, the modified shrinking core model is applicable to different LiFePO_4 electrodes whose charge/discharge process is controlled by diffusion or phase transformation or both diffusion and phase transformation. Whereas the shrinking core model is applicable for LiFePO_4 cathode whose charge/discharge process is controlled by diffusion alone. Hence the shrinking core model can be considered as a limiting case of the modified shrinking core model developed in this contribution. The detailed findings of this doctoral dissertation are given below.

From the time of invention until today, there has been considerable improvement in its rate capability. This improvement was attributed to factors such as increased

electronic conductivity, Li-ion conductivity, rate of phase transformation, solid solution range, and reduction in particle size. Though there has been considerable improvement in rate capability of LiFePO_4 , the rate controlling mechanism for the discharge of LiFePO_4 is not yet known and it is not clear how these factors affect the rate capability.

To find out the reasons for poor rate capability of LiFePO_4 and to determine the rate-controlling mechanism of LiFePO_4 , the shrinking core model was developed. This model was based on the assumption that the rate of phase transformation in LiFePO_4 is very fast, i.e. charge/discharge process is controlled by chemical diffusion. However, the shrinking core model was not able to completely predict the discharge behavior of LiFePO_4 samples. The poor prediction of shrinking core model was attributed to the large particle size distribution present in these samples. From the comparison of experimental discharge curves of LiFePO_4 with narrow particle size distribution and predictions from shrinking core model, it is found that the poor prediction of shrinking core model is not due to the particle size distribution. From the potential-step chronoamperometry (PSCA) measurement conducted during the charge/discharge process of $\text{LiFe}_{0.9}\text{Mg}_{0.1}\text{PO}_4$, it is found that diffusion is not the only controlling step during the charge/discharge process. From these results, it was evident that the discrepancy between the discharge curves from experiments and shrinking core model is due to restrictive assumption used in the model that the diffusion is the rate-controlling step for charge/discharge process.

Based on these results and by modifying the shrinking core model, a novel mathematical model for discharge process of phase transformation electrodes is developed. This model is based on the theory of mixed-mode phase transformation and it assumes that the discharge process is controlled by both chemical diffusion and rate of

phase transformation. The model developed in this doctoral dissertation work is a comprehensive model as it involves properties such chemical diffusion (electronic and Li-ion conductivity) in α and β phases, rate of phase transformation, solid solution range, and volume change.

The modified shrinking core model was validated by predicting the discharge behavior of two commercial LiFePO_4 samples (obtained from the industrial suppliers) at different current densities (Samples A and B). Sample A and sample B have different discharge characteristics and different rate capabilities. At 0.1C, sample A has shown a discharge capacity of 132 mAh/g and sample B has shown a discharge capacity of 144 mAh/g. Although sample A has higher solid solution range than sample B, the rate capability of sample A is much lower than that of sample B. At 5C, sample B has shown 90% rate capability, whereas sample A has shown only 67% rate capability. From the values of the parameters used in the new model, it can be concluded that the high rate capability of sample B is due to its very high interface mobility. These results show the importance of rate of phase transformation in improving the rate capability of LiFePO_4 . The modified shrinking core model was also validated by predicting the rate capability behavior of cation-doped nanoscale LiFePO_4 and conventional LiFePO_4 , which differ in miscibility gap and interface structure.

When the interface mobility is assumed to be high ($\approx 10^{-8}$ mmol/(J's)) in the modified shrinking core model, the discharge behavior predicted from the model matches with the discharge behavior predicted from diffusion controlled shrinking core model. These results strongly validate the modified shrinking model and show its applicability to

various LiFePO₄ materials, whose discharge process is controlled by diffusion or phase transformation or both diffusion and phase transformation.

Using the validated model as a tool and by determining the effects of chemical diffusion, rate of phase transformation, solid solution range, volume change and particle size on rate capability of LiFePO₄, a detailed rate capability analysis is done. Few important conclusions from the rate capability analysis can be summarized as follows:

- Rate capability of LiFePO₄ can be improved by improving the chemical diffusion coefficient or interface mobility. However, compared to electrode materials with high chemical diffusion coefficient and low interface mobility and electrode materials with low chemical diffusion coefficient and high interface mobility, electrode materials with moderately high chemical diffusion coefficient and interface mobility possess better rate capability.
- Same rate capability can be achieved for LiFePO₄ with different solid solution ranges, chemical diffusion coefficients and interface mobilities.
- To achieve a better rate capability for LiFePO₄ (sample A) with micron-sized particles and with $\theta_{\beta\alpha} = 0.771$ and $\theta_{\alpha\beta} = 0.015$, the value of the chemical diffusion coefficient (D_{β}) of LiFePO₄ should be higher than 2×10^{-15} m²/s and the value of interface mobility should be larger than 1.3×10^{-11} m mol/(J s).
- For an electrode made of micron-sized particles with moderately low chemical diffusion ability and low solid solution range, it is still possible to achieve high rate capability by maintaining high interface mobility, i.e. rapid phase transformation rate. Similarly, it is possible to achieve a high rate capability by increasing the solid solution range, though the interface mobility is low.

- The phase transformation electrodes with a wide solid solution exhibit high rate capability except when the diffusion coefficients are very low. Increasing either the α solid solution or increasing both α and β solid solutions will increase the rate capability of the electrodes, however the later one has higher impact on rate capability.
- The rate capability of LiFePO_4 can also be improved by reducing the volume change or accommodation energy during the phase transformation, though the chemical diffusion coefficient and interface mobility are low. These results show the reason for the high rate capability of $\text{Li}_4\text{Ti}_5\text{O}_{12}$ compared to LiFePO_4 .
- The rate capability of the phase transformation electrode materials can also be improved by reducing the Li^+ ion diffusion length (particle size) to nano meters, though the rate of the phase transformation and chemical diffusion, are low.

Based on these results, rate capability of LiFePO_4 can be expressed as a function of three important properties: solid solution range, chemical diffusion, and interface mobility. Hence, the rate capability can be plotted in a three-dimensional plot, where solid solution range, chemical diffusion, and interface mobility represent x, y, and z axes. Based on the value of one property, the effect of other two properties on rate capability changes. Here, it should be noted that the chemical diffusion coefficient is a function of electronic conductivity and Li-ion conductivity. Previously, it was proposed that the rate capability of LiFePO_4 is controlled by its electronic conductivity. Though this hypothesis is valid, the validity is limited to particular region in the three-dimensional plot. So to

improve the rate capability of a particular LiFePO_4 sample, it is essential to know the region where it lies in the three-dimensional plot.

Currently, LiFePO_4 is available from different manufactures and surprisingly all of them exhibit different charge-discharge characteristics and different rate capabilities. This can be explained by the difference in properties such as chemical diffusion, phase transformation, solid solution range and volume change; and difference in interface structures (Coherent, semi-coherent, and incoherent), which are accounted in this model. The developed model can be applied to all ion insertion electrodes with phase transformation (such as $\text{Li}_4\text{Ti}_5\text{O}_{12}$ in Li-ion battery and metal-hydride electrodes in Ni/MH batteries), and, therefore, making it a useful practical tool in developing the next generation electrode materials.

CHAPTER 8

FUTURE WORK

In Chapter 5, the development and description of mathematical model to predict the discharge behavior of LiFePO_4 cathode in Li-ion half cells is discussed. Generally, the LiFePO_4 cathode in Li-ion half cell consists of LiFePO_4 (active material), conductive carbon and binder in solid phase form and electrolyte in liquid phase. Models developed in section 5.1 and section 5.2 are particle (active material particle only) scale models and they involve only active material properties such as diffusion, phase transformation, solid solution, etc. But these models do not account for solid phase/matrix properties such as solid phase conductivity, contact resistance between cathode and current collector, electrode thickness, etc., and solution phase properties such as electrolyte conductivity, diffusion coefficient of electrolyte, etc. Since these properties have a strong influence on the discharge behavior at moderate to high currents, the particle scale model cannot be used directly to predict the discharge behavior at high currents. Also the electrode preparation conditions (active material loading, thickness of the electrode, etc.) have a large impact on the discharge behavior. Due to these reasons, the particle scale model is only applicable for thin film electrodes (which contain only active material) and electrodes with low active material loading. Hence, in order to use the mathematical model for predicting the discharge behavior at high currents or discharge behaviors of electrodes with high active material loading, it is necessary to introduce factors such as electrolyte resistance, contact resistance, porosity, etc., into the model. This can be done by coupling the porous electrode theory (developed by John Newman in 1965 [46]) with

particle scale model. Availability of such a comprehensive model can also facilitate the unit cell optimization about given performance requirements to maximize the performance/cost and to understand the trade-offs.

In this chapter, a brief description of porous electrode theory is given and the equations describing the phenomenon occurring in porous electrodes are presented. Also how the equations of porous electrode theory are coupled to the equations of particle scale model is explained. For simplicity in describing the system of equations, particle scale model involving only β phase (refer to section 5.1) is chosen.

8.1 Description of Porous Electrode

Figure 8.1 describes the schematic of a Lithium ion half cell typically used in this contribution. It consists of a positive electrode/cathode, current collector for cathode, Lithium metal working as a negative electrode, a porous separator placed between anode & cathode, and Lithium ion conducting electrolyte. The cathode and anode are in solid phase and the electrolyte is in liquid phase. The electrolyte is prepared by dissolving Lithium ion conducting salt into an organic liquid. The typical concentration of salt in electrolyte varies from 1 to 1.5 M. As a result of high salt concentration, the electrolyte exhibits non-ideal behavior and the mass transport in the electrolyte has a strong impact on the performance of Li-ion cells at moderate to high currents. The cathode is usually made by coating slurry of active material (LiFePO_4 in the present case), conductive filler and binder, onto an Aluminum foil used as current collector. The cathode thus formed exhibits a porous structure as shown in figure 8.1. Such porous structure provides a high

surface area for electrochemical reaction and reduces the distance between reactants and the surfaces where reaction occurs. “In these porous electrodes, the electrochemical reaction is distributed over the surface of the particles of the active material and varies across the depth of the electrode due to interaction of potential drop and the concentration changes in both the solution and solid phases” [46]. The distribution of these reaction rates are dependant on physical structure, conductivity of the matrix (cathode), and of electrolyte, and on the parameters characterizing the electrode processes [87]. Hence, in order to predict the discharge behavior of Li-ion cells accurately at high currents, it is essential to consider the interactions among mass transfer and potential in the electrolyte in anode, cathode, and separator.

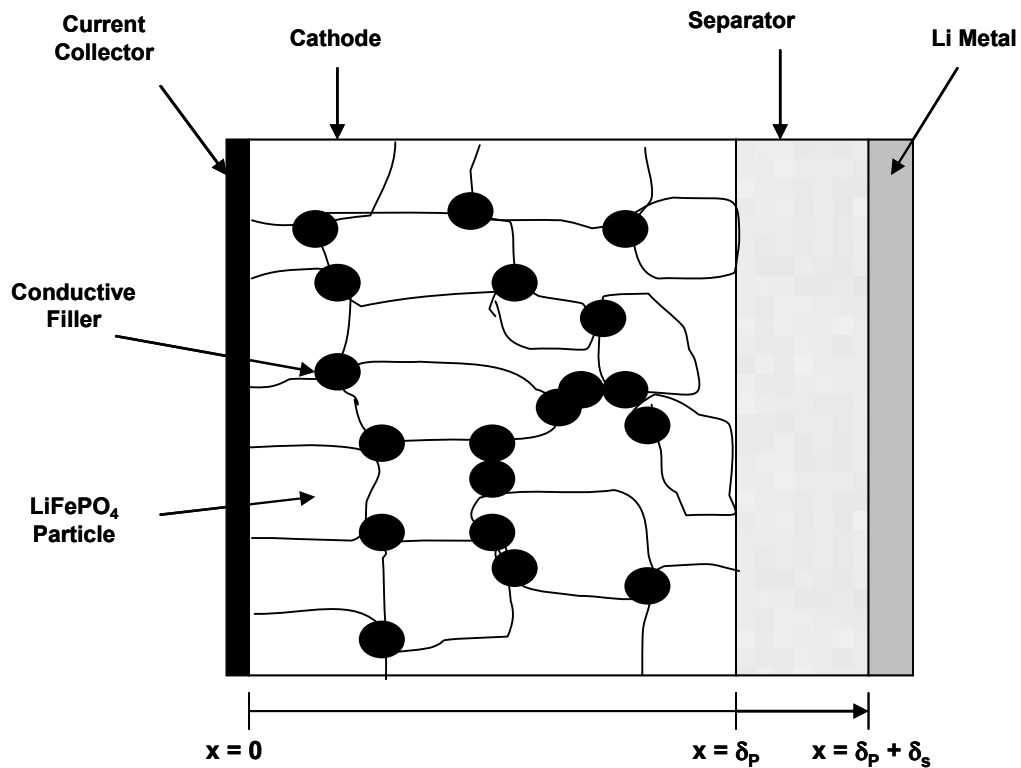


Figure 8.1: Schematic of LiFePO₄ half cell, consisting of current collector, LiFePO₄ electrode, separator and Lithium metal

8.2 Porous Electrode Theory

In porous electrode theory, the exact positions and shapes of all the particles and the pores are not specified. Instead, the electrode is considered as a superposition of active material, conductive filler, and electrolyte and all these phases are considered to be present at every point in the model. The properties of these phases are averaged over an elemental volume small with respect to the overall dimensions of the electrode but small with respect to the pore structure. For developing the equations for porous electrode theory, the following parameters were defined [46,87]. Let ϕ_1 be the potential in the cathode and ϕ_2 be the potential in electrolyte and these are assumed to be continuous functions of time and space. The porosity (ϵ) is defined as the void volume fraction with in the element and is considered to be filled with electrolyte. C_i is the solution phase concentration of species i , averaged over the pores. Then the superficial concentration, averaged over the volume of matrix and pores is ϵC_i . The specific interfacial area a is the surface area of the pore walls per unit volume of the total electrode. j_{in} is the pore-wall flux of species i averaged over the same interfacial area. Therefore, $a j_{in}$ represents the rate of transfer of the species from the solid phases to the pore solution. Similarly, N_i is the average flux of species i in the pore solution when averaged over the cross section of the electrode. Therefore, for a plane surface, of normal unit vector n , cutting the porous solid, $n \cdot N_i$ represents the amount of species i crossing this plane in solution phase.

In the absence of chemical reaction and by performing a differential mass balance for species i with in the pore, the following equation can be obtained:

$$\frac{\partial \varepsilon C_i}{\partial t} = a j_{in} - \nabla \cdot N_i \quad (8.1)$$

where N_i can be expressed as

$$N_i = -\varepsilon D \nabla C_i + \frac{t_i^0}{Z_i F} i_2 \quad (8.2)$$

where D is the diffusion coefficient of electrolyte, Z_i is the charge number of species i , t_i^0 is the transference number of species i , F is the Faraday's constant, and i_2 is the current density in the solution phase. The current applied across the current collector (I) of a Lithium ion battery is carried through both solid phase and solution phase. Hence, it can be expressed as follows:

$$i_1 + i_2 = I \quad (8.3)$$

where i_1 is the solid/matrix phase current.

With the assumption of electro-neutrality in the electrode, the divergence of the total current density becomes equal to zero and it can be expressed by the following equation:

$$\nabla \cdot i_1 + \nabla \cdot i_2 = 0 \quad (8.4)$$

The divergence of solution phase current density can be expressed as a function of pore wall flux of species, j_{in} as follows:

$$\nabla \cdot i_2 = a F \sum_i Z_i j_{in} = a i_n \quad (8.5)$$

where i_n is average transfer current density. Combining Eqs. 8.1, 8.2, and 8.4 results in

$$\frac{\partial \varepsilon C_i}{\partial t} - \nabla \cdot (\varepsilon D \nabla C_i) - \frac{(1 - t_i^0)}{Z_i F} a i_n = 0 \quad (8.6)$$

The above equation is applicable to electrode region and the separator region; however, in the separator region the average current density is equal to zero.

In the matrix/solid phase, electron motion is governed by Ohm's law, which is given by the following equation

$$i_1 = -\sigma \nabla \phi_1 \quad (8.7)$$

where σ is the effective conductivity of the matrix. σ is affected by the volume fraction of the conducting phase, the inherent conductivity of the each conducting solid phase, and the manner in which granules of conducting phases are connected together.

Since the solution phase current density is due to net flux of ions, it can be expressed as

$$i_2 = -k \nabla \phi_2 + \frac{2RT}{F} (1 - t_i^0) \left(1 + \frac{d \ln f_{\pm}}{d \ln C_i} \right) \nabla \ln C_i \quad (8.8)$$

where k is the effective conductivity of the solution phase and f_{\pm} is the mean molar salt activity coefficient.

Rearranging Eq. 8.5 with the aid of Eq. 8.8 results in

$$\nabla \cdot \left(k \nabla \phi_2 - \frac{2RT}{F} (1 - t_i^0) \left(1 + \frac{d \ln f_{\pm}}{d \ln C_i} \right) \nabla \ln C_i \right) = -ai_n \quad (8.9)$$

Rearranging Eq. 8.5 with the aid of Eq. 8.4 and Eq. 8.7 results in

$$\nabla \cdot (\sigma \nabla \phi_1) - ai_n = 0 \quad (8.10)$$

The average transfer current density in Eq. 8.9 and Eq. 8.10 can be determined from polarization or current-overpotential equation (Eq 4.3), which shows the dependence of local rates of reaction on various concentrations and on the potential jump at the matrix solution interface.

$$i_n = i_o \left(\frac{(C_t - C_{\beta s})}{(C_t - C_{\beta \alpha})} \times e^{\left(\frac{\alpha_a F}{RT} (\phi_1 - \phi_2 - U) \right)} - \frac{C_{\beta s}}{C_{\beta \alpha}} \times e^{\left(-\frac{\alpha_c F}{RT} (\phi_1 - \phi_2 - U) \right)} \right) \quad (8.11)$$

where i_o is the exchange current density and U is equilibrium potential of LiFePO_4 cathode determined from the particle scale model.

For Sample A LiFePO_4 , U is given by Eq. 4.1:

$$U = 3.3929 - 0.5 \times e^{\left(\frac{1.55}{\left(\frac{C_{\beta s}}{C_t} \right)^5} + \left(\frac{C_{\beta s}}{C_t} \right) \right)} - 8 \times e^{\left(-\frac{0.52}{\left(\frac{C_{\beta s}}{C_t} \right)^{14}} \right)} \quad (8.12)$$

where $C_{\beta s}$ is the surface concentration of LiFePO_4 particle determined from the particle scale model given in section 5.1.2.

In summary, Eqs. 8.6, 8.9, and 8.10 represent the governing equations for electrolyte concentration, solid phase potential and solution phase potential in Li-ion half cell, as shown in Figure 8.1.

The boundary condition at the lithium foil electrode is that the flux of anion is zero. Therefore the diffusion of anion is balanced by migration, which is given as follows:

$$\varepsilon \frac{\partial C_i}{\partial x} = \frac{(1-t_i^0)}{Z_i F} aI, \quad x = \delta_p + \delta_s \quad (8.13)$$

Similarly the flux of salt is zero at the current collector for cathode,

$$\frac{\partial C_i}{\partial x} = 0, \quad x = 0 \quad (8.14)$$

At the interface between cathode and separator, the concentration and flux are continuous, which can be expressed as

$$-D \frac{\partial C_i}{\partial x} \Big|_{x=\delta_p^-} = -D \frac{\partial C_i}{\partial x} \Big|_{x=\delta_p^+} \quad (8.15)$$

Eqs. 8.13, 8.14, and 8.15 are the boundary conditions for governing Eq. 8.6.

The average transfer current density is equivalent to the total current density at the current collector and is equivalent to zero at the cathode/separator interface. As a result, Eq. 8.10 can be rearranged as follows:

$$-\sigma \frac{\partial \phi_1}{\partial x} = aI, \quad x=0 \quad (8.16)$$

$$\frac{\partial \phi_1}{\partial x} = 0, \quad x = \delta_p^- \quad (8.17)$$

Eq. 8.16 and 8.17 are the boundary conditions for governing Eq. 8.10.

Since the flux of salt is zero at the current collector for cathode, the potential gradient in the solution phase at the current collector is equivalent to zero, which can be expressed as

$$\frac{\partial \phi_2}{\partial x} = 0, \quad x = 0 \quad (8.18)$$

In addition to Eq. 8.18, the other boundary conditions for Eq. 8.9 are given as follows:

$$-k \frac{\partial \phi_2}{\partial x} \Big|_{x=\delta_p^-} = -k \frac{\partial \phi_2}{\partial x} \Big|_{x=\delta_p^+} \quad (8.19)$$

$$I = i_0 \left(\exp\left(\frac{\alpha_a F}{RT} (-\phi_2)\right) - \exp\left(-\frac{\alpha_c F}{RT} (-\phi_2)\right) \right), \quad x = \delta_p + \delta_s \quad (8.20)$$

8.3 Summary of System of Equations

8.3.1 Equations for Porous Electrode

Governing Equation 1:

$$\frac{\partial \varepsilon C_i}{\partial t} - \nabla \cdot (\varepsilon D \nabla C_i) - \frac{(1-t_i^0)}{Z_i F} a i_n = 0, \text{ cathode, } 0 < x < \delta_p$$

$$\frac{\partial \varepsilon C_i}{\partial t} - \nabla \cdot (\varepsilon D \nabla C_i) = 0, \text{ separator, } \delta_p < x < \delta_p + \delta_s$$

Boundary Conditions for Governing Equation 1:

$$\frac{\partial C_i}{\partial x} = 0, \text{ Current collector/cathode interface, } x = 0$$

$$-D \left. \frac{\partial C_i}{\partial x} \right|_{x=\delta_p^-} = -D \left. \frac{\partial C_i}{\partial x} \right|_{x=\delta_p^+}, \text{ cathode/separator interface}$$

$$\varepsilon \frac{\partial C_i}{\partial x} = \frac{(1-t_i^0)}{Z_i F} a I, \text{ separator/Li metal interface, } x = \delta_p + \delta_s$$

Governing Equation 2:

$$\nabla \cdot (\sigma \nabla \phi_1) - a i_n = 0, \text{ cathode, } 0 < x < \delta_p$$

Boundary Conditions for Governing Equation 2:

$$-\sigma \frac{\partial \phi_1}{\partial x} = a I, \text{ Current collector/cathode interface, } x = 0$$

$$\frac{\partial \phi_1}{\partial x} = 0, \text{ cathode/separator interface, } x = \delta_p^-$$

Governing Equation 3:

$$\nabla \cdot \left(k \nabla \phi_2 - \frac{2RT}{F} (1 - t_i^0) \left(1 + \frac{d \ln f_{\pm}}{d \ln C_i} \right) \nabla \ln C_i \right) = -a i_n, \text{ cathode, } 0 < x < \delta_p$$

$$\nabla \cdot \left(k \nabla \phi_2 - \frac{2RT}{F} (1 - t_i^0) \left(1 + \frac{d \ln f_{\pm}}{d \ln C_i} \right) \nabla \ln C_i \right) = 0, \text{ separator, } \delta_p < x < \delta_p + \delta_s$$

Boundary Conditions for Governing Equation 3:

$$\frac{\partial \phi_2}{\partial x} = 0, \text{ Current collector/cathode interface, } x = 0$$

$$-k \frac{\partial \phi_2}{\partial x} \Big|_{x=\delta_p^-} = -k \frac{\partial \phi_2}{\partial x} \Big|_{x=\delta_p^+}, \text{ cathode/separator interface}$$

$$I = i_0 \left(\exp \left(\frac{\alpha_a F}{RT} (-\phi_2) \right) - \exp \left(-\frac{\alpha_c F}{RT} (-\phi_2) \right) \right), \text{ separator/Li metal interface, } x = \delta_p + \delta_s$$

Equation for i_n :

$$i_n = i_o \left(\frac{(C_t - C_{\beta s})}{(C_t - C_{\beta \alpha})} \times e^{\left(\frac{\alpha_a F}{RT} (\phi_1 - \phi_2 - U) \right)} - \frac{C_{\beta s}}{C_{\beta \alpha}} \times e^{\left(-\frac{\alpha_c F}{RT} (\phi_1 - \phi_2 - U) \right)} \right)$$

Equation for U :

$$U = 3.3929 - 0.5 \times e^{\left(\frac{1.55}{\left(\frac{C_{\beta s}}{C_t} \right)^5 + \left(\frac{C_{\beta s}}{C_t} \right)} \right)} - 8 \times e^{\left(\frac{0.52}{\left(\frac{C_{\beta s}}{C_t} \right)^{14}} \right)}$$

8.3.2 Determination of $C_{\beta s}$ from Particle Scale Model (refer to section 5.1.2)

For Region II:

$$\frac{\partial C_{\beta}}{\partial t} = D_{\beta} \left(\frac{\partial^2 C_{\beta}}{\partial x^2} \right)$$

$$C_{\beta} = 0 \text{ at } t = 0$$

$$D_{\beta} \left(\frac{\partial C_{\beta}}{\partial x} \right) = \frac{i_n}{F} \text{ at surface } x = x_0$$

$$C_{\beta} = C_{\beta i} \text{ at interface } x = x_C(t)$$

$$\frac{dx_C(t)}{dt} = \frac{D_{\beta}}{(-C_{\beta i})} \left(\frac{\partial C_{\beta}}{\partial x} \right)_{x=x_C(t)} \text{ at interface } x = x_C(t)$$

$$\left(\frac{C_{\beta i}}{C_{\beta \alpha}} - 1 \right) \times (C_{\beta i}) = \frac{D_{\beta} \left(\frac{\partial C_{\beta}}{\partial x} \right)_{x=x_C(t)}}{MRT(1 - A \times P \times f(x_C(t)))}$$

For Region III:

$$\frac{\partial C_{\beta}}{\partial t} = D_{\beta} \left(\frac{\partial^2 C_{\beta}}{\partial x^2} \right)$$

$$D_{\beta} \left(\frac{\partial C_{\beta}}{\partial x} \right) = \frac{i_n}{F}, \text{ at surface } (x = x_0)$$

$$D_{\beta} \left(\frac{\partial C_{\beta}}{\partial x} \right) = 0, \text{ at particle center } (x = 0)$$

In order to solve the particle scale model, the value of the parameter i_n in the boundary condition at the surface needs to be obtained. To determine the parameter i_n , the values of solid phase potential (ϕ_1) and solution phase potential (ϕ_2) need to be determined, which is only possible by solving the equations of porous electrode theory. However, the equations of porous electrode theory cannot be solved until the value of the parameter i_n is known. From the discussion, it is evident that the equations of particle scale model, which correspond to a moving boundary problem, are coupled to the equations of porous electrode through the polarization or current-over potential equation. Due to this reason, the above system of equations needs to be solved simultaneously and hence represents a complex system to be solved by numerical methods.

8.4 Possible Strategy for Solving the System of Equations

The system of equations in shrinking core models used by Srinivasan et al. [53] and Zhang et al. [66] can be derived from the system of equations described in section 8.3.2 by assuming that the phase transformation is controlled by diffusion alone. Here, in this section, a brief review of the method used by above authors to solve the respective system of equations is presented.

The system of equations solved by Srinivasan et al. [53] is applicable to LiFePO_4 chemistry and it involves a particle scale model (in spherical coordinates), which is coupled to porous electrode model (in Cartesian coordinates). The particle scale model is a moving boundary problem, which involves only β phase (neglects α phase). To simplify the solution procedure, the particle scale model was converted to stationary

boundary problem. To solve the resulting system of equations, a pseudo 2D approach was used, where one Band subroutine was used for porous electrode model (with stationary boundary) and second Band subroutine was used for particle scale model with stationary boundary. The time stepping was done using Crank-Nicolson method. Initially guess values were given to all the parameters in the particle scale model, including the reaction current (i_n in the boundary condition of the particle scale model, refer to section 8.3.2) and the surface concentration was obtained. Surface concentration was fed to electrode scale model (combination of porous electrode model and particle scale model), the iterations were run until the convergence is achieved.

The system of equations solved by Zhang et al. [66] is applicable to both LiFePO_4 and LiCoO_2 chemistries. The system also involves both particle scale (in spherical coordinates) and porous electrode models (in Cartesian coordinates), which are coupled to each other. But, the particle scale model for this system also includes α phase. The equations of the particle scale model were converted from moving boundary to a stationary boundary with the aid of the Landau transformation method. Then the resulting equations of particle scale model and the equations of porous electrode model were converted to differential algebraic equations by using finite difference technique. The differential algebraic equations were solved by using FORTRAN DAE solver DDSART. “To solve the DAEs, the DDSART solver uses a combination of backward differentiation formula and a choice of direct linear system solution method” [88]. Since the two systems of equations described above can be derived from the system of equations mentioned in section 3.1.2, the methods used for solving them could be used here. Such

approach would guide us in finding out the suitable method to solve the complex system of equations.

List of Symbols

a	surface area of pore walls per unit volume of total electrode, m^2
a_p	β phase radius, m
A	accommodation energy factor
C_i	solution phase concentration of species i , mol/m^3
C_α	lithium concentration in α phase, mol/m^3
C_β	lithium concentration in β phase, mol/m^3
$C_{\alpha\beta}$	equilibrium lithium concentration in α phase at the interface, mol/m^3
$C_{\beta\alpha}$	equilibrium lithium concentration in β phase at the interface, mol/m^3
$C_{\alpha i}$	real lithium concentration in α phase at the interface, mol/m^3
$C_{\beta i}$	real lithium concentration in β phase at the interface, mol/m^3
$C_{\alpha S}$	lithium concentration in α phase at the surface, mol/m^3
$C_{\beta S}$	lithium concentration in β phase at the surface, mol/m^3
C_t	maximum lithium concentration in $FePO_4/LiFePO_4$ lattice, mol/m^3
\hat{D}	Effective diffusion coefficient, m^2/s
D	Diffusion coefficient of the electrolyte, m^2/s
D_e	Electron diffusion coefficient, m^2/s
D_i	Ionic diffusion coefficient, m^2/s
D_α	mixed diffusion coefficient in the α phase, m^2/s
D_β	mixed diffusion coefficient in the α phase, m^2/s
f_\pm	mean molar salt activity coefficient
F	Faraday's constant, 96487 C/mol
I	total current density applied, A/m^2
i	reaction current applied at the particle surface, A/m^2
i_n	average transfer current density, A/m^2
i_1	current density in solid phase/matrix, A/m^2
i_2	current density in solution phase, A/m^2
i_0	exchange current, A/m^2
j_{in}	pore wall flux of species i in solid phase, $mol/(m^2 \cdot s)$
J_{Li}^i	flux of Li^+ ions across the interface, $mol/(m^2 \cdot s)$
j_{Li}^β	flux of Li^+ ions towards the interface, $mol/(m^2 \cdot s)$
k	effective conductivity of solution phase, S/m
K	bulk modulus of α phase
M	interface mobility, $m/mol/(J \cdot s)$
n	exponential term

N_i	average flux of species i in pore solution, mol/(m ² .s)
P	proportionality Factor
r	radial position in the particle, m
r_c	radial position of the interface in the particle, m
r_p	plastic zone radius, m
R	Gas constant, 8.3145 J/mol.k
R_p	particle radius, m
t	time, s
t_i^0	transference number of species, i
T	temperature, K
U	equilibrium potential, V
V_i	molar volume of phase, i
x	axial position in the particle, m
x_0	total Li ⁺ ion diffusion length in the particle, m
$x_C(t)$	position of the phase boundary, m
X	dimensionless axial/radial position in the particle
X_C	dimensionless axial/radial position of the interface
W	total accommodation energy, J/(mol.m ³)
Z_i	charge number of species, i
Z_α, Z_β	dimensionless variables
$\Delta G_{\alpha-\beta}^i$	driving force for the phase transformation, J/mol
$\Delta G_{\alpha-\beta}^{Chem}$	chemical free energy, J/mol
$\Delta G_{\alpha-\beta}^{Elastic}$	elastic accommodation energy, J/mol
$\Delta G_{\alpha-\beta}^{Plastic}$	plastic accommodation energy, J/mol
$\Delta G_{\alpha-\beta}^{Surface}$	free energy resulting from free surfaces, J/mol
$\eta(t)$	over-potential, V
ρ	density of LiFePO ₄ , g/m ³
α	reacted fraction
α_1	transfer coefficient
ξ	position of the phase boundary
ε	porosity of the cathode
ε_p	radial stress free misfit strain
σ	effective conductivity of matrix, S/m
σ_{Li}	Li ⁺ ion conductivity of LiFePO ₄ , S/m
σ_e	Electronic conductivity of LiFePO ₄ , S/m
σ_y	yield stress of α phase
ϕ_1	potential in the cathode, V
ϕ_2	potential in the electrolyte, V
μ	shear modulus of α phase
ν	poisson's ratio of α phase
$\delta, \delta_1, \delta_2$	dimensionless current density
τ	dimensionless time
θ_α	dimensionless lithium concentration in α phase

θ_β	dimensionless lithium concentration in β phase
$\theta_{\alpha\beta}$	dimensionless equilibrium lithium concentration in α phase at the interface
$\theta_{\beta\alpha}$	dimensionless equilibrium lithium concentration in β phase at the interface
$\theta_{\alpha i}$	dimensionless real lithium concentration in α phase at the interface
$\theta_{\beta i}$	dimensionless real lithium concentration in β phase at the interface
$\theta_{\alpha S}$	dimensionless lithium concentration in α phase at the surface
$\theta_{\beta S}$	dimensionless lithium concentration in β phase at the surface

REFERENCES

1. "World Consumption of Primary Energy by Energy Type and Selected Country Groups, 1980-2004 (.XLS File)," Energy Information Administration, U.S. Department of Energy (July 31, 2006).
2. "Petroleum Basic Statistics Data for 2007," Energy Information Administration, U.S. Department of Energy (<http://www.eia.doe.gov/basics/quickoil.html>).
3. "U.S. Primary Energy Consumption by Source and Sector, 2007," Energy Information Administration, U.S. Department of Energy (http://www.eia.doe.gov/emeu/aer/pecss_diagram.html).
4. "World Proved Reserves of Oil and Natural Gas, Most Recent Estimates," Energy Information Administration, U.S. Department of Energy (<http://www.eia.doe.gov/emeu/international/reserves.html>).
5. "Inventory of U.S. Greenhouse gas emissions and sinks: 1990-2006," USEPA #430-R-08-005, U.S. Greenhouse Gas Inventory Reports.
6. Handbook of Batteries and Fuel Cells, 2nd edition, edited by D. Linden, McGraw-Hill Book Company, 1984.
7. Winter; M. Besenhard; J. O. Spahr; M. E. Novak; P., Adv. Mater., 10 (10), 725 (1998).
8. <http://auto.howstuffworks.com/lithium-ion-battery-car2.htm>
9. Padhi, A. K. Nanjundaswamy; Goodenough, J. B. . *J. Electrochem. Soc.*, 144, 1188 (1997).
10. Ravet; N. Goodenough; J. B. Besner; S. Simonneau; P. Hovington; P. Armand; M. Abstract 127, The Electrochemical Society and The Electrochemical Society of Japan Meeting Abstracts, Vol. 99-2, Honolulu, HI, Oct 17-22, 1999.
11. Ravet; N. Chouinard; Y. Magnan; J. F. Besner; S. Simonneau; P. Gauthier; M. Armand; M. Abstract 166, International Meeting on Lithium Batteries, Como, Italy, May 28-June 2, 2000.
12. Ravet; N. Besner; S. Simonneau; P. Vallee; A. Armand; M. Hydro-Quebec, Can. Pat., 2,270,771.
13. Huang, H.; Yin, S. -C.; Nazar, L. F. *Electrochem. Solid-State Lett.*, 4, A170 (2001).
14. Doeff, M. M.; x Hu, M. M.; McLarnon, F.; Kostecki, F. *Electrochem. Solid-State Lett.*, 6, A207 (2003).
15. Chung, S-Y.; Bloking, J. T.; Chiang, Y-M. *Nature Materials*, 1, 123 (2002).

16. Chung; S-Y. Chiang; Y-M. *Electrochem. Solid-State Lett.*, 6, A278 (2003).
17. Chung, S-Y.; Bloking, J. T.; Chiang, Y-M. *Nature Materials*, 2, 702 (2003).
18. Herle; P. S. Ellis; B. Coombs; N. Nazar; L. F. *Nature Materials*, 3, 147 (2004).
19. Croce; F. Epifanio; A. D. Hassoun; J. Deptula; A. Olczac; T. Scrosati; B. *Electrochem. Solid-State Lett.*, 5, A47 (2002).
20. Wang; D. Li; H. Shi; S. Huang; X. Chen; L. *Electrochim. Acta.*, 50, 2955 (2005).
21. Wang; C. Hong; J. *Electrochem. Solid-St. Lett.*, 10, A65 (2007).
22. Striebel; K. Shim; J. Srinivasan; V. Newman; J. *J. Electrochem. Soc.*, 152, A664 (2005).
23. Reiss; I. *Solid State Ionics.*, 157, 1 (2003).
24. Chiang; Y-M. Meethong; N. Huang; H-Y. S. Carter; W. C. Chang; S. Hsiao; A. Gozdz; A. S. ECS Meeting 2006, Cancun, November.
25. Meethong; N. Huang; H-Y. S. Speekman; S. A. Carter; W. C. Chiang; Y-M. *Adv. Funct. Mater.*, 17, 1115 (2007).
26. Meethong; N. Huang; H-Y. S. Speekman; S. A. Carter; W. C. Chiang; Y-M. *Electrochem. Solid-State Lett.*, 10, A134 (2007).
27. Nakamura; T. Sakumoto; K. Seki; S. Kobayashi; Y. Tabuchi; M. Yamada; Y. *J. Electrochem. Soc.*, 154, A1118 (2007).
28. Nakamura; T. Sakumoto; K. Okamoto; M. Seki; S. Kobayashi; Y. Takeuchi; T. Tabuchi; M. Yamada; Y. *J. Power Sources.*, 174, 435 (2007).
29. Colbow; K. M. Dahn; J. R. Hearing; R. R. *J. Power Sources.*, 26, 397 (1989).
30. Ferg; E. Gummow; R. J. Kock; A. de. Thackeray. M. M. *J. Electrochem. Soc.*, 11, 141 (1994).
31. Ohzuku; T. Ueda; A. Yamamoto; N. *J. Electrochem. Soc.*, 142, 1431 (1995).
32. Ma; J. Wang; C. Wroblewski; S. *J. Power Sources*, 164, 849 (2007).
33. Nakahara; K. Nakajima; R. Matsushima; T. Majima; H. *J. Power Sources.*, 117, 131 (2003).

34. Cheng; L. Liu; H-J. Zhang; J-J. Xiong; H-M. Xia; Y-Y. *J. Electrochem. Soc.*, 153, A1472 (2006).
35. Kim; J. Cho; *J. Electrochem. Solid-State Lett.*, 10, A81 (2007).
36. Sides; C. R. Croce; F. Young; V. Y. Martin; C. R. Scrosati; B. *Electrochem. Solid-St. Lett.*, 8, A484 (2005).
37. Kim; D-H. Kim; *J. Electrochem. Solid-St. Lett.*, 9, A439 (2006).
38. Delacourt; C. Poizot; P. Levasseur; S. Masquelier; C. *Electrochem. Solid-State Lett.*, 9, A352 (2006).
39. Gaberscek; M. Dominko; R. Jamnik; *J. Electrochem. Commun.*, 9,2778 (2007).
40. West; K. Jacobsen; T. Atlung; S. *J. Electrochem. Soc.*, 129, 1480 (1982).
41. Doyle; M. Fuller; T. Newman; *J. J. Electrochem. Soc.*, 140, 1526 (1993).
42. Nagarajan; G. S. Van Zee; J. W. Spotnitz; R. M. *J. Electrochem. Soc.*, 145, 771 (1998).
43. Verbrugge; M. W. Koch B. J., *J. Electrochem. Soc.*, 150, A374 (2003).
44. Doyle M., Yuentes F., *J. Electrochem. Soc.*, 150, A706 (2003).
45. Botte; G. G. Subramanian; V. R. White; R. E. *Electrochim. Acta.*, 45, 2595 (2000).
46. Thomas; K. E. Newman; J. Darling; R. M. Chapter 12, *Advances in Lithium-Ion Batteries*, Kluwer Academic/Plenum Publishers, 2002.
47. Gomdam; P. M. Weidner; J. W. Dougal; R. A. White; R. E. *J. Power Sources.*, 110, 267 (2002).
48. Yagi; S. Kinii; D. 1955, Studies on combustion of carbon particles in flames and fluidized beds. In; Fifth symposium (International) on combustion, Reinhold, New York, pp. 231-244.
49. Szekely; J. Evans; J. W. Sohn; H. Y. 1976, *Gas Solid Reactions*. Academic Press, New York.
50. Levenspiel; O. 1979. *Chemical Reaction Engineering*, 3rd Edition. Wiley, New York.
51. Wen; C. Y. *J. Ind. Eng. Chem.* 60, 36 (1968).

52. Subramanian; V. R. Ploehn; H. J. White; R. E. *J. Electrochem. Soc.*, 147, 2868 (2000).
53. Srinivasan; V. Newman; J. *J. Electrochem. Soc.*, 151, A1517 (2004).
54. Hong; J. Wang; C. Kasavajjula; U. *J. Power Sources.*, 162, 1289 (2006).
55. Geoffroy; D. Ravet; N. 21st International Seminar and Exhibit on Primary & Secondary Batteries 2004, Fort Lauderdale, Florida, March.
56. Nowak; U. *Applied Numerical Mathematics*, 20, 129 (1996).
57. Zhang; W. *Applied Numerical Mathematics*, 20, 235 (1996).
58. Bard; A. J. Faulkner; L. R. *Electrochemical Methods* 2004, 2nd Edition, John Wiley & Sons, Inc.; p 99.
59. Chen; G. Song; X. Richardson; T. J. *Electrochem. Solid-State Lett.* 9, A295 (2006).
60. Funabiki; A. Inaba; M. Abe; T. Ogumi; Z. J. *Electrochem. Soc.* 146, 2443 (1999).
61. Gunawardena; G. Hills; G. Montenegro; I. Scharifker; B. J. *Electroanal. Chem.* 138, 225 (1982).
62. Lee; J. W. Pyun II; S. *Electrochim. Acta.* 50, 1777 (2005).
63. Jost; W. *Diffusion in Solids, Liquids, Gases*, Academic, New York, 1960 (Chapter I).
64. Porter; D. A. Easterling; K. E. *Phase Transformations in Metals and Alloys*, 2nd ed., Stanley Thorne, UK, 1992 (Chapter 5).
65. Feng; F. Han; J. Geng; M. Northwood; D.O. *Sol. Energy Mater. Sol. Cells.* 62, 51 (2000).
66. Zhang; Q. White; R. E. *J. Electrochem. Soc.*, 154, A587 (2007).
67. Christian; J. *The Theory of Phase Transformations in Metals and Alloys* 1981, Oxford; Pergamon Press.
68. Sietsma; J. Zwaag; S. V. D. *Acta Mater.*, 52, 4143 (2004).
69. Nolfi; F. V. Shewman; P. G. Foster; J. S. *Trans Metall Soc AIME*, 245, 1427 (1969).
70. Ruiheng; W. U. Xueyu; R. Zhang; H. Hsu; T. Y. *J. Mater. Sci. Techno.*, 20, 561 (2004).

71. Sietsma; J. Mecozzi; M. G. Bohemen; S. M. C. Zwaag; S. V. D. Int. J. Mat. Res., 7, 356 (2004).
72. Balasubramaniam; R. J. Alloys and compounds, 253, 203 (1997).
73. Birnbaum; H. K. Grossbeck; M. L. Amano; M. J. less-common Metals 49, 357 (1976).
74. Flanagan; T. B. Clewley; J. D. J. less-common Metals 83, 127 (1982).
75. Flanagan; T. B. Oates; W. A. Kishimoto; S. Scripta Metall. 16, 293 (1982).
76. Kuji; T. Flanagan; T. B. Sakamoto; Y. Hasaka; M. Scripta Metall. 19, 1369 (1985).
77. Balasubramaniam; R. J. Acta metal. Mater. 12, 3341 (1993).
78. Lee; J. K. Earmme; Y. Y. Aaronson; H. I. Russell; K. C. Metallurgical Transactions, 11A, 1837 (1980).
79. Earmme; Y. Y. Johnson; W. C. Lee; J. K. Metallurgical Transactions, 12A, 1521 (1981).
80. Liu; Y. C. Sommer; F. Mittemeijer; E. J. Acta Mater. 52, 2549 (2004).
81. Breierova; L. Choudhari; M. Forrester; J. W. "Introduction to Sensitivity Analysis," A Project for System Dynamics, September 6, 1996.
82. Annual Progress Report on Energy Storage Research and Development, Freedom Car and Vehicle Technologies Program, 2005.
83. Whittingham; M. S. Song; Y. Lutta; S. Zavalij; P. Y. Chernova; N. A. J. Mater. Chem., 15, 3362 (2005).
84. Ellis; B. Perry; L. K. Ryan; D. H. Nazar; L. F. J. Am. Chem. Soc., 128, 11416 (2006).
85. Prosini; P. P. Lisi; M. Zane; D. Pasquali; M. Solid State Ionics, 148, 45 (2002).
86. Yu; D. Y. W. Fietzek, C.; Weydanz, W.; Donoue, K.; Kurokawa, H.; Fujitani, S. J. Electrochem. Soc., 154, A253 (2007).
87. J. Newman, W. Tiedemann, AIChE Journal, 21, 25 (1975).
88. K. E. Brenan, S. L. Campbell, and L. R. Petzold, *Numerical Solution of Initial Problems in Differential-Algebraic Equations*, Elsevier, New York (1989).

VITA

Mr. Uday Shankar Kasavajjula was born in Hyderabad, India, in 1982. He earned his Bachelor's degree in the field of Chemical Engineering at Chaitanya Bharathi Institute of Technology, Hyderabad, India, in the year 2002. He pursued his Master's degree in the field of Chemical Engineering at Tennessee Technological University, USA, in the year 2005. In Fall 2005, he joined in the Ph.D. program in Chemical Engineering at Tennessee Technological University. During his graduate student life, he was pursuing his research in the field of Lithium ion batteries. His other research interests are renewable energy and modeling of electrochemical systems.